REPUBLIC OF TÜRKİYE
YILDIZ TECHNICAL UNIVERSITY
GRADUATE SCHOOL OF SCIENCE AND ENGINEERING

DEVELOPMENT OF GLASS-BASED LUMINESCENT SOLAR CONCENTRATORS FOR BUILDING-INTEGRATED PHOTOVOLTAIC APPLICATIONS

Emre İLTER

MASTER OF SCIENCE THESIS

Department of Metallurgy and Materials Engineering

Materials Program

Supervisor

Prof. Dr. Ali Erçin ERSUNDU

January 2026

REPUBLIC OF TÜRKİYE

YILDIZ TECHNICAL UNIVERSITY

GRADUATE SCHOOL OF SCIENCE AND ENGINEERING

DEVELOPMENT OF GLASS-BASED LUMINESCENT SOLAR CONCENTRATORS FOR BUILDING-INTEGRATED PHOTOVOLTAIC APPLICATIONS

A thesis submitted by Emre İLTER in partial fulfillment of the requirements for the degree of MASTER OF SCIENCE is approved by the committee on 20.01.2026 in Department of Metallurgical and Materials Engineering, Program of Materials.

Prof. Dr. Ali Erçin ERSUNDU
Yildiz Technical University
Supervisor

Approved By the Examining Committee

Prof. Dr. Ali Erçin Ersundu, Supervisor
Yildiz Technical University _____

Assoc. Prof. Dr. Mehmet Yılmaz, Member
Yildiz Technical University _____

Assoc. Prof. Dr. Furkan Kuruoğlu, Member
Istanbul University _____

I hereby declare that I have obtained the required legal permissions during data collection and exploitation procedures, that I have made the in-text citations and cited the references properly, that I haven't falsified and/or fabricated research data and results of the study and that I have abided by the principles of the scientific research and ethics during my Thesis Study under the title of Development of Glass-Based Luminescent Solar Concentrators for Building-Integrated Photovoltaic Applications supervised by Prof. Dr. Ali Erçin ERSUNDU. In the case of a discovery of false statement, I am to acknowledge any legal consequence.

Emre İLTER



This work was supported by the project no FYL-2025-6869 of Yıldız Technical University Scientific Research Projects Coordination Unit.

Dedicated to my family

and my beautiful soulmate

ACKNOWLEDGEMENTS

I would like to express my deepest gratitude to Prof. Dr. Ali Erçin ERSUNDU for his invaluable support, inspiration, and guidance throughout this journey. I am equally grateful to Prof. Dr. Miray ÇELİKBİLEK ERSUNDU for her meticulous guidance and unwavering support during my years as a student. It has been a great privilege to be their student.

Being part of the Yıldız Technical University and YTU Glass Research Group has been a true blessing, where I found not only colleagues but lifelong friends. I am especially thankful to Utku EKİM and Harun Samet ÇELİK for their guidance and companionship, and to all my colleagues who have supported me like family.

I owe heartfelt thanks to my parents and brother for their endless love and support, which have been the foundation of both my education and professional life.

Finally, I am profoundly grateful to my beloved partner, whose unwavering presence and encouragement have carried me through the most challenging times, ensuring I never felt alone.

Emre İLTER

TABLE OF CONTENTS

LIST OF SYMBOLS ..... **viii**

LIST OF ABBREVIATIONS ..... **x**

LIST OF FIGURES ..... **xii**

LIST OF TABLES ..... **xvii**

ABSTRACT ..... **xix**

ÖZET ..... **xxi**

1 INTRODUCTION **1**

1.1 Literature Review 1

1.2 Objective of the Thesis 5

1.3 Original Contribution 6

2 THEORETICAL INFORMATION **8**

2.1 Luminescence 8

2.2 Luminescent Materials 10

2.3 Luminescent Solar Concentrators 14

2.4 Host-Waveguide Selection for LSCs 30

2.5 PVs Used for LSCs 33

3 EXPERIMENTAL STUDIES **35**

3.1 Sample Preparation 35

3.2 Characterization Studies 37

4 Eu^{3+}-DOPED GLASS-BASED LSCs **40**

4.1 Thermal, Structural, Optical and Photoluminescence Properties 40

4.2 Photonic Collection, Conversion and Waveguiding Properties 43

4.3 Evaluation of Optical, Environmental and Mechanical Performance ...49
4.4 LSC Device Study 51
5 PQD GNC-BASED LSCs 59
5.1 Thermal, Structural, Optical and Photoluminescence Properties 59
5.2 Evaluation of Optical, Environmental, and Mechanical Performance ..65
5.3 Photonic Collection, Conversion, and Waveguiding Properties 67
5.4 LSC Device Study 70
6 CONCLUSION 76
6.1 Conclusions....76
6.2 Future Outlook....77
7 REFERENCES....79
PUBLICATIONS FROM THE THESIS 93

LIST OF SYMBOLS

A_{edge}	Total area of the waveguide edges (cm^2)
A_{lsc}	Top surface area of the waveguide edges (cm^2)
C	Concentration factor
d	Waveguide thickness (cm or mm)
E_g	Optical bandgap energy (eV)
EQE_{lsc}	External quantum efficiency of LSC device
G	Geometric gain factor
h	Planck's Constant
$I_0(\lambda)$	Edge emission intensity at the optical path length $L = 0$
$I_{edge}, I_{bulk}, I_{surf}$	Emission intensities (edge, bulk, surface geometry)
I_{sc}	Short-circuit current (mA or A)
J_{sc}	Short-circuit current density (mA/cm^2)
k_R, k_{NR}	Radiative and non-radiative decay rates (s^{-1})
L	Optical path length / Waveguide length (cm)
n_{wg}, n_s	Refractive index of the waveguide and surrounding medium
P_{in}	Total incident optical power (W)
$P_{opt,edge}$	Optical power reaching waveguide edges (W)
Q_{lsc}	LSC Quality factor (Klimov model)
R	Fresnel reflection coefficient
S_0, S_1, T_1	Ground singlet, excited singlet, and triplet energy states
V_{oc}	Open-circuit voltage (V)
$\alpha(\lambda)$	Absorption coefficient (cm^{-1})
β	Optical efficiency constant (scattering factor in Weber-Lambe model
η_{abs}	Absorption efficiency
η_{edge}	Edge emission efficiency (experimental)
η_{ext}	External photon efficiency
η_{int}	Internal photon efficiency
η_{opt}	Optical efficiency (Photonic collection efficiency)

η_{pl}	Intrinsic photoluminescence quantum yield
$\eta_{pl,wg}$	Waveguide-integrated quantum yield
η_{pv}	Power conversion efficiency of the LSC attached PV cell
η_{ra}	Reabsorption survival factor (non-reapsorption efficiency)
η_{trap}	Trapping efficiency
θ_c	Critical angle of total internal reflection
λ	Wavelength (nm)
$\mu(\lambda)$	Linear attenuation coefficient (mm^{-1})
τ, τ_{ave}	Photoluminescence lifetime (average) (ns or ms)
ϕ_s	Solar photon-flux spectrum

LIST OF ABBREVIATIONS

AM1.5	Air Mass 1.5 Global
AVT	Average Visible Transmittance
BIPV	Building-Integrated Photovoltaic
CB	Conduction Band
CIE	Commission Internationale de I'Éclairage
CRI	Color Rendering Index
DASF	Derivative Absorption Spectrum Fitting
EMA	Effective Mass Approximation
EQE	External Quantum Efficiency
EVA	Ethylene Vinyl Acetate
FF	Fill Factor
FFT	Fast Fourier Transform
FWHM	Full Width at Half Maximum
GNC	Glass Nanocomposite
HOMO	Highest Occupied Molecular Orbital
HRTEM	High-Resolution Transmission Electron Microscopy
LED	Light Emitting Diode
LSC	Luminescent Solar Concentrator
LUMO	Lowest Unoccupied Molecular Orbital
NIR	Near-Infrared
OE	Optical Efficiency
PCE	Power Conversion Efficiency
PDMS	Polydimethylsiloxane
PERC	Passivated Emitter and Rear Cell
PL	Photoluminescence
PLA	Polylactic acid
PLQY	Photoluminescence Quantum Yield
PMMA	Polymethyl Methacrylate
PS	Polystyrene

PU	Polyurethane
PQD	Perovskite Quantum Dot
PV	Photovoltaic
PVDF	Polyvinylidene Fluoride
PVB	Polyvinyl Butyral
QD	Quantum Dot
STA	Simultaneous Thermal Analysis
TCSPC	Time-Correlated Single-Photon Counting
TEM	Transmission Electron Microscopy
UV	Ultraviolet
VB	Valence Band
XRD	X-ray Diffraction

LIST OF FIGURES

Figure 2.1 (a) Spin states: singlet ground, singlet excited, and triplet. (b) Partial Jablonsky diagram showing fundamental processes of luminescence. 9

Figure 2.2 Fundamental photon processes of photoluminescence. 9

Figure 2.3 Dieke diagram showing calculated energy levels of Ln^{3+} ions, adapted from the reference. [169] 11

Figure 2.4 (a) Schematic energy diagrams for the electronic structures of atoms, molecules, small and large QDs and bulk semiconductors. (b) Electron-hole pair (exciton) generation, recombination, and photoluminescence emission by a QD. c) Energy level diagram showing direct/indirect band gap structures in momentum space. 12

Figure 2.5 Schematic representation of a planar luminescent solar concentrator, illustrating (1) incident light, (2) luminescent centers, (3) total internal reflection, (4) the waveguide/host medium, and (5) edge-mounted PV cells receiving the guided photoluminescence emission. 15

Figure 2.6 Schematic illustration of the glass host and waveguide, showing the main optical processes: (1) incident light, (2) reflection, (3) transmission, (4) absorption, (5) host attenuation, (6) photoluminescence (PL) emission, (7) escape cone, (8) reabsorption, and (9) total internal reflection. 17

Figure 2.7 Normalized EQE spectra of some PV cell types. 34

Figure 3.1 Schematic representation of the fabrication workflow for Eu^{3+}-doped and PQD GNC–LSC specimens follows a shared route of melt-quenching, annealing, and mechanical shaping. A distinctive secondary thermal treatment is applied exclusively to the PQD-GNC samples to

trigger the in-situ growth of perovskite nanocrystals, thereby defining their final optoelectronic properties. 37

Figure 3.2 Flowchart of the Monte Carlo ray-tracing model. 39

Figure 4.1 (a) STA curve of the glass sample containing 0.50 mol% Eu^{3+}, illustrating its thermal transition behavior. (b) XRD pattern of the same composition, confirming the amorphous structure through the presence of a broad diffuse halo. (c) UV–Vis absorption spectra of all synthesized glasses; the inset highlights the weak Eu^{3+} absorption features and includes photographs of undoped and doped samples under ambient light and UV excitation. (d) Steady-state photoluminescence excitation spectra monitored at the 613 nm emission, alongside the corresponding emission spectrum excited at 393 nm for Eu^{3+}-doped glasses. (e) PLQY values measured under 393 nm excitation for samples containing 0.25, 0.50, and 1.00 mol% Eu_2O_3. (f) Time-resolved PL decay traces at 613 nm collected following pulsed excitation at 393 nm. 41

Figure 4.2 (a) Conceptual illustration of the Eu^{3+}-doped glass waveguide showing the principal optical events, including photon absorption, photoluminescence emission, and confinement via total internal reflection. (b) Photoluminescence spectra collected from the bulk, surface, and edge regions using an integrating sphere. The inset tables summarize the extracted η_{edge}, η_{int}, and η_{ext} parameters, where η_{ext} is calculated for both monochromatic 393 nm excitation and the full AM1.5G solar spectrum. Schematics on the left depict the corresponding detection geometries, with black-shaded areas indicating masked surfaces used to block undesired emission. (c) Photographic images of Eu^{3+}-doped glass waveguides containing 0.50 mol% Eu_2O_3 with lateral lengths of 2, 4, and 6 cm (L = 2, 4, 6 cm), shown under normal illumination and under UV excitation. 44

Figure 4.3 (a) Schematic representation of the measurement concept used to evaluate edge-emitted photoluminescence as a function of in-plane optical path length *L*. (b) Experimental arrangement employed for optical-path–dependent PL measurements, showing the excitation and

collection geometry. (c) Representative edge-emission spectra recorded for the Eu^{3+}-doped glass sample with a lateral dimension of 6 cm. (d) Exponential decay fit of the integrated edge-emission intensity I_L as a function of the optical distance L for the 0.50 mol% Eu^{3+} sample. 48

Figure 4.4 (a) Optical transmittance spectrum of the glass containing 0.50 mol% Eu^{3+}, with an inset photograph showing a 6×6 cm^2 sample illuminated by natural sunlight. (b) Temperature-dependent PL emission spectra recorded as the sample was heated from ambient temperature to 200 °C. (c) Corresponding luminescence photographs taken at 50 °C and 200 °C, illustrating thermal effects on emission. (d) Variation in PL intensity tracked over four sequential heating–cooling cycles. (e) Time evolution of optical transmittance and photoluminescence quantum yield during 30 days of immersion in deionized water. (f) Photoluminescence stability under continuous 393 nm excitation monitored over a period of 50 hours. (g) Vickers microhardness values obtained under different applied loads, with the inset showing representative indentation marks at 100× magnification. 49

Figure 4.5 (a) Schematic representation and corresponding photograph of the customized measurement platform used to couple the Eu^{3+}-doped glass waveguide to the laser-cut silicon cell, illustrated for the device with L = 2 cm under AM1.5G illumination. (b) Current–voltage curves of LSCs fabricated with waveguide lengths of 2, 4, and 6 cm, shown together with the reference cut-cell for comparison. (c) External quantum efficiency of the LSC devices as a function of waveguide length. (d) Wavelength-dependent EQE_{lsc} (λ) for the 6 cm device, plotted alongside the PL emission profile, the EQE of the standalone cut-cell, and the AM1.5G solar spectrum. EQE_{lsc} (λ) and the reference EQE are given in percentage units, whereas the PL and AM1.5G spectra are displayed in arbitrary units.....52

Figure 5.1 (a) STA curve of the as-cast glass. (b) XRD patterns of the as-cast sample and PQD GNCs heat-treated between 510–570 °C (10 °C increments, 4h). (c) Bright-field TEM and (d) HAADF-STEM images of the 540 °C–4h GNC sample, showing a uniform distribution of $CsPbBr_3$ PQDs

within the glass matrix. (e) Particle size histogram obtained from measurements of more than 300 PQDs. (f, i) HRTEM images confirming $CsPbBr_3$ nanocrystals embedded in the glass. (g, j) Magnified HRTEM views of the PQDs marked in (f) and (i). (h, k) Corresponding FFT power spectra of the nanoparticles shown in (g) and (j), verifying the cubic $CsPbBr_3$ phase.....61

Figure 5.2 (a) Photographs of the as-cast glass and samples heat-treated between 510–570 °C under daylight and UV illumination. (b) Optical absorption spectra and (c) corresponding DASF plots of the same series. (d) PL emission spectra of the heat-treated samples under 450 nm excitation. (e) PLQY values measured for ~1×1×1 mm^3 pieces under 360 nm excitation. (f) PLQY spectrum of the 540 °C sample, with an inset showing the measured piece. (g) Time-resolved PL decay curves of the heat-treated samples under 450 nm pulsed excitation. 64

Figure 5.3 (a) Transmittance spectrum of the 5×5 cm^2 GNC waveguide, with inset images highlighting its uniform structure and optical clarity. (b) Temperature-dependent PL emission spectra; the inset shows heating–cooling cycles between 25–200 °C and corresponding luminescence images. (c) PLQY values of a 1×1×1 mm^3 reference sample measured periodically over 60 days of water immersion. d) Photostability of the GNC waveguide under continuous excitation. (e) Vickers hardness measurements under various loads, with insets showing indentations at 100× magnification. All stability characterizations were performed under 360 nm excitation.....66

Figure 5.4 (a) Digital images of GNC waveguides (1×1 cm^2 to 5×5 cm^2) under daylight and under UV illumination in PLA holders, in which three edges and the back surface act as blackbody absorbers. (b) PL spectra of total, surface, and edge emissions measured under diffuse 360 nm excitation inside an integrating sphere; inset schematics indicate emitting surfaces, with black regions denoting masked areas. (c) Schematic of the experimental setup showing the definition of optical path length and the measurement procedure. (d) PL spectra of the 5×5 cm^2 waveguide collected at varying optical path lengths. (e) PL peak

position and intensity as a function of optical path length, combining experimental data up to 5 cm with Monte Carlo simulations extending from 10 to 100 cm; the inset illustrates the simulation approach. 68

Figure 5.5 a) Custom measurement setup integrating GNC-LSC waveguides with cut silicon solar cells, shown here with a 5×5 cm^2 device under AM1.5 illumination. b) Schematic of the system layout and a photograph of the cut solar cell (8.0×1.0 cm^2). c) EQE spectrum of the uncut PERC cell overlaid with the PL emission range of a 5×5 cm^2 GNC-LSC waveguide. d) Electrical performance of the cut solar cell. e) I–V characteristics of GNC-LSC devices with sizes from 1×1 cm^2 to 5×5 cm^2. f) Optical efficiency (OE) of GNC-LSC devices spanning 1×1 cm^2 to 100×100 cm^2, showing experimental results (up to 5×5 cm^2) and analytical predictions (dashed lines). g) Power conversion efficiencies of GNC-LSC devices (PCE_{lsc}) from 1×1 cm^2 to 100×100 cm^2, combining experimental data and simulation results, together with a comparison of representative PQD-based LSC studies across different hosts, PQD types, and device dimensions. Reported PCE values are evaluated for methodological consistency and linked to their original literature sources. 71

LIST OF TABLES

Table 4.1 Average visible transmittance (AVT), color rendering index (CRI), and CIELAB chromaticity values for the undoped glass and the Eu^{3+}-doped samples containing 0.25%, 0.50%, and 1.00% Eu_2O_3. 50

Table 4.2 Photovoltaic parameters of LSC devices with waveguide lengths of L = 2, 4, and 6 cm, presenting both calculated values and experimentally measured parameters normalized to four-edge coupling. 53

Table 4.3 Overview of Eu^{3+}-based LSC studies, classified according to LSC architecture, luminophore properties, host material, fabrication route, device dimensions, η_{pl}, optical efficiency (OE), and power conversion efficiency (PCE). The table highlights performance variations, compliance with the LSC consensus reporting guidelines, and peak or representative PCE values, with complete bibliographic details given in the reference section. 56

Table 5.1 Summary of the as-cast and heat-treated PQD GNCs at various temperatures, including their absorption edge, direct optical bandgap energies, particle radii determined by the EMA method, PL center peak wavelengths, FWHM, and Stokes shift values. 62

Table 5.2 Photoluminescence lifetime parameters of PQD GNCs heat-treated at temperatures between 510°C and 570°C. 65

Table 5.3 Edge emission efficiency (η_{edge}), internal photon efficiency (η_{int}), and external photon efficiency (η_{ext}) of GNC-LSC waveguides under 360 nm monochromatic and AM1.5 illumination. 69

Table 5.4 Lifetime parameters for optical path dependent PL measurements for the largest sample, 5x5 cm^2. 70

Table 5.5 Photovoltaic parameters of GNC-LSC devices as a function of device size, including experimentally measured values up to 5×5 cm^2 and simulated results for larger devices extending to 100×100 cm^2. 72

Table 5.6 Overview of PQD-based LSC studies categorized by encapsulating hosts, PQD luminophore types, host materials, LSC dimensions, thicknesses, quantum yield (QY) values, optical efficiencies (OE), and power conversion efficiencies (PCE). The table also highlights variations or compatibility with the consensus statement. (PCE and OE values represent the highest-performing or most representative examples reported in each study). 74

ABSTRACT

Development of Glass-Based Luminescent Solar Concentrators for Building-Integrated Photovoltaic Applications

Emre İLTER

Department of Metallurgy and Materials Engineering
Master of Science Thesis

Supervisor: Prof. Dr. Ali Erçin ERSUNDU

Building-integrated photovoltaics (BIPV) require transparent, durable, and scalable light-harvesting surfaces capable of operating under direct, diffuse, and indoor illumination. Luminescent solar concentrators (LSCs) address this need by collecting sunlight over a large area and guiding it to small photovoltaic cells located at the device edges. In this study, two glass-based LSC platforms are developed within a 2.5-mm-thick architecture: (i) Eu^{3+}-doped glasses designed for high transparency and color neutrality, and (ii) $CsPbBr_3$ perovskite quantum dot glass nanocomposites (PQD-GNCs) engineered for high photon-conversion efficiency. A unified experimental and model-based framework is applied to relate laboratory-scale results with meter-scale performance.

For Eu^{3+}-doped glasses, optimization of dopant concentration minimizes transport losses while preserving optical clarity. LSC devices fabricated in sizes ranging from 2×2 to 6×6 cm^2 exhibit an average visible transmittance of ~90%, near-neutral color rendering (CRI ≈ 98), and strong environmental stability. The external photon

efficiency (η_{ext}) remains nearly constant at ~6.4% for all device sizes, indicating negligible waveguide-related losses during scaling. However, the peak PCE_{lsc} decreases from 0.852% to 0.164% with increasing dimensions. This reduction arises purely from geometric effects: while the light-collecting surface area increases quadratically, the energy-converting edge area grows only linearly. As a result, efficiency per unit area declines, even though absolute current, voltage, and power output increase with device size.

In PQD-GNC LSCs, a broad absorption profile combined with a high quantum yield (QY ≈ 97%) enables efficient photon conversion while maintaining ~90% transmittance beyond the absorption edge. At 1×1 cm^2, devices achieve a PCE_{lsc} of 3.16%, an optical efficiency of 27.13%, and η_{ext} of 53.7%. When scaled to 5×5 cm^2, total electrical output increases, but PCE_{lsc} decrease to 0.38% due to geometric gain. Optical efficiency and η_{ext} decrease to, 2.78%, and 35.2%, respectively, due to emerging waveguide losses. Monte Carlo simulations extended to 100×100 cm^2 reveal that this initial performance decline saturates near 3×3 cm^2, reflecting a balance between waveguide losses and the expanding geometric gain, indicating further increase in size does not affect device performance.

Overall, Eu^{3+}-doped glasses and PQD-GNCs represent complementary LSC platforms, emphasizing aesthetic neutrality and high photon-conversion performance, respectively. These findings demonstrate the feasibility of durable and scalable glass-based LSCs for BIPV applications such as architectural facades and windows.

Keywords: Luminescent solar concentrators, Building-integrated photovoltaics, Perovskite quantum dots, Europium, Glass nanocomposites

ÖZET

Binalara Entegre Fotovoltaik Uygulamaları için Cam Tabanlı Lüminesan Güneş Yoğunlaştırıcıların Geliştirilmesi

Emre İLTER

Metalurji ve Malzeme Mühendisliği Anabilim Dalı

Yüksek Lisans Tezi

Danışman: Prof. Dr. Ali Erçin ERSUNDU

Bina ile bütünleşik fotovoltaik (BIPV) sistemler, doğrudan, dağınık ve iç mekân aydınlatması altında çalışabilen şeffaf, dayanıklı ve ölçeklenebilir ışık toplayıcı yüzeylere ihtiyaç duyar. Lüminesanslı güneş yoğunlaştırıcılar (LSC'ler), geniş bir yüzeyden güneş ışığını toplayıp cihaz kenarlarına yerleştirilen küçük fotovoltaik hücrelere dalga kılavuzluğu yoluyla yönlendirerek bu gereksinimi karşılar. Bu çalışmada, 2.5 mm kalınlığında iki cam esaslı LSC platformu geliştirilmiştir: (i) yüksek şeffaflık ve renk nötrlüğü için tasarlanan Eu^{3+} katkılı camlar ve (ii) yüksek foton dönüşüm performansı için geliştirilen $CsPbBr_3$ perovskit kuantum nokta cam nanokompozitleri (PQD-GNC). Laboratuvar ölçekli sonuçların metre ölçeğine taşınması için birleşik deneysel ve model tabanlı bir yaklaşım uygulanmıştır.

Eu^{3+} katkılı camlarda katkı oranının optimize edilmesi, optik berraklık ve renk nötrlüğü korunurken taşıma kayıplarını en aza indirmiştir. 2×2 ile 6×6 cm^2 arasında üretilen LSC cihazları, görünür bölgede ortalama ~%90 geçirgenlik, neredeyse nötr renk üretimi (CRI ≈ 98) ve yüksek çevresel kararlılık sergilemiştir. Dış foton

verimliliği (η_{ext}) tüm boyutlarda ~%6.4 civarında sabit kalarak ölçekleme sırasında dalga kılavuzu kaynaklı kayıpların ihmal edilebilir olduğunu göstermiştir. Buna karşın, PCE_{lsc} değeri boyut artışıyla 0.852%'den 0.164%'e düşmüştür. Bu azalma tamamen geometrik bir etkiden kaynaklanmaktadır: ışık toplayan yüzey alanı karesel olarak artarken, enerji dönüştüren kenar alanı yalnızca doğrusal olarak büyümektedir. Sonuç olarak birim alan başına verim düşerken, toplam akım, gerilim ve güç çıktıları cihaz boyutuyla birlikte artmaktadır.

PQD-GNC LSC'lerde geniş soğurma profili ve yüksek kuantum verimi (QY ≈ %97) birlikte etkin foton dönüşümünü mümkün kılmaktadır. 1×1 cm^2 boyutunda PCE_{lsc} %3.16, optik verim %27.13 ve η_{ext} %53.7 olarak elde edilmiştir. Boyut 5×5 cm^2'ye çıkarıldığında toplam elektrik çıktısı artmakta, ancak PCE_{lsc} geometrik kazanım sebebiyle %0.38'e düşmektedir. Optik verim ve η_{ext} sırasıyla %0.38, %2.78 ve %35.2'ye düşmektedir; ki bu durum dalga kılavuzu kayıplarının ortaya çıkmasıyla ilişkilidir. 100×100 cm^2'ye kadar yapılan Monte Carlo simülasyonları, optik performanstaki ilk düşüşün yaklaşık 3×3 cm^2 civarında doygunluğa ulaştığını ve dalga kılavuzu kayıpları ile artan ışık toplama alanı arasında bir denge oluştuğunu, dolayısıyla artan boyutun artık cihaz performansını etkilemediğini göstermektedir.

Sonuç olarak, Eu^{3+} katkılı camlar estetik nötrlüğü, PQD-GNC sistemleri ise yüksek foton dönüşüm kapasitesini öne çıkaran tamamlayıcı LSC platformları sunmaktadır. Bu bulgular, mimari cepheler ve pencereler gibi BIPV uygulamaları için dayanıklı ve ölçeklenebilir cam tabanlı LSC'lerin uygulanabilirliğini ortaya koymaktadır.

Anahtar Kelimeler: Lüminesan güneş yoğunlaştırıcılar, Bina-bütünleşik fotovoltaikler, Perovskit kuantum noktalar, Evropiyum, Cam nanokompozit

1
INTRODUCTION

1.1 Literature Review

Urban energy consumption has surged, driven by rapid population growth, the electrification of transport, and the emergence of digital technologies, all of which have significantly increased the energy demand of modern cities. [1–5] This trajectory has intensified the demand for renewable power generation systems integrated directly into the built environment which is a cornerstone of net-zero energy building design. [6,7] While conventional photovoltaic (PV) modules represent the most established solution for on-site generation, their inherent opacity severely restricts their application on building facades, where transparency, visual neutrality, and daylight access are non-negotiable architectural requirements. [8] Although semi-transparent PV technologies offer a partial solution, they typically require the placement of the photovoltaic stack within the optical aperture of the glazing. This configuration often compromises aesthetic quality due to the visibility of current-collecting grids and wiring, complicating their seamless integration into modern architectural envelopes. [9,10]

Luminescent solar concentrators (LSCs) present a fundamentally distinct alternative that circumvents these limitations. In a typical LSC architecture, a transparent waveguide (composed of glass or polymer) is doped with specific luminophores that absorb incident solar radiation and re-emit it at longer wavelengths. A significant fraction of this re-emitted light is trapped within the waveguide via total internal reflection and guided toward compact PV cells mounted unobtrusively at the device edges. [11]

By spatially decoupling the optical collection area from the photovoltaic conversion zone, LSCs enable large-area light harvesting with minimal visual impact.

Furthermore, their ability to effectively concentrate on both direct and diffuse light renders them particularly advantageous for deployment in densely built urban environments or climates characterized by frequent cloud cover. [12] The performance of an LSC depends strongly on the photophysical characteristics of the embedded emitters, notably their absorption strength, photoluminescence quantum yield (PLQY), and the magnitude of their Stokes shift, along with how well their emission aligns with the spectral response of the edge-mounted photovoltaic cell. For example, broadband absorbers capture sunlight efficiently but compromise transparency and color uniformity, while narrow absorbers preserve visual quality at the expense of photon collection. Any loss of PLQY reduces conversion efficiency, and insufficient Stokes shift enhances reabsorption during waveguiding. For these reasons, general approach in the current literature is to tailor the emission properties of the emitters. [13]

To date, a wide range of emitters including organic dyes [14–20], rare earths ions and their complexes [21,22], semiconductor nanocrystals [12], and more recently perovskite nanocrystals [23] have been explored for LSCs applications. Historically, the development of LSC emitters has progressed along two primary material classes. The first comporises molecular emitters, particularly organic dyes, which offer high radiative efficiency and straigtforward processing but are limited by narrow absorption bands and small Stokes shifts, leading to significant reabsorption losses. [16,24–26] Advanced design strategies such as aggregation induced emission (AIE) [27] and Förster resonance energy transfer (FRET) [28–30] have been employed to reduce these losses. Rare-earth comlexes, in contrast, provide broadband absorption and large Stokes shifts; however, their dependence on organic antenna ligands for sensitization introduces challenges related to photostability and intricate synthesis routes. [21]

Colloidal nanocrystals represent the second major category, offering size-tunable optical properties. [31] Early research centered on cadmium-based quantum dots, which set the performance benchmarks for colloidal emitters [31–37], but their practical integration is limited by intrinsic toxicity and small Stokes shifts, requiring sophisticated core/shell architectures to suppress reabsorption. [38–41] This challenge prompted a shift toward ternary I–III–VI nanocrystals, such as $CuInS_2$,which combine large Stokes shifts with low toxicity [12,42–55] and

maintaining high stability under environmental exposure. [56–58] Carbon [59–80] and silicon quantum dots [81–86] followed as earth-abundant and stable alternatives, though their absorption cross-sections are generally lower. More recently, perovskite nanocrystals have emerged as highly promising candidates due to their defect-tolerance, near-unity QY and narrow emission linewidths. [23,87–95] Key advances include Stokes shift engineering through Mn-doping [91,96], quantum cutting enabled by Yb-doping [94,97], and performance enhancement via plasmonic coupling. [92,98–100] Despite these advantages, environmental instability continues to pose a major barrier to their widespread deployment in LSCs.

Beyond improvements in individual luminophores alone, several engineering strategies have also emerged. These include scattering-enhanced LSC designs [101–103] and a substantial body of research that integrates multiple luminophores within a single architecture to combine the advantageous properties of different material classes. [47,54,66,104–115]

In addition to luminophore engineering, the selection of the host matrix represents a critical design parameter. The host is not merely a structural container but an active optical component whose refractive index determines the critical angle for total internal reflection and, consequently, the light-trapping efficiency. [12,116–118] In addition, the long-term stability of the luminophore is tightly coupled to the host's ability to provide a hermetic barrier against environmental stressors. [116,117,119–122]

Depending on the device configuration, the host may serve directly as the waveguide or function as a separate carrier layer. For example, liquid hosts where emitters are dissolved in a solvent confined within a transparent vessel allow facile spectral tuning. [123] However, leakage risks and insufficient long-term preservation of the emitters limit their practical utility. As a result, solid-state matrices dominate the field, following two primary approaches. The first involves surface coatings, in which emitters are dispersed within thin polymeric films applied onto transparent substrates. [124] While this method offers precise spectral control, it suffers from vulnerabilities such as delamination and UV degradation. The second approach is bulk incorporation, where emitters are embedded directly within the matrix volume, thereby reducing interfacial losses and simplifying

fabrication. Nevertheless, bulk incorporation often imposes stricter constraints on processing temperatures, chemical compatibility, and doping flexibility.

In both solid-state approaches, a wide range of polymers have been employed including PMMA [21,95,106,125–134], PDMS [92,107,135,136], PS [88,90,137], resins [138–141], and various hybrid organic-inorganic materials. [22,114,142–152] However, polymers inherently suffer from limited thermal, chemical and photostability. [26,153–155] These limitations have redirected attention toward inorganic glass matrices, which combine superior mechanical robustness with natural compatibility for architectural glazing applications. [156–158]

Despite these advantages, the incorporation of emitters into inorganic glass remains relatively unexplored. Early demonstrations include laser-written perovskite nanocrystals [159,160] and ultrathin glass sheets [161], though these approaches were hindered by handling fragility and measurement inconsistencies. Similarly, in-situ grown PbSe nanocrystals in glass successfully extended absorption into the near-infrared [162], but their QY remained comperatively low. While lanthanide-doped glasses inherently provide large Stokes shifts [163], their device-level performance has not been systematically evaluated.

This thesis addresses these gaps by developing two distinct glass-based LSC platforms: Eu^{3+}-doped glasses designed for highly transparent and color-neutral LSCs, and $CsPbBr_3$ perovskite quantum dot glass nanocomposites engineered for high photon-conversion performance. To mitigate the handling fragility and measurement inconsistencies common in the literature, both systems are fabricated within a standardized 2.5-mm thick architecture. A unified experimental and simulation-based framework is established to evaluate the fundamental trade-offs between two emitter classes: Eu^{3+}, characterized by its Stokes shift and low re-absorption losses despite a smaller absorption cross-section; and $CsPbBr_3$, offering near-unity QY and broad absorption but with a more limited Stokes shift. By linking laboratory-scale photophysical measurements to simulation-based meter-scale device behaviour, this thesis work provides a comprehensive assessment of the scalability of both systems. Ultimately, the study delivers a practical roadmap for design of durable, glass-integrated LSCs optimized for real-world architectural applications.

1.2 Objective of the Thesis

Luminescent glasses have strong potential for use in building integrated LSCs due to their high thermal, chemical, and mechanical stability. Although studies show that inorganic glasses can reach optical performance similar to polymericmaterials, most research has stayed at the proof-of-concept stage. Therefore, it is important to explore systems that are scalable, meet architectural needs such as color and transparency, and maintain long-term stability.

This thesis develops systematic evaluation framework for luminescent glasses in LSCs. Two types of emitters were embedded in the same glass matrix: Eu^{3+} lanthanide ions and $CsPbBr_3$ perovskite quantum dots. These materials were chosen to represent two contrasting optical behaviours. Eu^{3+}-based LSCs have narrow absorption and relatively low QY but a large Stokes shift, which reduces reabsorption losses and allows long-distance photon transport. They also maintain neutral color and high transparency, which are beneficial for architectural applications. In contrast, $CsPbBr_3$-based LSCs have broad absorption and very high QY, enabling strong spectral conversion, but their smaller Stokes shift can cause reabsorption losses, and they impart a noticable color to the glass.

In this context, two sets of glass based waveguides embedded with Eu^{3+} and $CsPbBr_3$ were synthesized, and their optical and emission properties were optimized. Selected glass samples were tested for thermal, chemical, photostability, and mechanical durability. The effect of scaling on performance was then evaluated both optically and electronically by producing waveguides in different sizes. Finally, both systems were compared to literature reports from architectural and optoelectronic perspectives.

Ultimately, this study demonstrates that the same glass matrix can incorporate different emitters, resulting in distinct optical behaviors and potential applications. The selected systems show stability under environmental conditions, making them suitable for building-integrated photovoltaic applications, while their fabrication allows straightforward scalability. This work thus highlights a practical pathway for deploying glass-based luminescent solar concentrators in real-world architectural settings. .

1.3 Original Contribution

Luminescent glasses are promising platforms for LSCs due to their high thermal, chemical, and mechanical stability. Although some studies exist in the recent literature, most remain at the proof-of-concept level focusing on emission properties, leaving real-world architectural requirements, such as color, transparency, durability and scalability, largely unexplored. There is therefore a need for a comprehensive engineering approach that considers optical, structural, and architectural aspects together.

In this work, Eu^{3+}-doped borosilicate glass waveguides were synthesized and shown to transport photons efficiently to remote edges. Despite their narrow absorption bands, the large Stokes shift minimizes reabsorption losses, enabling consistent photon transport efficiency independent from the waveguide size. These glasses also maintain high transparency and neutral color while exhibiting superior durability under environmental conditions. Combined with acceptable power generation, results indicate that Eu^{3+}-doped glass LSCs offer a scalable and mass-producible solution for BIPV.

In parallel, $CsPbBr_3$ PQDs were grown within a borosilicate glass matrix, with composition and heat treatment optimized to achieve the highest QY reported to date. This system absorbs broadly and converts photons efficiently, but its narrower Stokes shift raises concerns for long-distance photon transport. Experimental tests together with Monte-Carlo simulations showed that photon loss stabilizes beyond a certain size, preventing further efficiency reduction. Simulations also confirmed this behavior up to square-meter scale, indicating high efficiency can be maintained even at higher scales. The perovskite system also exhibited strong durability, and its potantial for tunable emission colors demonstrate that PQD GNC based LSCs can meet diverse architectural requirements.

Finally, performance evaluations for both systems were organized into a modular structure, separating the effects of different loss mechanisms. This approach provides a clear, reproducible, and practical framework for assessing glass-based LSC performance, addressing inconsistencies in current literature. Importantly, the original contribution of this work is showing that the same luminescent glass matrix

can host different emitters, producing distinct optical properties and applications while remaining stable, scalable, and suitable for BIPV integration.

2
THEORETICAL INFORMATION

2.1 Luminescence

Electromagnetic radiation spans an enormous spectrum, from gamma rays to radio signals, with visible light occupying only the 380–750 nm interval. Regardless of wavelength, the generation of this radiation stems from two fundamental pathways. The first is *incandescence*, the emission of thermal radiation from hot matter. The second is *luminescence*, where light is generated by the radiative relaxation of electronically excited atoms or molecules without elevated temperatures, a mechanism that underpins applications ranging from solid-state lighting to optical sensing. [164]

The first classification of these phenomena depends on the excitation source. Common forms include *electroluminescence* (electric fields), *cathodoluminescence* (electrons), and *triboluminescence* (mechanical stress). [165] However, this work focuses exclusively on *photoluminescence* due to its critical role in light-harvesting applications and optoelectronics.

Photoluminescence arises when electrons are excited from the ground state (S_0) to higher singlet energy levels (S_n) by an interaction of incoming photon(s). As illustrated in Figure 2.1a, the subsequent relaxation pathways are dictated by spin dynamics and the emission lifetime (τ). *Fluorescence* corresponds to a fast, spin-allowed transition from the excited singlet state (S_1) back to S_0, typically occurring within nanoseconds. In contrast, *phosphorescence* involves a transition to a triplet state (T_1) via intersystem crossing, resulting in a delayed emission (10^{-6} s to hours) due to the spin-forbidden nature of the $T_1 \rightarrow S_0$ decay. Figure 2.1b maps these competing pathways, highlighting the role of spin-orbit coupling in mediating transitions between the singlet and triplet manifolds. [166]

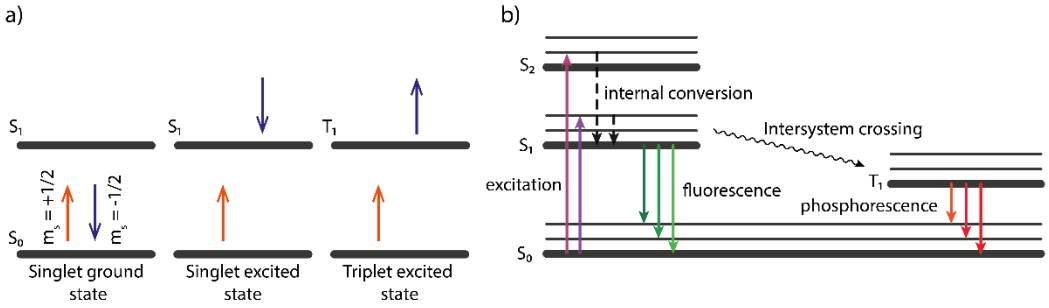


Figure 2.1 (a) Spin states: singlet ground, singlet excited, and triplet. (b) Partial Jablonsky diagram showing fundamental processes of luminescence.

In condensed matter systems, however, this idealized landscape becomes more intricate. In solids, the relaxation dynamics are complicated by local disorder and crystal-field effects, which modify transition probabilities and broaden emission lifetimes. Fast, allowed transitions coexist with slower, forbidden processes, making the resulting emission a signature of both the material's electronic state and its structural environment. [166]

Photoluminescence may encompass linear single-photon or complex multi-photon interactions. As illustrated in Figure 2.2, these processes are categorized by the energy relationship between absorbed and emitted photons. Down-shifting refers to the emission of a photon at lower energy than the absorbed quantum. Down-conversion (or quantum cutting) involves the partition of a single high-energy photon into two or more lower-energy photons. Conversely, up-conversion utilizes the sequential or cooperative absorption of multiple low-energy photons to generate higher-energy emissions. These spectral management strategies are foundational to modern optoelectronics, including LEDs, lasers, displays, and advanced photovoltaic devices. [166]

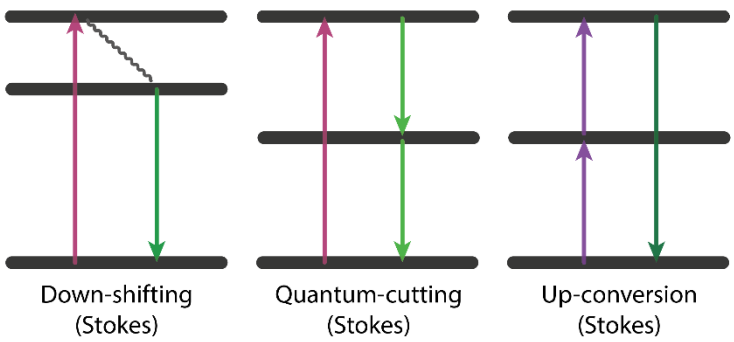


Figure 2.2 Fundamental photon processes of photoluminescence.

Since a portion of the excitation energy is typically dissipated into the lattice as phonons (often driven by the solid-state interactions), the emitted photon carries less energy than the absorbed quantum. This energy offset manifests as the Stokes shift which is a characteristic red shift between the absorption and emission maxima that complies with Stokes' law. Conversely, anti-Stokes emission yields photons of higher energy than the excitation source (e.g., up-conversion), enabled by the system extracting thermal energy from the lattice. [166]

A fundamental metric for evaluating these materials is the photoluminescence quantum yield, PLQY, defined as the ratio of emitted photons to absorbed photons. When combined with emission lifetime, absorption cross-section, and Stokes shift, the quantum yield provides a comprehensive figure of merit for assessing the performance metrics of luminescent materials for optoelectronic applications. [166]

2.2 Luminescent Materials

Photoluminescent materials are fundamentally categorized organic and inorganic. Given the scope of this research and the requirement for integration into glass hosts, the discussion prioritizes inorganic emitters over their organic counterparts. Consequently, organic fluorophores are mentioned only briefly, with the primary analysis dedicated to lanthanide ions and quantum dots. [166]

2.2.1 Lanthanides (Rare-Earths)

Lanthanide elements (atomic numbers 57–71) typically exhibit luminescence in their trivalent form, Ln^{3+}. In this configuration, the optically active 4f electrons are shielded by filled $5s^2$ and $5p^6$ subshells. This outer electrostatic buffer effectively isolates the 4f manifold from the surrounding electronic field. Consequently, the energy levels of 4f electrons remain quasi-atomic, exhibiting only modest Stark splitting and weak electron-phonon coupling. This unique shielding is responsible for the hallmark features of lanthanide luminescence: remarkably narrow, spectrally pure emission lines and high thermal stability, distinguishing them from most other solid-state emitters. [167]

The complex network of energy levels characteristic of lanthanides is systematized in the Dieke diagram (Figure 2.3). Originally compiled by G. H. Dieke, this diagram consolidates the experimentally observed energy levels for trivalent ions ranging

from Pr^{3+} and Yb^{3+}. It serves as an essential tool for interpreting lanthanide spectroscopy, enabling the rapid identification of allowed transitions, resonance conditions, and potential energy transfer pathways. [168]

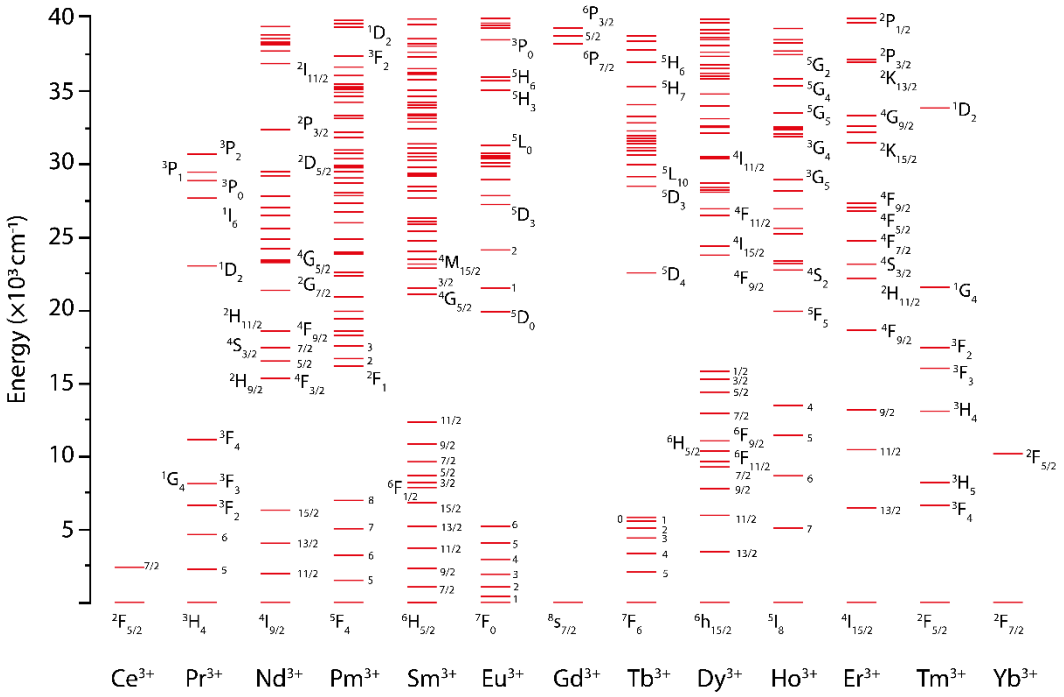


Figure 2.3 Dieke diagram showing calculated energy levels of Ln^{3+} ions, adapted from the reference. [169]

The intensity of 4*f*–4*f* transitions is governed by quantum mechanical selection rules, specifically the Laporte rule, which forbids electric-dipole transitions between states of the same parity (e.g., $f \rightarrow f$). Since both initial and final states typically possess odd parity, pure electric-dipole transitions are formally forbidden and intrinsically weak. However, in condensed matter, local site asymmetrical perturbs the metal center, mixing the 4f states with opposite-parity configurations (e.g., 5*d*). This mixing relaxes the selection rule, enabling "forced" electric-dipole transitions. Consequently, lanthanide ions embedded in asymmetrical hosts like amorphous glasses or low-symmetry crystals often exhibit emission intensities significantly higher than idealized parity arguments would predict. [167] The intensities of these forced transitions are quantitatively described by Judd-Ofelt theory.

In contrast to the sharp intraconfigurational 4*f*-4*f* lines, interconfigurational $4f \rightarrow 5d$ transitions are parity-allowed and thus exhibit much higher oscillator strengths.

Because the unshielded 5*d* orbitals interact strongly with the ligand environment, these transitions manifest as broad, host-dependent absorption and emission bands, characteristic of ions such as Ce^{3+}, Eu^{2+}, and Pr^{3+}. [167]

A critical limitation for light-harvesting applications is the extremely low absorption cross-section of parity-forbidden 4*f*-4*f* transitions (10^{-22} / 10^{-20} cm^{-2}), which renders direct excitation inefficient. To overcome this, lanthanide ions are frequently sensitized by "antenna" species such as organic ligands, Ce^{3+} co-dopants, or semiconductor hosts, which absorb light efficiently and transfer the excitation energy to the lanthanide center via Förster (dipole-dipole) or Dexter (exchange) mechanisms. [167]

2.2.2 Quantum Dots

Quantum dots (QDs) are semiconductor nanocrystals, typically 2–10 nm in diameter, synthesized from II–VI (CdSe, CdTe, ZnS, ZnSe), III–V (InP, GaP), or IV–VI (PbSe) compounds. Their unique optical properties emerge when the particle dimension approaches the exciton Bohr radius of the bulk material. In this quantum confinement regime, the continuous electronic band structure breaks into discrete, size-dependent energy levels. As crystal size decreases, the effective bandgap widens, allowing for precise tunability of absorption and emission spectra across the visible and infrared regions (Figure 2.4a). [170]

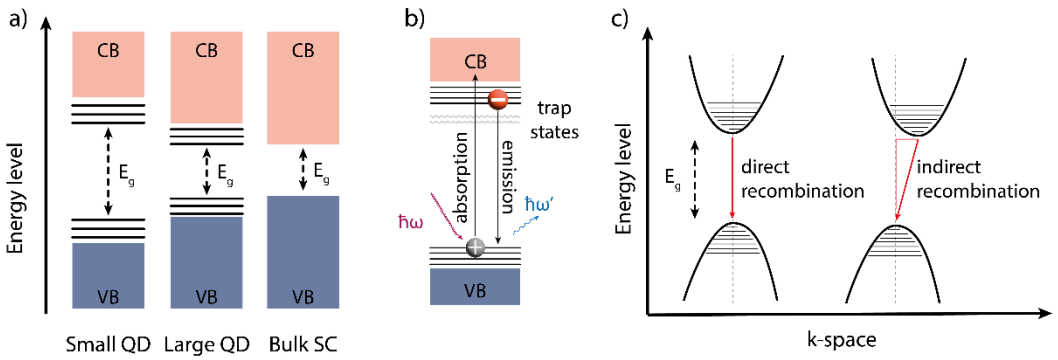


Figure 2.4 (a) Schematic energy diagrams for the electronic structures of atoms, molecules, small and large QDs and bulk semiconductors. (b) Electron-hole pair (exciton) generation, recombination, and photoluminescence emission by a QD. c) Energy level diagram showing direct/indirect band gap structures in momentum space.

Photoluminescence in QDs is initiated by the absorption of a photon with energy greater than the bandgap, generating an electron-hole pair (exciton) (Figure 2.4b). Owing to the nanoscale dimensions of the QD, the exciton is spatially confined within the crystal, ultimately undergoing recombination to emit a quantum. Radiative recombination generates a photon with energy corresponding to the size-modified bandgap. While QDs offer broad absorption profiles ideal for solar harvesting, they typically exhibit small Stokes shifts. This significant spectral overlap between absorption and emission leads to severe reabsorption losses in large-area devices, resulting in redshifted emissions, reduced quantum yields, and shortened effective lifetimes. Strategies to engineer larger "effective" Stokes shifts include the use of core-shell heterostructures, alloyed compositions, or dopant-mediated emissions (e.g., Mn^{2+}-doped QDs). [170]

A notable subclass is metal-halide PQDs ($CsPbX_3$, where X = Cl, Br, I), which have garnered intense interest due to their defect-tolerant electronic structure and near-unity photoluminescence quantum yields. Unlike traditional chalcogenide QDs, PQDs possess a direct bandgap (see Figure 2.4c) that facilitates rapid radiative recombination without phonon assistance. Their ionic lattice allows for facile synthesis via hot-injection or ligand-assisted reprecipitation and offers broad compositional tunability. [170]

Despite their superior optical metrics, PQDs face significant stability challenges. The ionic nature of the perovskite lattice and the dynamic binding of surface ligands (e.g., oleic acid) make them susceptible to degradation by moisture, heat, and polar solvents. Stabilization strategies include surface passivation with multidentate ligands and encapsulation within robust matrices. Among these, inorganic glass hosts are particularly attractive for optoelectronic applications, offering superior protection against environmental factors compared to polymers. However, encapsulating PQDs in glass presents a processing trade-off: while it maximizes durability, it locks the spectral properties at the synthesis stage, limiting post-fabrication tunability. [170]

2.2.3 Transition Metal Ions

Within the inorganic emitters, transition metal ions (e.g., Cr^{3+}, Mn^{2+}, V^{2+}) offer an alternative luminescence mechanism governed by their partially filled *d*-shells ($3d_n$

configurations). Unlike the shielded *f*-orbitals of lanthanides, the valance *d*-orbitals are spatially extended and interact strongly with the surrounding ligand environment. This interaction is described by crystal field theory, where the local symmetry increases the degeneracy of *d*-orbitals. Consequently, emission arises from two primary pathways, namely ligand-to-metal charge transfer, and *d*-*d* transitions. In prior, fully allowed, high-intensity transitions often found in high-oxidation states (d_0) complexes like vanadate. In the second, often spin-forbidden and parity forbidden transitions results in longer lifetimes. [167]

Crucially, the strong electron-phonon coupling in transition metals results in significantly broadened emission profiles with high full width half maxima (FWHM). While this broadband emission is advantageous for tunable solid-state lasers (e.g., Ti:sapphire) and radiometric sensing in metal oxygen frameworks, it lacks the spectral precision and ease of production required for the specific waveguiding applications targeted in this work, reinforcing the choice of lanthanide and QD platforms. [167]

2.2.4 Organic Emitters

Organic photoluminescence arises principally from π-π^* electronic transitions across the HOMO-LUMO gap (the energy difference between the highest electron-filled orbital and the lowest empty one available for excitation). These materials fall into two classes: intrinsic (natural fluorophores like NADH, flavins, and chlorophyll) and extrinsic (synthetic dyes like rhodamine, fluorescein, and coumarin). Although synthetic dyes exhibit high quantum yields and are indispensable in bio-imaging, they suffer from intrinsic limitations for optoelectronic devices. Their emission typically features small Stokes shifts and susceptibility to photobleaching, the irreversible photochemical destruction of the fluorophore under prolonged illumination. Furthermore, weak van der Waals forces in organic solids often lead to low thermal resistance compared to the rigid lattice of inorganic hosts. [166]

2.3 Luminescent Solar Concentrators

Projections indicate that by 2050, the global population will approach 10 billion, driving a substantial rise in electricity demand due to urbanization, electric vehicle

adoption, and digital infrastructure growth. [1] With fossil fuels still accounting for ~61% of generation (as of 2023), the transition to scalable renewable alternatives is urgent. [2] Among these, solar energy is uniquely abundant, positioning PV technologies at the forefront of the clean energy transition. [3] Silicon-based PVs (Si-PVs) dominate this landscape, offering commercial efficiencies exceeding 20% and sharply reduced costs. [4]

However, conventional Si-PVs require large installation areas, typically in remote locations, which introduces challenges in consistent transmission, grid balancing, and maintenance requirements. [5] While BIPVs aim to decentralize generation by utilizing urban surfaces [6,7], the opaque and rigid nature of traditional panels limits their aesthetic integration. [8] Although various PVs offer significant transparency, color tunability, and geometric flexibility like thin-film devices, wavelength-selective organic or perovskite absorbers, and micro-patterned silicon structures, their active layers still often compromise design freedom because active PV layers and electrical contacts still occupy the visible surface, limiting design flexibility. [9,10]

LSCs offer a fundamentally different solution by decoupling light collection from electrical conversion. As illustrated in Figure 2.5, a typical LSC operates via three coordinated steps: (1) spectral conversion, where luminophores absorb sunlight and re-emit it at longer wavelengths; (2) optical guiding, where a transparent waveguide transports this emission to the perimeter via total internal reflection; and (3) PV conversion by edge-mounted cells. [11]

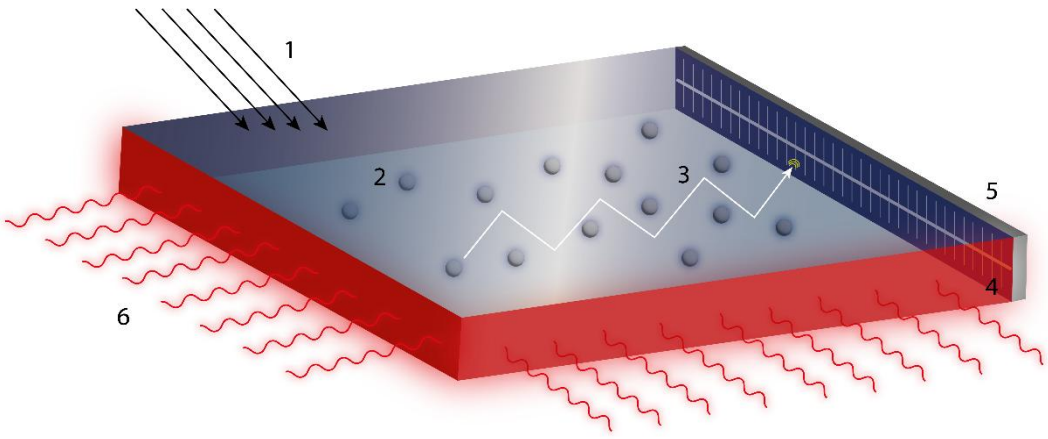


Figure 2.5 Schematic representation of a planar luminescent solar concentrator, illustrating (1) incident light, (2) luminescent centers, (3) total internal reflection,

(4) the waveguide/host medium, and (5) edge-mounted PV cells receiving the guided photoluminescence emission.

Originally conceived in the 1970s to reduce the cost of expensive silicon cells [12], LSCs are now valued primarily for their architectural versatility by confining PV components to the edges, the main surface remains transparent and customizable in color and shape. [12] While various geometries exist, the planar sheet architecture remains the most practical for façade integration and serves as the primary focus of this thesis.

2.3.1 Evaluation of LSCs

The overall efficiency of an LSC is governed by the combined behavior of two subsystems: the photonic collector and the photovoltaic device. The photonic collector determines how effectively incident sunlight is absorbed, spectrally transformed, and guided toward the device edges, where the PV cell converts the guided photon flux into electrical power. Device-level performance therefore reflects the interplay between the optical functions of the luminophores and waveguide, and the electrical characteristics of the PV component. [12,13]

The electrical efficiency of the PV cell is described conventionally by the power conversion efficiency (PCE or η_{pv}), measured under standard test conditions. It is given by

$$\eta_{pv} = \frac{V_{oc}\, I_{sc} FF}{P_{in}} \tag{2.1}$$

where V_{oc} is the open-circuit voltage, I_{sc} the short-circuit current, FF the fill factor, and $P_{\mathrm{in}}$the incident irradiance. [12]

The photonic collector efficiency is expressed in terms of optical power:

$$\eta_{opt} = P_{opt,edge}/P_{opt,in} \tag{2.2}$$

where $P_{\mathrm{opt,edge}}$ is the optical power reaching the waveguide edges and $P_{\mathrm{opt,in}}$ is the total incident optical power. This quantity appears in the literature under several names, such as external photon efficiency, optical efficiency, or optical power efficiency. [12]

The overall electrical efficiency of an LSC device then follows:

$$\eta_{lsc,pv} = \eta_{opt} \times \eta_{pv} \times G \tag{2.3}$$

with $G = A_{\text{lsc}}/A_{\text{edge}}$ representing the geometric gain, defined as the ratio between the device's large-area collecting surface and the total PV-covered edge area. This term converts photon fluxes into equivalent flux densities. [12]

The concentration factor C, a key performance indicator, is defined as

$$C = \eta_{opt} \times G \tag{2.4}$$

which describes how much the effective photon flux density increases at the edges relative to the incident flux. When $C > 1$, the edge-mounted PV cells generate more current than they would under direct illumination, indicating true optical concentration. When $C \leq 1$, the device behaves more as a light guide than a concentrator. [12]

The electrical output of an LSC can be written as

$$P_{lsc,el} = \eta_{opt} \times \eta_{pv} \times P_{in} \times \frac{A_{lsc}^2}{A_{edge}} = C \times P_{ref,el} \tag{2.5}$$

where $P_{\text{ref,el}}$ is the reference power generated by PV cells of equal edge area under identical illumination conditions. [12]

Experimentally, η_{opt} reflects a combination of waveguide losses: reflection, transmission, photon trapping, parasitic absorption, reabsorption, and scattering. Figure 2.6 summarizes the main optical events in a planar LSC—incident light, reflection, transmission, luminophore absorption, host-related attenuation, photoluminescence emission, photon escape through the critical-angle cone, reabsorption cycles, and total internal reflection toward the edges.

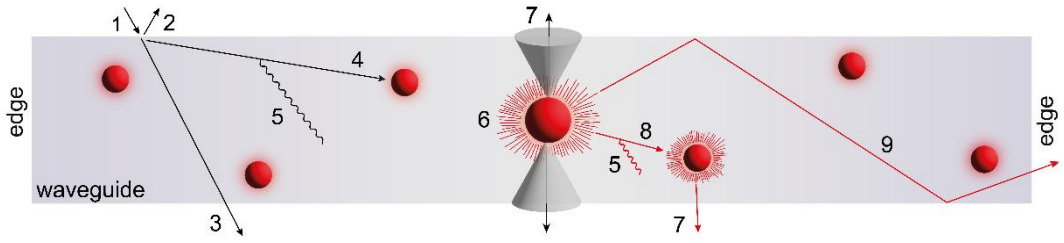


Figure 2.6 Schematic illustration of the glass host and waveguide, showing the main optical processes: (1) incident light, (2) reflection, (3) transmission, (4) absorption, (5) host attenuation, (6) photoluminescence (PL) emission, (7) escape cone, (8) reabsorption, and (9) total internal reflection.

Using the summarized optical events optical efficiency can be written as a weight of all loss mechanisms:

$$\eta_{opt} = (1 - R)\eta_{abs}\eta_{pl}\eta_{ra}\eta_{trap}\eta_{tr} \tag{2.6}$$

Here, R is the Fresnel reflection coefficient; η_{abs} the absorptance; η_{pl} the intrinsic photoluminescence quantum yield; η_{ra} the non-reabsorption factor; η_{trap} the trapping efficiency; and η_{tr} the transport efficiency. [12]

For normal incidence, the reflection coefficient is

$$R = \frac{\left(n_{wg} - n_s\right)^2}{\left(n_{wg} + n_s\right)^2} \tag{2.7}$$

For example, a waveguide with $n_{\mathrm{wg}} \approx 1.5$, the reflection is 4%, and the critical angle becomes $\theta_c \approx 42°$.

Absorptance for monochromatic excitation is given by Beer–Lambert behavior:

$$\eta_{abs} = (1 - e^{-\alpha_1 d}) \tag{2.8}$$

where α_1 is the absorption coefficient and d the slab thickness. [12]

Integrating over the solar spectrum yields

$$\eta_{abs} = \frac{\int \phi_s(\lambda)\left(1 - e^{-\alpha(\lambda)d}\right)d\lambda}{\int \phi_s(\lambda)d\lambda} \tag{2.9}$$

with $\phi_s(\lambda)$ the solar photon-flux spectrum. [12]

In the original formulation of the LSC concept, Weber and Lambe (1976) combined η_{tr} and η_{ra} into a single parameter known as the waveguide transport factor (η_{wg}), defined by the following expression:

$$\eta_{wg} = \frac{1}{1 + \beta\alpha_2 L} \tag{2.10}$$

where α_2 is the absorption coefficient at the emission wavelength, L the waveguide length, and $\beta = 1.4$ represents scattering.

Thus, optical efficiency becomes:

$$\eta_{opt}^{Weber-Lambe} = (1 - R)\frac{\int \phi_s(\lambda)\left(1 - e^{-\alpha(\lambda)d}\right)d\lambda}{\int \phi_s(\lambda)d\lambda}\frac{\eta_{pl}\eta_{trap}}{1 + \beta\alpha_2 L} \tag{2.11}$$

This model tends to deviate from experimental results by approximately +12% to −15% because it assumes that photons lost to reabsorption are completely extinguished. [12]

Klimov later refined the model by including repeated reabsorption–reemission cycles. [171] For a planar luminescent slab with length (L), width (W), and thickness (d), where two edges are coupled to PV cells and the remaining two edges are mirrored, the model is reformulated as follows:

$$\eta_{opt}^{Klimov} = (1-R)\left(1-e^{-\langle\alpha_1\rangle d}\right)\frac{\eta_{pl}\eta_{trap}}{1+\beta\langle\alpha_2\rangle L\left(1-\eta_{pl}\eta_{trap}\right)} \tag{2.12}$$

with spectrally average absorption coefficients

$$\langle\alpha_1\rangle = -\frac{1}{d}\ln\left[\frac{\int_0^{\lambda_g}\phi_s(\lambda)e^{-\alpha(\lambda)d}d\lambda}{\int_0^{\lambda_g}\phi_s(\lambda)d\lambda}\right] \tag{2.13}$$

$$\langle\alpha_2\rangle = \frac{\int\phi_{em}(\lambda)\alpha(\lambda)d\lambda}{\int\phi_{em}(\lambda)d\lambda} \tag{2.14}$$

The resulting concentration factor is

$$C = \eta_{opt}\times G = (1-R)\left(1-e^{-\langle\alpha_1\rangle d}\right)\frac{\eta_{pl}\eta_{trap}}{1+\beta\langle\alpha_2\rangle L\left(1-\eta_{pl}\eta_{trap}\right)}\frac{L}{2d} \tag{2.15}$$

which increases linearly at small L but approaches an asymptotic maximum:

$$C_{max} = \frac{(1-R)}{2\beta\left(\frac{1}{\eta_{pl}\eta_{trap}}-1\right)}\frac{\langle\alpha_1\rangle}{\langle\alpha_2\rangle} = FQ_{lsc} \tag{2.16}$$

with $Q_{\mathrm{lsc}} = \langle\alpha_1\rangle/\langle\alpha_2\rangle$, the effective quality factor. [171]

Notably, when the two reflective edges are replaced with PV-covered edges, an additional loss factor of approximately 0.4 must be considered.

Although analytical models align well with experiments, they exhibit key limitations. They do not account for the gradual red shift of the emission spectrum after successive reabsorption–reemission cycles (generations), which reduces spectral overlap with the absorption profile in later generations. Moreover, they assume a constant QY for each excitation wavelength across the absorption range,

covering even red-shifted reabsorption events. This idealization that does not hold in real systems.

Experimentally determined optical efficiency uses a different relation:

$$\eta_{opt} = (1 - R)\,\eta_{abs}\eta_{pl,waveguide}\eta_{edge} \tag{2.17}$$

In this experimental approach, two main distinctions arise relative to the analytical models: the introduction of an additional parameter, η_{edge}, and the replacement of the intrinsic quantum yield η_{pl} with the waveguide-integrated value $\eta_{\text{pl, waveguide}}$. The parameter η_{edge} consolidates reabsorption, trapping, and transport losses into a single experimentally accessible metric. In parallel, $\eta_{\text{pl,waveguide}}$ reflects the effective external emission efficiency of the luminophore within the waveguide environment rather than its intrinsic QY, also includes the geometrical effects. As device size increases and reabsorption becomes more significant, this modification provides a more realistic estimate of the reduction in the total amount of light escaping from the waveguide. [13]

η_{edge} parameter is obtained from PL intensities measured in an integrating sphere under identical illumination conditions: the unmasked emission spectrum $I_{\text{bulk}}(\lambda)$ and the spectrum recorded with only the lateral edges masked, $I_{\text{surface}}(\lambda)$. It is defined as:

$$\eta_{edge} = \frac{\int I_{edge}(\lambda)d\lambda}{\int I_{bulk}(\lambda)d\lambda} \tag{2.18}$$

with

$$I_{\text{edge}}(\lambda) = I_{\text{bulk}}(\lambda) - I_{\text{surface}}(\lambda)$$

The internal photon efficiency becomes:

$$\eta_{\text{int}} = \eta_{\text{edge}}\,\eta_{\text{pl, waveguide}} \tag{2.19}$$

and the external photon efficiency is:

$$\eta_{ext} = (1 - R)\eta_{\text{abs}}\eta_{\text{int}} \tag{2.20}$$

LSCs function as a type of photovoltaic device, and when evaluated at the system level, the most important and reliable performance metric is integral PCE:

$$PCE_{lsc} = \frac{V_{oc}\, I_{sc} FF}{A_{lsc}\, P_{in}} \tag{2.21}$$

This method allows LSCs of any size to be evaluated straightforwardly. Although the measurement principle appears simple, the procedures reported in the literature vary considerably. The most common mistake is defining the light-collection area as the total area of the edge-mounted PV cells rather than the large top surface of the waveguide. While this assumption follows conventional PV-device measurement practices, it is inappropriate for LSCs, where photon collection takes place at the wide top surface, not at the PV-covered edges. Additionally, the presence or absence of a reflective backing, the number of edges covered with PV cells, and whether any remaining edges are coated with reflective materials all have a significant impact on the measurement outcome. For this reason, the following conditions are recommended to ensure an accurate evaluation of the intrinsic device performance: (1) one or all four edges should be equipped with PV cells, (2) the rear surface and all exposed side facets should be masked with a highly absorbing black material, (3) if the PV cell area is smaller than the waveguide edge area, any uncovered regions must be carefully masked, and (4) the area A_{LSC} must be used in the efficiency calculation. Meeting these conditions isolates the true photonic performance of the LSC and prevents artificially inflated or underestimated values of $\mathrm{PCE_{lsc}}$. [12,13,172]

Another critical performance metric for photovoltaic devices is the spectral response, or external quantum efficiency (EQE). Owing to the multi-component nature of an LSC, the system EQE is expressed as follows:

$$EQE_{lsc}(\lambda) = \eta_{opt} \frac{\int EQE_{pv}(\lambda)\, \phi_{em}(\lambda)\, d\lambda}{\int \phi_{em}(\lambda)\, d\lambda} = \eta_{opt}\, EQE^{*}_{pv} \tag{2.22}$$

Here, EQE^{*}_{PV} represents the average spectral response of the attached PV cell within the emission region of the luminescent centers. This method is well suited for laboratory-scale LSCs and can be used to validate analytically derived optical power efficiencies. However, applying it to large-area LSCs is more challenging. [173]

At the same time, the short-circuit current density of the system can be calculated using the following expression, which provides a useful consistency check against the short-circuit current measured directly from the PV cell: [173]

$$J_{sc} = e \int EQE_{lsc}(\lambda)\, \phi_s(\lambda) d\lambda \tag{2.23}$$

2.3.2 Luminescent Materials for LSCs

The optical performance of an LSC is governed by four intrinsic properties of its luminophores: (1) the absorption cross-section, which dictates light-harvesting efficiency, transparency, and device coloration; (2) QY, representing the radiative efficiency; (3) the Stokes shift, which is critical for minimizing reabsorption losses during waveguiding; and (4) the spectral overlap between the luminophore emission and the responsivity of the edge-mounted PV cells. Over several decades, a wide range of luminophore classes from organic dyes to advanced semiconductor nanocrystals has been developed to optimize these parameters. [13]

Organic Dyes and Aggregation-Induced Emission (AIE) Luminophores

Early LSC studies employed organic dyes such as rhodamines, coumarins, and perylenes. [14,15] These molecules offer high QY and can be easily incorporated into polymer matrices, enabling straightforward device fabrication. However, their applicability is fundamentally limited by narrow absorption bands, small Stokes shifts, the requirement for high loading concentrations to reach sufficient optical density, and photodegredation effect. [16,24–26] In 2008, Sloof et. al reported an LSC device using commercial dyes of Lumogen F Red-305 and coumarin dye Yellow-CRS040, diffuse backside reflector and four GaAs PV cell, yielding PCE of 7.1% with a C = 2.5 at the European Solar Test Installation Laboratories. [17] Similarly, another research using F Red 305 and perylene perione dye with Si cells achieved a PCE of 4.2%. [18]

Thermally activated delayed fluorescence dyes have also been used to broaden the absorption cross-section and enlarge the Stokes shift. [19,20] In this research, PCE values exceeding 2.2% are reported due to the reduced reabsorption losses. Notably, chemically tailored molecules showed relatively superior resistance to photodegredation. [19]

A persistent limitation of conventional dyes is aggregation-caused quenching, where π–π stacking in the condensed phase activates non-radiative relaxation pathways. This challenge motivated the development of aggregation-induced emission luminogens (AIEgens). Propeller-shaped AIEgens such as tetraphenylethene (TPE) are non-emissive in solutions because intramolecular rotations dissipate excitation energy; in the aggregated (solid) state, these rotations are restricted, suppressing non-radiative decay and allowing remarkably high doping concentrations without quenching. For instance, in 2022 Li et al. demonstrated an AIE-based LSC employing 4,4'-(benzo[c]thiadiazole-4,7-diyl)bis(N,N-diphenylaniline), which exhibited a Stokes shift of 0.59 eV and achieved a PCE of 1.4% under 1 sun when coupled to a commercial Si PV cell. [27]

Another strategy to enhance the effective absorption cross-section of organic systems involves energy-transfer schemes, specifically Förster resonance energy transfer (FRET). [28] In 2017, Tummeltshammer et al. reported an LSC in which acceptor luminophores of Alexa Fluor 546 dye are attached to the surface of CdSe-ZNSe core-shell QD donor, achieving a PCE of 2.87%, correspondingly 28% higher than bare QD based LSCs. [29] Shortly thereafter, Zhang and co-workers fabricated a perylene diimide-based donor/emitter luminophore pair, intentionally selected to improve QD of acceptor/emitter Lumogen Red-305 and to reduce reabsorption possibility in PMMA matrix. Eventually, their film-coated PSC-LSC system yielded a PCE of 2.6%, among the best results reported to date. [30]

A related luminophore class is lanthanide antenna complexes (e.g., Eu^{3+} and Tb^{3+} β-diketonates), where organic ligands absorb light and transfer excitation to the lanthanide center via Förster- or Dexter-type mechanisms. These systems provide broadened absorption bands and large pseudo-Stokes shifts, making them promising candidates for LSCs. [21]

Chalcogenide Quantum Dots

Among inorganic luminophores, colloidal QDs represent a major class extensively investigated for LSC applications. [12] Traditional chalcogenide QDs such as CdSe and PbS exhibit size-tunable optical properties due to quantum confinement, enabling control over the absorption onset and emission wavelength to match the solar spectrum and PV bandgap. [31] CdSe QDs can be tuned across visible regions,

whereas PbS QDs enable near-infrared (NIR) emission suitable for Si and CIGS modules. [15] However, core-only QDs typically exhibited moderate PLQYs (10–50%) and small Stokes shifts, promoting reabsorption losses due to surface defect–induced non-radiative recombination. [31]

To increase QY and Stokes-shift core/shell architectures were considered in various LSC applications. [32,33] In such structures, the narrower bandgap core absorbs photons to generate excitons, while the wider bandgap shell passivates surface defects of the core, suppresses non-radiative recombination, improves both QY and photostability, and offers a Stokes shift engineering tool. Carrier confinement within the core results in narrower emission linewidths (reduced FWHM), enhanced emission intensity, and improved chemical and thermal stability. [34,35,40] Representative examples include Stokes-shift–engineered CdSe/CdS QDs with >400 meV Stokes shift and 45% QY (Meinardi et al.), achieved η_{int} of 10.2% and an effective C factor of 4.4. [33] Recently, Gordon et al. proposed CdSe/CdS nanotetrapods with negligible reabsorption but relatively low PLQY (12%), achieving η_{int} of only 5.8%. [36] Then, Song et. Al proposed a seed/quantum-well/thich-shell structure, proposing extremely high QY of 95%. In their research, focus was an increment in trapping efficiency, which increased up to 0.86 by using a top selective reflector system in their LSCs. [37]

In another work, Zhou et al. improved the QY of PbS/CdS QDs to 40–50% and enhanced the Stokes-shift while also broadening the absorption spectrum into the infrared region. [39] In their representative device, they reported an optical efficiency of 6.1% for a geometric factor of 10. Bradshaw et al. further showed that $Cd_{1-x}Cu_xSe$ nanocrystals with PLQYs around 40% can also function as viable LSC luminophores. [38] Despite these advances, the practical deployment of Cd-based QDs remains restricted by modest QYs under operating conditions, limited high-temperature stability [40], and the intrinsic toxicity of cadmium. [41]

Driven by toxicity concerns, research has progressively shifted toward eco-friendly QDs such as $CuInS_2$ (CIS), $CuInSe_2$ (CISe), their alloys (e.g., $CuInSe_xS_{2-x}$), $AgInS_2$, and $CuGaS_2$. These so-called I–III–VI QDs naturally provide broad absorption bands and large Stokes shifts without requiring complex core–shell engineering, and their absorption spectra can span the entire visible range, ensuring excellent spectral overlap with solar irradiance. [46] Li et al. reported LSC devices based on

$CuInS_2$/ZnS core/shell QDs with an intrinsic PLQY of 81% and a Stokes shift exceeding 8.27 eV; in PMMA films the PLQY remained as high as 56%. Their device possessed an optical efficiency of 26.5% excitation of under 460 nm. [42] In 2018, Bergren et al. synthesized $CuInS_2$/ZnS QDs with intrinsic QY of 91%, retaining 66% after film formation. Their 100 cm^2 device exhibited a remarkable η_{ext} of 8.1% and the PCE of 2.2%. [43] Subsequently, Anand et al. reported a 30×30 cm^2 $CuInS_2$/ZnS QDs-based LSCs possessing η_{ext} of 6.8%. [44] Utilizing similar QDs, Macarov et al. reported 15×15 cm^2 devices with PCE values ranging from 1.1% to 4.9% and optical efficiencies between 3% and 13%, corresponding to an AVT ranged of 74% to 5%, respectively. [45]

To enhance absorption, Meinardi et al. incorporated selenium (Se) into I–III–VI QDs, achieving a QY of ~40% and a significant Stokes shift of 0.53 eV Stokes shift. This configuration yielded a η_{ext} of 3.27% for the 12×12×0.3 cm^3 devices. [46] Subsequently, Wu et al. demonstrated $CuInSe_2$/ZnS QD-based LSCs with 65% QY and an enhanced absorption coefficient of 28%. [47] Building on this, Güngör et al. alloyed Zn into $CuInSe_{2-x}S_x$/$CuInS_2$ QDs, achieving a QY of 78% and an exceptionally high η_{ext} of 11.8% in their 9.5×9.5 cm^2 device. [48] More recently, Lai et al. investigated $Cu_{2-x}Se$@SiO_2@$CuInSe_{2-x}S_x$/ZnS core/shell/shell hybrid nanostructures with amplified NIR emission and 78% QY; their highly transparent 6×6 cm^2 LSC exhibited a PCE of 0.23%. [49]

Although I–III–VI QDs exhibit high intrinsic PLQY, their long-term stability in polymer matrices used as waveguides or films is a major concern. Wu et al. addressed this by proposing thiol–ene polymers as host materials, achieving broadened Stokes shifts for $CuInS_2$/ZnS QDs and maintaining 81% PLQY after polymerization. [50] Their 29 × 29 cm^2 prototype delivered a PCE of 1.36% at 51% average visible transmittance (AVT).

Current research efforts are increasingly focused on the practical implementation of LSCs based on these CuIn-chalcogenide QDs, aiming to bridge the gap between laboratory results and real-world applications. [56,57] Siripurapu et al. further demonstrated that this QD family can maintain high stability for two years under exposure to dust, water droplets, and dried deposits. [58]

Other concurrent efforts include substituting Cu with Ag or replacing In with Ga and Al. In 2021, Dhamo et al. fabricated 10.4 × 10.4 cm^2 LSCs using $AgInS_2$/ZnS QDs and reported an internal photon efficiency of 24.1% and a PCE of 3.8%. [52] Meanwhile, You et al. achieved a notably high PLQY of 91% using eco-friendly CuGaAlS/ZnS core/shell QDs; their 100 cm^2 LSC prototype reached a PCE of 4.29%. [53] The same group also reported CuGaS/ZnS QDs with PLQY of 65.4% and CuInGaS/ZnS QDs with PLQY 94.6%. [54] In 2023, Lee et al. showed that $Ag(In,Ga)S_2$–$AgGaS_2$ QDs can reach near-unity QY while maintaining ~95% transparency across the visible spectrum, yielding optical efficiencies approaching 10% in LSC devices. [55]

Carbon Quantum Dots and Si Quantum Dots

Carbon quantum dots (CDs) have recently gained attention as non-toxic, earth-abundant, chemically robust, and low-cost luminophores for LSCs. [74] Their emission can be tuned across the visible spectrum by adjusting particle size, synthesis route, surface chemistry, and dopants, enabling high photoluminescence efficiency. [75] Although CDs exhibit multicolor fluorescence due to π-conjugated carbon cores and quantum confinement, reabsorption losses remain the major limitation in CD-based LSCs. [13]

In the literature, high-efficiency CD-based LSCs are reported for small-area devices. [59–63] Guo et al. achieved exceptionally high performance with yellow-emissive CDs exhibiting 98% QY and a 9.6 eV Stokes shift, yielding 68% internal and 3.1% external photon efficiency in a 5 × 5 cm^2 prototype under 442 nm excitation. [64] Later, Wang and co-workers demonstrated a near-unity QY in a polymer matrix with a 0.64 eV Stokes shift. This configuration yielded ~13.8% optical efficiency and ~4.8% PCE under an irradiance of 80 mW cm^{-2}. [65] Larger-area devices have also shown competitive performance [66,67]: Zhao et al. reported a 10 × 10 cm^2 LSC with a 0.6 eV Stokes shift achieving 0.7% PCE under ambient light, and a 15 × 15 cm^2 device with 65% PLQY and a 0.53 eV Stokes shift delivering 2.2% external photon efficiency and 1.13% PCE. [68,69] Li et al. reported CDs with a 6.4 eV Stokes shift reaching 4.56% optical efficiency and 4.1% PCE in 10 × 10 cm^2 devices under 45 mW cm^{-2} illumination [70], and later demonstrated Ba-doped CDs with a 0.68 eV Stokes shift and 66.8% QY, achieving 6.87% efficiency at 40 mW cm^{-2}. [71]

Another emerging strategy involves the Si doping of CDs. [76–80] For example, gong et al. demonstrated a 15×15 cm^2 device that reached 2.06% overall efficiency under 35 mW cm^{-2} natural light. [72] Most recently, Cai et al. reported a device with boric acid-functionalized graphene CDs with 90% QY and 1.4% PCE in 10×10 cm^2 devices. [73] Importantly, most of these PCE values were measured under ambient natural illumination rather than standard 100 mW cm^{-2} AM1.5G conditions, under which efficiencies decrease. [13]

Another non-toxic QD class is Si-QDs, which offer high QY and large Stokes-shift potential. [84] Due to quantum confinement effects, silicon nanostructures exhibit a per-atom absorption cross-section nearly an order of magnitude greater than that of bulk Si in the 2–3 eV range [85], enabling robust solar harvesting even at low QD loading densities. [81] Furthermore, their absorption and photoluminescence profiles can be precisely tuned across the visible to near-infrared (NIR) spectrum. [86]

Meinardi et al. were the first to implement Si-QDs in LSCs, reporting a PCE of 2.85% for a 144 cm^2 device. [82] Ren et al. later integrated Si-QDs onto a 4×4 cm^2 perovskite solar cell as a spectral converter, achieving a ~6.2% enhancement in PCE. [83]

Although both CDs and Si-QDs are attractive for LSCs owing to their non-toxicity, earth abundance, low cost, and large Stokes shifts they still suffer from limited absorption strength and reduced QY in the NIR. Extending their absorption and emission further into the NIR while maintaining high QY therefore remains a key challenge for next-generation LSCs. [13]

Perovskite Nanocrystals and Quantum Dots

While the exceptional optical properties of perovskite nanocrystals (PNCs) are well-documented, their integration into LSC systems is primarily constrained by reabsorption losses, environmental instability, and structural toxicity. Research in this field has evolved around four key thematic pillars to circumvent these hurdles: Stokes shift engineering (via ion doping or quantum cutting), durability-focused surface passivation, environmental protection through matrix encapsulation, and spectral management using optimized tandem or bilayer architectures. These

strategies have established perovskites as the most popular luminophore type in the LSC field in recent years.

A chronological review shows that in 2017, Meinardi et al. Bypassed reabsorption through Mn-doping, achieving 0.5% η_{ext}, 5.6% η_{int}, and 0.08% PCE in a 25×20×0.5 cm^3 device. [91] That same year, Zhao et al. tuned emission to the solar cell bandgap via a mixed-halide strategy, reporting 2.0% η_{ext}, 5% η_{int}, and 0.57% PCE in a 9×1.3×0.2 cm^3 LSC. [96] During 2018-2019, the quantum cutting mechanism gained prominence; Yb-doped systems generated two photons from one, reaching 3.7% η_{ext} and 118.1% η_{int} with 0.60% PCE in 5×5×0.2 cm^3. [97] Cohen et al. pushed this technology further with a massive 70×70×0.1 cm^3 monolithic bilayer design, reporting 9.0% η_{ext}. [93]

In 2019, Tong et. al. used dicarboxylic acid ligands for room-temperature synthesis of ultra-stable $FAPbBr_3$ achieving 5.88 η_{ext} and 1.03% PCE in 5×12×0.3 cm^3 device. [127] Wei et al. demonstrated ultrafast exciton routing by controlling the layer count in quasi-2D nanoplatelets, reporting 0.87% η_{ext}, 26% η_{int}, and 0.15% PCE in 10×10×0.2 cm^3. [128] Simultaneously, the 1.5 eV Stokes shift of zero-dimensional Cs_4PbBr_6 structures was tested in 10×10×0.4 cm^3 devices with 2.4% η_{ext}, 25% η_{int}, and 1.8% PCE at low light intensities. [88] In 2020, Wu et al. ensured the stability of $CsPbI_3$ nanocrystals even in water through TPP ligand treatment, reaching 3.1% η_{ext} and 36% η_{int} in 2×2×0.2 cm^3 device. [147] Li et al. tailored a multi-quantum well structure in the HA2MA2Pb3I10 trough solvent-solute coordination to reach 2.0% η_{ext} and 0.14% PCE in 10×10×0.2 cm^3 [129], while Cai et al. reported 7.5% η_{ext} and 60% η_{int} for triple-emitting Mn/Yb co-doped systems in 20×20×0.5 cm^3. [94]

Since 2021, the focus has shifted toward practical applications and hybrid solutions; 2.11% η_{ext} and 1.06% PCE were reported in 6×6×0.5 cm^3 using thiol-ene polymers [139], and a 2.87% η_{ext} were achieved in 10×10×0.2 cm^3 via plasmonic gold nanoparticles. [98] Bhosale et.al. were tested flexible panels at 2.8×2.5×1.4 cm^3 with 8.0% η_{ext} [174], and then Liu et al. were integrated 0D structures into real devices for a 1.10% PCE in 5×5×0.4 cm^3. [90] In 2022, electrospun nanofibers yielded 12.26% η_{ext} and 2.35% PCE in 5×5×0.45 cm^3 [132], while encapsulation in glass matrices provided 6.17% η_{ext} in 2×2×0.2 cm^3 device. [161] Lead-free

$Cs_3Cu_2Cl_5$ systems reported a 1.80% PCE in 8×8×0.5 cm^3. [99] Wei et al. demonstrated scalability with massive 40×40×0.5 cm^3 Mn-doped panels reaching 11.0% η_{ext} and 47% η_{int}. [123] Finally, in 2024, Xia et al. reached 7.2% η_{ext} and 1.40% PCE using an advanced structure with an optical spacer layer in 5×5×0.3 cm^3 dimensions. [100]

In conclusion, the heavy clustering of contemporary research around perovskite nanocrystals has made them the most popular luminophore class in the LSC field. However, an analysis of the reported data reveals significant discrepancies, with some studies showing very high optical efficiencies alongside low PCE values, and vice versa. This inconsistency clearly demonstrates that even today, there is no complete consensus on evaluation protocols or performance reporting standards for LSC devices, highlighting the urgent need for a standardized methodology in the field.

Scattering-Enhanced and Tandem LSC Architectures

To further enhance photon transport to the PV cells, an additional strategy involves incorporating scattering materials into the waveguide. [101,102] For example, Jin et al. embedded microfibrillated cellulose and CDs into a PMMA matrix; the scattering induced by cellulose improved light trapping, enabling 18.07% optical efficiency and 8.61% PCE. [103] On the other hand, additional scattering centers tend to disrupt the internal reflection mechanism, leading to increased optical losses. Consequently, this effect remains a major constraint for the practical implementation of wide-area systems.

Recent years Tandem LSCs using different luminophores that are strategically arranged in separate layers to absorb distinct portions of the solar spectrum have emerged. [104–106]

In this route, research is mainly on CD-based systems, possibly because they can by synthesized in very different colors. For example, among representative studies, Zhou et al. reported a CD/PVP tandem film-based LSC (100 cm^2) with 1.1% optical efficiency. [66] In 2020, Zdrazil and co-workers fabricated tandem LSCs comprising blue, green, and red CDs; their 64 cm^2 devices achieved 2.3% external photon efficiency. [108] In the same year, Wang et al. reported a 5×5 cm^2 tandem LSC based on green, yellow, and red CDs, achieving PCEs up to 2.92%. [109] In

2021, Li et al. demonstrated red–yellow CD-based tandem LSCs with 3.8% PCE in 100 cm^2 devices [110], while Han and co-workers reported 2.3% PCE for devices employing red- and green-emissive CDs. [111]

Hybrid tandem architecture combining CDs with other luminophore classes have also been realized. In 2018, Zhao et al. reported a 100 cm^2 device incorporating CDs and inorganic mixed-halide perovskite QDs, achieving ~3% η_{ext}, and 0.41% PCE in 10×10×0.2 cm^3 dimensions under standard solar illumination. [112] In 2019, Ma et al. demonstrated a tandem LSC (2.5×2 cm^2) combining AIE molecules, TPFE–Rho dye, and N-doped CDs, achieving 4.06% PCE. [115] Chen et al. subsequently reported semi-transparent tandem LSCs (5×5 cm^2) based on Cu_4I_6(pr-ted)$_2$ nanoparticles with QY of 92.2% and CDs with QY of 91.1%, reaching optical efficiencies of ~6.4%. [113]

Tandem concepts have also been extended to I–III–VI QDs. For example, Wu and co-workers layered Mn^{2+}-doped $Cd_xZn_{1-x}S$ QDs and $CuInSe_2$/ZnS QDs, attaining 6.4% external photon efficiency and 3.1% PCE under daylight conditions. [47] In 2023, Zhi et al. combined $CuGaS_2$/ZnS QDs (PLQY of 65.4%) with $CuGaInS_2$/ZnS QDs (PLQY of 94.6%) in a tandem LSC, reporting a PCE of 0.99%. [54]

While the quest for ideal LSC luminophores has accelerated through innovative breakthroughs in materials science, no single class of materials has concurrently satisfied the multi-faceted criteria of superior optical performance, long-term durability, and cost-effective scalability, yet.

2.4 Host-Waveguide Selection for LSCs

The overall efficiency of a LSCs is contingent not only upon the luminophore itself but also on the medium in which it resides. In practice, this medium performs a critical dual function: it acts as the chemical host that determine spectral properties and stability of the emitters and, simultaneously, as the optical confinement media. [116] Depending on the specific device architecture, the roles of "host" and "waveguide" may be fulfilled by a single material or distinct components; yet, in all configurations, their properties are intrinsic to the effective performance of the luminophore. Despite this constructive interaction, the majority of LSC research has focused on tailoring emission properties, frequently treating the host matrix as

a passive background and overlooking its pivotal role in device-level operation. [12,13,116,119–122,175]

From an optical perspective, the refractive index of the host dictates the critical angle and, by extension, the escape cone which is the solid angle encompassing emission trajectories that fail to undergo total internal reflection and are lost from the device. Increasing the refractive index narrows this cone, thereby mitigating escape losses and enhancing photon confinement. Chemically, the host serves as a barrier, isolating luminophores from moisture, oxygen, and reactive species to suppress degradation and aggregation-induced quenching. Consequently, the emitter and its environment cannot be optimized in isolation; rather, they constitute a coupled design space where photophysics, photon transport, and material stability must be engineered concurrently. [118]

Structurally, strategies for integrating luminophores into LSC architecture are primarily categorized into two approaches: (1) Surface-coated systems involve depositing a thin luminescent film onto a transparent substrate, such as glass or PMMA. While these coatings offer ease of emitter manipulability, fabrication, and design flexibility, they are prone to long-term instability caused by surface abrasion, delamination, and UV-induced degradation. Furthermore, refractive index mismatches at the film-substrate interface can potentially increase scattering losses. Sandwich-type encapsulation mitigates environmental exposure; however, it also introduces additional optical interfaces, random reflections, thermal expansion mismatches, and increased fabrication costs.

In contrast, monolithic bulk systems incorporate the luminophore directly into the optical medium, creating a unified host–waveguide structure that minimizes internal interfaces and interface-related scattering. This approach, however, necessitates a matrix material that simultaneously possesses all required properties for an LSC, such as high transparency, an appropriate refractive index, chemical compatibility with the emitter, and adequate mechanical strength. While sharing the volumetric nature of bulk systems, liquid LSCs constitute a separate class where luminophores are dissolved in a transparent cell. [123] Despite offering superior optical uniformity, they are inherently limited by risks of leakage, solvent evaporation, and seal failure under thermal cycling, restricting their utility primarily to laboratory-scale demonstrations rather than practical deployment.

Historically, polymers have dominated all LSC research by means of host media due to their low cost and processing versatility. [124] PMMA is the ubiquitous host of choice, owing to its high visible transparency (~90%) and moderate refractive index (~1.49). [21,95,106,125–134] While standard polymers like PDMS [92,107,135,136], PS [88,90,137], resins [138–141], PU [147], PLA [148], EVA [149], PVDF [150,151], elastomers [152], and PVB [22] have been widely utilized, sol-gel derived organic-inorganic hybrids and film-formers (e.g., ureasils and bridged silsesquioxanes) [114,142–146] have been studied.

Nevertheless, polymer-based LSCs face a fundamental processing–performance trade-off: scalable techniques like hot-melt extrusion require elevated temperatures that may degrade sensitive luminophores (e.g., colloidal QDs, hybrid perovskites), whereas low-temperature solution casting preserves emitter photophysics but is labor-intensive and difficult to scale. [26,153,154] Moreover, organic polymers are intrinsically susceptible to photo-oxidation and thermal aging, which severely limits their long-term stability in outdoor BIPV environments. [155] Glass, in contrast, offers superior protection for emitters due to its durability, thermal stability, and chemical resilience, while also providing excellent optical properties. [156,157]

The integration of luminophores into glass matrices imposes specific constraints. The elevated temperatures required for melt-quenching preclude the use of organic antenna ligands essential for sensitizing lanthanides; consequently, lanthanide-doped glasses remain limited by low absorption cross-sections. As a result, most studies on lanthanide–glass systems have been confined to spectroscopic analysis, with no translation into fully characterized LSC devices. For semiconductor QDs, incorporation into glass typically requires direct formation within the matrix via in situ precipitation during melt-quenching or sol–gel processing. [156] This requirement restricts compositional freedom and limits the ability to tailor surface chemistry.

Early proof-of-concept demonstrations, such as femtosecond-laser-induced perovskite QD formation in glass, confirmed the viability of PQD–glass LSCs but suffered from low efficiencies due to non-uniform nanocrystal distributions. [159,160] Subsequent advancements, including ultrathin $CsPbBr_3$-based PQD–glass sheets [161] and PbSe QD–glass composites [162], have improved optical

uniformity and transparency. However, challenges related to large-area processing, mechanical robustness, and scalable fabrication persist. Beyond these specific examples, the literature on bulk-doped glass LSCs remains notably sparse compared to polymeric systems.

Collectively, the host-waveguide is not a passive vessel but a critical design component that dictates LSC performance. While bulk-doped glasses offer a unique combination of optical efficiency and the stability required for architectural integration, the relationship between glass composition, processing conditions, and luminophore behavior is not yet fully understood. This research fills this gap by systematically exploring glass-based LSC platforms. By establishing design rules that balance emission properties with host constraints, this study aims to transition from lab-scale prototypes to scalable BIPV technologies.

2.5 PVs Used for LSCs

The performance of any PV device is fundamentally quantified by its EQE, defined as the ratio of collected charge carriers to the number of incident photons at a specific wavelength. For conventional solar modules operating under the terrestrial AM1.5G spectrum, the primary design objective is to maximize the integrated EQE across the broadest possible bandwidth spanning from the ultraviolet (UV) to the NIR to ensure high PCE. [176]

However, integration within an LSC architecture necessitates a fundamental shift in design. [26] Since edge-mounted cells are driven by narrow-band fluorescence rather than broadband sunlight, the primary design objective is to align the PV cell's peak responsivity with the luminophore's specific emission profile, rather than maximizing total spectral width. As illustrated in Figure 2.7, current PV technologies offer distinct trade-offs in this context:

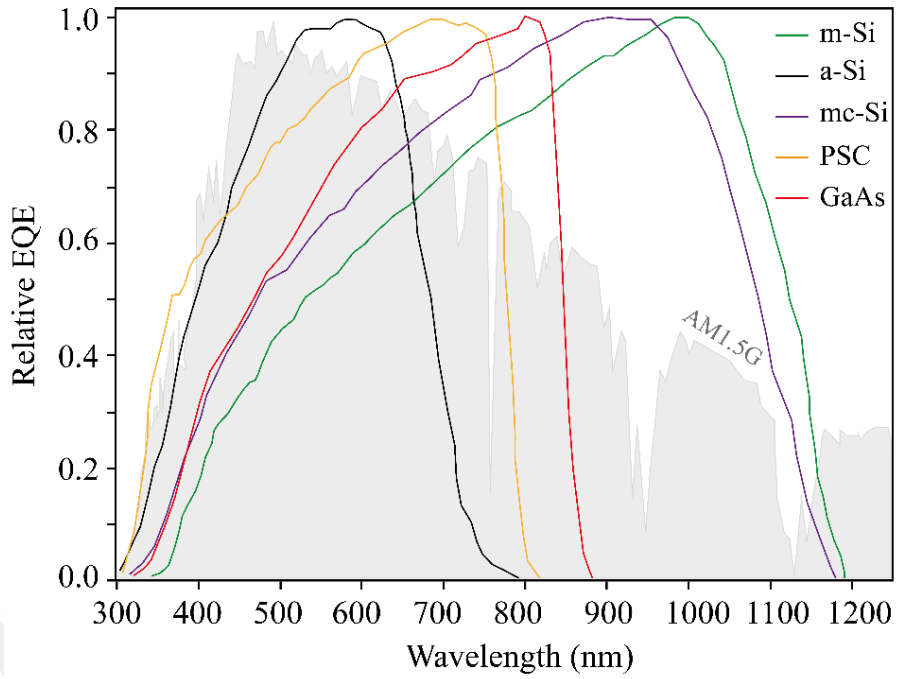


Figure 2.7 Normalized EQE spectra of some PV cell types.

The selection of the photovoltaic (PV) cell is a critical determinant of LSC performance, representing a strategic trade-off between technological maturity and spectral alignment. Whether it changes slightly for monocrystalline (m-Si), amorphous (a-Si), or multicrytalline (mc-Si), Silicon (Si) cells have a peak sensitivity in the red/NIR region (1.12 eV) that often misaligns with visible luminophores, remains the ubiquitous choice for LSC prototypes due to its cost-effectiveness and industrial maturity. In contrast, III-V semiconductors such as GaAs and InGaP offer near-ideal spectral matching and superior conversion efficiencies; however, their prohibitive fabrication costs largely confine them to high-performance proof-of-concept devices. Emerging as a compelling alternative, Perovskite Solar Cells (PSCs) present a unique advantage through their chemically tunable bandgaps, allowing for precise spectral matching, yet their practical application remains hindered by long-term instability. Ultimately, while III-V materials hold the lead in theoretical efficiency, silicon continues to serve as the standard pragmatic solution by offering the optimal balance between performance, integration flexibility, and affordability. [117]

3
EXPERIMENTAL STUDIES

3.1 Sample Preparation

Two distinct series of luminescent glass-based matrices were prepared for this study using the conventional melt-quenching technique: Eu^{3+}-doped oxide glasses and $CsPbBr_3$ PQD GNCs.

Analytical-grade raw materials (≥99.9% purity) were sourced from Sigma-Aldrich and Alfa Aesar and used without further purification. The precursors included $CaCO_3$, ZnO, Al_2O_3, H_3BO_3, SiO_2, Na_2CO_3, PbO, Eu_2O_3, NaBr, $PbBr_2$, and Cs_2CO_3. For both glass systems, the stoichiometric amounts of precursors were weighed with high precision and thoroughly homogenized in an agate mortar.

The host composition of Eu^{3+} doped glasses was selected as $5CaO–3PbO–6Na_2O–12ZnO–2Al_2O_3–32B_2O_3–40SiO_2$. Different concentrations of Eu_2O_3 (x = 0, 0.25, 0.5, and 1 mol%) were incorporated, corresponding to approximately 1.06, 2.13, and 4.26 wt.% Eu^{3+} in the final glasses. The batches were melted in a platinum crucible at 1250 °C for 2h. To ensure compositional homogeneity, the melting–casting–grinding cycle was repeated several times.

The precursor glass batches for $CsPbBr_3$ PQD-GNCs corresponded to a nominal molar composition of $5CaO–12ZnO–2\ Al_2O_3–30\ B_2O_3–35\ SiO_2–(6NaBr–3PbBr_2–7Cs_2O)$. The mixtures were melted in alsint crucibles at 1200 °C for 20 minutes under ambient atmosphere.

Following the melting stage, the viscous melts were poured onto preheated stainless-steel plates and rapidly quenched. To relieve thermal stress, all as-cast samples were immediately transferred to an annealing furnace at 450 °C for 5h and subsequently cooled slowly to room temperature.

While the Eu^{3+}-doped glasses required no further thermal processing, the precursor glasses for the GNCs underwent controlled heat treatments to promote nanocrystal (PQD) formation. Based on optimization studies, these glasses were heat-treated between 510 and 570 °C (in 10 °C steps) for 4h. The optimal crystallization condition was identified as 540 °C for 4 h, which was used for the fabrication of LSC devices.

All annealed and heat-treated samples were cut, ground, and optically polished to a uniform thickness of 2.5 mm. To assess the size-dependent performance in LSC configurations, samples were fabricated in varying geometries: 2×2 cm^2, 4×4 cm^2, and 6×6 cm^2 for the Eu^{3+}-doped series (specifically for the 0.5 mol% composition), and ranging from 1×1 cm^2 to 5×5 cm^2 for the $CsPbBr_3$ GNCs (heat treated at 540 °C for 4 h).

The stepwise manufacturing process is illustrated in Figure 3.1. While the first two stages are common to both Eu^{3+}-doped glasses and PQD-GNCs, the final procedure is exclusive to the PQD-GNC samples.

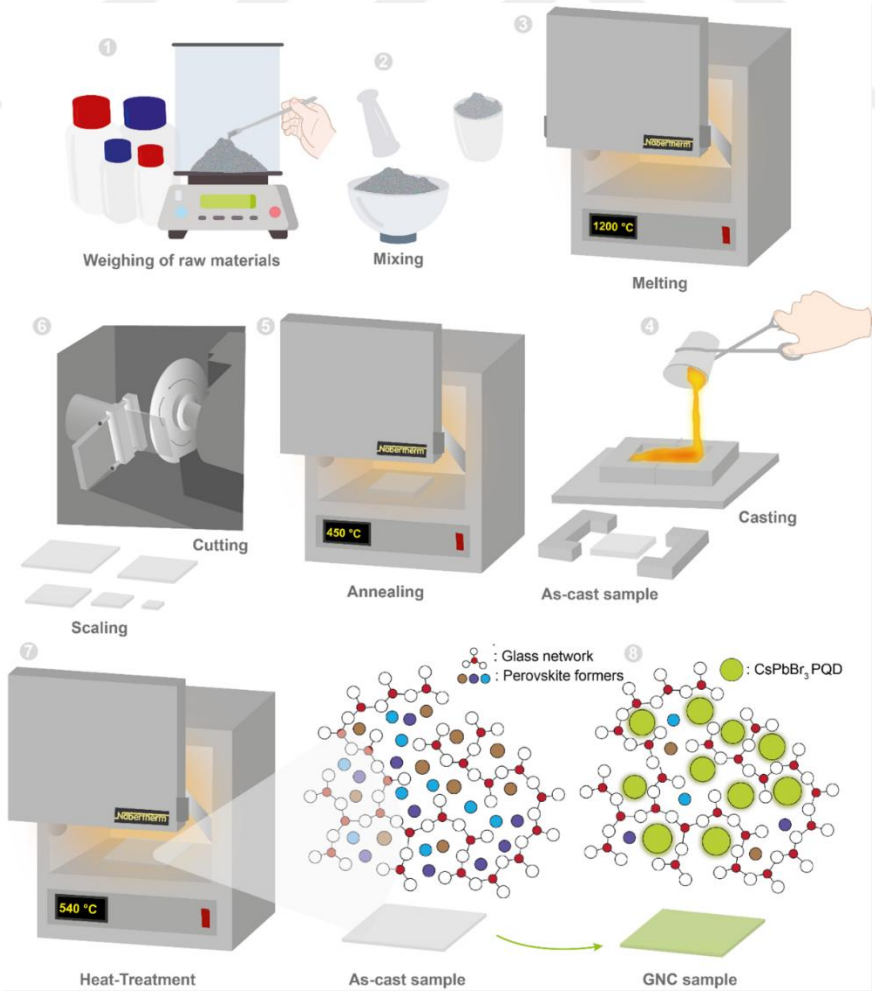


Figure 3.1 Schematic representation of the fabrication workflow for Eu^{3+}-doped and PQD GNC–LSC specimens follows a shared route of melt-quenching, annealing, and mechanical shaping. A distinctive secondary thermal treatment is applied exclusively to the PQD-GNC samples to trigger the in-situ growth of perovskite nanocrystals, thereby defining their final optoelectronic properties.

3.2 Characterization Studies

3.2.1 Thermal and Structural Characterization

Thermal characteristics of the glass samples were analyzed using a Netzsch STA 449 F3 Jupiter simultaneous thermal analyzer. Finely powdered samples (25 ± 1 mg) were sealed in aluminum pans and heated at a rate of 10 °C min^{-1} under a continuous argon flow to determine the glass transition temperature (T_g) for all samples, as well as crystallization onset (T_c) and peak (T_p) temperatures for the GNC precursor glasses. The amorphous nature of the host matrices and the crystalline phases in the PQD-GNCs were investigated by X-ray diffraction (XRD) using a Malvern PANalytical Empyrean Multicore system equipped with Cu K_α radiation (λ = 0.15418 nm, 45 kV, 40 mA). Diffraction data were collected with a step size of 0.02° over the 2θ range of 10°–90° for the Eu^{3+}-doped glasses and 10°–50° for the PQD-GNCs. To further characterize the formation and size distribution of $CsPbBr_3$ nanocrystals, transmission electron microscopy (TEM) was employed. Heat-treated GNC samples were gently crushed to yield electron-transparent fragments, suspended in ethanol, and deposited onto holey carbon-coated copper grids. Imaging was performed on a Thermo Fisher Scientific Talos F200X microscope operated at 200 kV.

3.2.2 Optical and Spectroscopic Characterization

Optical absorbance and transmittance spectra were recorded using an Edinburgh Instruments DS5 UV–Vis spectrophotometer. For the PQD-GNCs, the direct optical bandgaps (E_g) were calculated using the Derivative Absorption Spectrum Fitting (DASF) method by plotting $d[\ln(A(\lambda)\,\lambda^{-1})]/d\lambda^{-1}$ versus λ^{-1}. [177] To corroborate the nanocrystal radii (r), the Effective Mass Approximation (EMA) was applied:

$$E_g(r) = E_{g,bulk} + \frac{h^2}{8r^2}\left(\frac{1}{m_e^*} + \frac{1}{m_h^*}\right) - \frac{1.8e^2}{4\pi\varepsilon_0\varepsilon_r r} \qquad (3.1)$$

where, $E_{g,bulk}$ ($CsPbBr_3$: 2.3 eV) is the bulk bandgap, r is nanoparticle radius, m_e^* ($CsPbBr_3$: $0.15m_e$) and m_e^* ($CsPbBr_3$: $0.14m_e$) are the effective mass of electrons and holes, respectively. ε_0 is the vacuum permittivity, ε ($CsPbBr_3$: 4.797) is the relative permittivity, h is Planck's constant, and e is the charge of the electron. [158]

Steady-state photoluminescence (PL) spectra were acquired using an Edinburgh Instruments FS5 spectrofluorometer equipped with a 150 W xenon lamp. PLQY measurements were performed using a 150 mm PTFE-coated integrating sphere under diffuse excitation to minimize angular dependence (uncertainty ±5%). Excitation wavelengths were set to 393 ± 1 nm for Eu^{3+} glasses and 360 nm for GNCs. Time-resolved PL decay curves were collected via time-correlated single-photon counting (TCSPC). Eu^{3+} samples were excited using a microsecond pulsed lamp at 393 nm, while GNCs were excited with a 450 nm pulsed laser (56.5 ps pulse width). All decay traces were fitted with a bi-exponential function:

$$I(t) = A_1 e^{-\frac{t}{\tau_1}} + A_2 e^{-\frac{t}{\tau_2}} \tag{3.2}$$

where A_1 and A_1 are decay constants and τ_1 and τ_2 correspond to the short- and long-lived decay components. The average lifetime (τ_{ave}) was calculated as:

$$\tau_{meas} = \frac{A_1\tau_1^2 + A_2\tau_2^2}{A_1\tau_1 + A_2\tau_2} \tag{3.3}$$

For LSC performance assessment, edge-emission spectra as a function of propagation distance were collected using a CNI Arora 4000 high-resolution spectrometer coupled to a 0.5 cm core cosine collimator attached 200 µm core fiber. Refractive indices were measured at 520 nm using an Abbe refractometer. Additionally, Average Visible Transmittance (AVT) and Color Rendering Index (CRI) values were derived from transmission spectra according to CIE 13.3-1995 and CIE 15:2018 standards.

3.2.3 Stability and Mechanical Tests

Temperature-dependent PL and thermal cycling experiments (up to 200 °C) were conducted using a Pike Technologies heated transmission stage integrated with the FS5 spectrofluorometer. Photostability was assessed by continuously exposing the samples to excitation light (393 nm for 50 h for Eu^{3+}-doped glasses; 360 nm for 60 h for PQD-GNCs) and monitoring the emission intensity periodically. Chemical

durability was evaluated by immersing samples in deionized water at ambient temperature for 30 days (Eu^{3+}-doped glasses) or 60 days (PQD-GNCs), with degradation monitored via optical transmittance and PLQY. Mechanical properties were probed using a Vickers microhardness tester (DHV-1000(Z)). Five non-overlapping indentations were made per sample under loads ranging from 100 to 1000 gf with a dwell time of 30 s.

3.2.4 Photovoltaic Device Characterization and Simulation Studies

To evaluate the electrical performance of LSC devices, monofacial PERC silicon solar cells were laser-cut into strips (8×1 cm^2) and coupled to the edges of the waveguides. For the GNC devices, a custom 3D-printed holder was used to block extraneous light. Current–voltage (I-V) characteristics were recorded using Keithley sourcemeters (Model 2410/2400) in conjunction with Newport class ABA solar simulators under AM 1.5G illumination (100 mW cm^{-2}). Finally, to extrapolate experimental results to larger PQD-GNC waveguide dimensions (up to 1×1 m^2), a modified Monte Carlo ray-tracing simulations were performed (see Figure 3.2), utilizing 10^5 photons. Within the refined model, the emission characteristics of successive absorption-reabsorption events were re-determined from path-length-dependent PL spectra, while incorporating a wavelength-dependent PLQY distribution function for each subsequent generation.

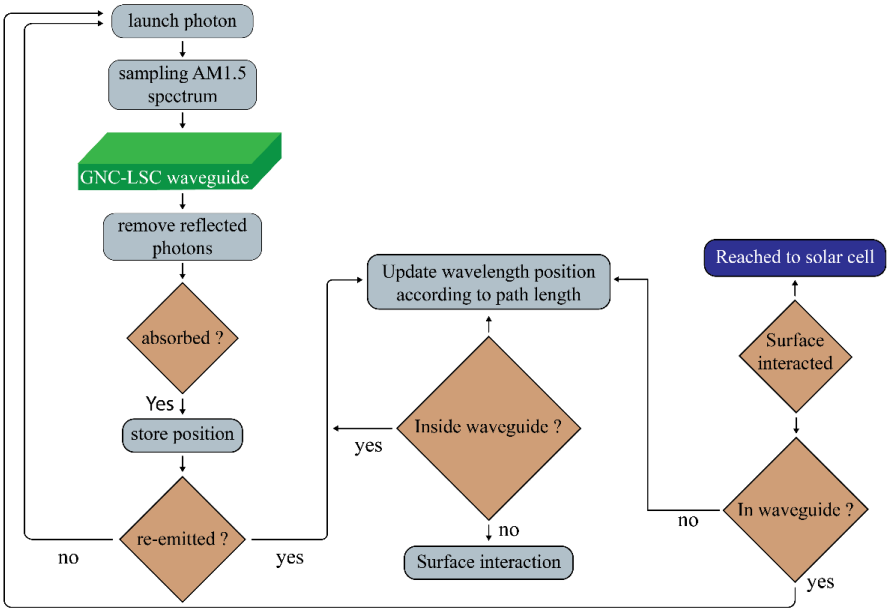


Figure 3.2 Flowchart of the Monte Carlo ray-tracing model.

4
Eu^{3+}-DOPED GLASS-BASED LSCs

Motivated by the need for aesthetically unobtrusive energy-harvesting windows, this study evaluates Eu^{3+}-doped glass LSCs as a superior alternative to polymer-based counterparts. The central aim is to validate a material system that maintains high visible transmittance and color neutrality without compromising optical efficiency or long-term durability.

4.1 Thermal, Structural, Optical and Photoluminescence Properties

The thermal properties of the glasses were examined using STA to assess their thermal stability and define appropriate annealing conditions, which are critical for subsequent cutting and sizing processes. The representative 0.50 mol% Eu^{3+}-doped glass exhibited a glass transition onset (T_g) at 523 °C (Figure 4.1a). Accordingly, annealing was performed at 450 °C for 5 hours, sufficiently below T_g to prevent crystallization. The STA profiles confirmed that the Eu^{3+}-doped glasses retained high thermal stability and structural integrity at temperatures compatible with BIPV operating conditions. The amorphous structure of the samples was verified by XRD, where the 0.50 mol% Eu^{3+}-doped glass displayed a broad diffuse halo without distinct diffraction peaks (Figure 4.1b), confirming the absence of crystalline phases.

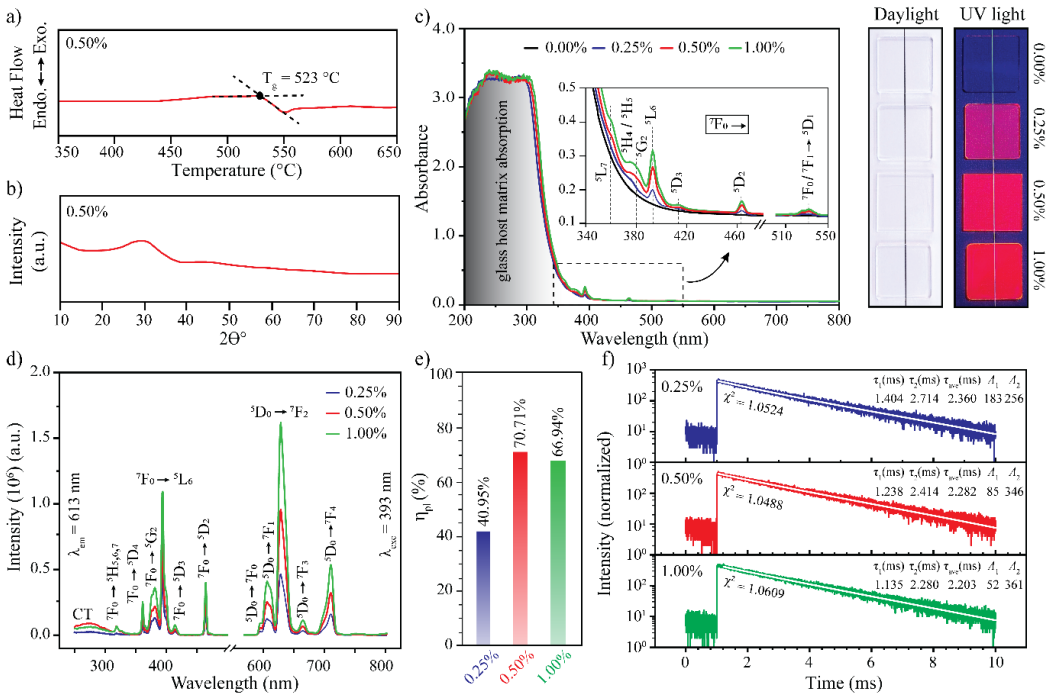


Figure 4.1 (a) STA curve of the glass sample containing 0.50 mol% Eu^{3+}, illustrating its thermal transition behavior. (b) XRD pattern of the same composition, confirming the amorphous structure through the presence of a broad diffuse halo. (c) UV–Vis absorption spectra of all synthesized glasses; the inset highlights the weak Eu^{3+} absorption features and includes photographs of undoped and doped samples under ambient light and UV excitation. (d) Steady-state photoluminescence excitation spectra monitored at the 613 nm emission, alongside the corresponding emission spectrum excited at 393 nm for Eu^{3+}-doped glasses. (e) PLQY values measured under 393 nm excitation for samples containing 0.25, 0.50, and 1.00 mol% Eu_2O_3. (f) Time-resolved PL decay traces at 613 nm collected following pulsed excitation at 393 nm.

The optical absorption spectra of all glass compositions are presented in Figure 4.1c. The inset highlights the weak but characteristic Eu^{3+} absorption features that are difficult to distinguish over the full spectrum. On the right, photographs of the undoped and doped glasses under daylight and UV illumination are shown. All samples appeared transparent, colorless, and free of visible imperfections such as bubbles, scratches, or inclusions, indicating high optical quality. Under UV irradiation, the Eu^{3+}-containing samples emitted a uniform and intense red glow, while the 0.25 mol% sample exhibited noticeably weaker luminescence. No

observable scattering or nonuniform emission was detected, confirming that Eu^{3+} ions were homogeneously distributed within the glass network.

A slight redshift of the UV absorption edge was also observed with increasing Eu^{3+} concentration, shifting from about 338 nm for the undoped glass to approximately 340, 342, and 345 nm for 0.25, 0.50, and 1.00 mol% Eu^{3+} doping, respectively. This apparent displacement arises from the gradual increase in the cumulative absorbance of the Eu^{3+} 4*f*–4*f* transitions, which raises the near-UV baseline and effectively shifts the observed edge toward longer wavelengths. [178] The absorption spectra display seven characteristic peaks at 360, 374, 381, 393, 414, 464, and 532 nm, corresponding to the transitions from the Eu^{3+} ground state $^7F_0$ to the excited states $^5L_7$, $^5H_4/^5H_5$, $^5G_2$, $^5L_6$, $^5D_3$, $^5D_2$, and $^5D_1$, respectively. An additional weak transition near 525 nm, assigned to $^7F_0/^7F_1 \rightarrow {}^5D_1$, is also visible. As expected, overall absorbance increased with Eu_2O_3 content, reaching its highest value for the 1.00 mol% sample.

To further explain the excitation mechanisms, PL excitation (PLE) spectra were recorded, allowing detection of Eu^{3+} transitions that are not distinctly observable in absorption. Figure 4.1d shows the steady-state PLE spectra of Eu^{3+}-doped glasses monitored at the 613 nm emission, alongside the emission spectrum obtained under 393 nm excitation. The PLE curves reveal the characteristic 4f–4f transitions of Eu^{3+} ions as well as a broad charge-transfer (CT) band between 250–300 nm, associated with ligand-to-metal transitions. Distinct excitation peaks around 318, 361, 381, 393, 414, and 464 nm correspond to $^7F0 \rightarrow {}^5H_{5,6,7}$, $^7F_0 \rightarrow {}^5D_4$, $^7F_0 \rightarrow {}^5G_2$, $^7F_0 \rightarrow {}^5L_6$, $^7F_0 \rightarrow {}^5D_3$, and $^7F_0 \rightarrow {}^5D_2$ transitions, respectively.

The combined absorption and excitation results highlight the suitability of Eu^{3+}-doped glasses for LSCs intended for BIPV use. As illustrated in Figure 4.1c, the host glass exhibits a sharp UV absorption cut-off (marked region), enabling intrinsic UV-blocking while preserving high visible transparency. The narrow and weak 4f–4f bands of Eu^{3+} maintain optical neutrality under daylight which is an essential property for architectural integration. Together, the glass matrix and Eu^{3+} ions allow partial conversion of UV photons into visible red emission, facilitating solar energy conversion without compromising transparency.

The photoluminescence spectra of the Eu^{3+}-doped glasses reveal five distinct emission bands at approximately 578, 592, 613, 653, and 703 nm, corresponding to the $^5D_0 \rightarrow {}^7F_j$ (J = 0–4) transitions (Figure 4.1d). The dominant peak at 613 nm, originating from the hypersensitive $^5D_0 \rightarrow {}^7F_2$ electric-dipole transition, indicates that Eu^{3+} ions occupy sites lacking inversion symmetry within the glass network. [179] As the Eu_2O_3 content increases from 0.25 to 1.00 mol%, the emission intensity increases steadily due to the higher density of active centers.

Absolute photoluminescence quantum yields ($\eta_{pl,waveguide}$) measured under 393 nm excitation were 40.95%, 70.71%, and 66.94% for 0.25, 0.50, and 1.00 mol% Eu_2O_3, respectively (Figure 4.1e). The maximum QY at 0.50 mol% followed by a slight decrease at 1.00 mol% indicates the onset of concentration quenching at higher dopant levels.

Time-resolved emission analyses were performed for the $^5D_0 \rightarrow {}^7F_2$ transition at 613 nm using pulsed excitation at 393 nm. The corresponding decay traces and bi-exponential fits are summarized in Figure 4.1f. The average lifetime (τ_{ave}), determined using Equations 3.1 and 3.2, decreased from 2.36 ms at 0.25 mol% Eu_2O_3 to 2.20 ms at 1.00 mol%. Combining η_{pl} with τ_{ave} using the relations $\eta_{pl} = k_R/(k_R + k_{NR})$ and $\tau_{ave} = 1/(k_R + k_{NR})$ allowed extraction of radiative and non-radiative decay rates. The radiative rate (k_R) increased significantly from 173 s^{-1} to 309 s^{-1} between 0.25 and 0.50 mol%, while the non-radiative rate (k_{NR}) decreased from 250 s^{-1} to 128 s^{-1} in the same range, confirming that the enhanced η_{PL} arises from more efficient radiative recombination. At 1.00 mol%, k_R slightly decreased to 303 s^{-1} and k_{NR} increased to 150 s^{-1}, consistent with the modest drop in QY due to increased non-radiative losses.

4.2 Photonic Collection, Conversion and Waveguiding Properties

The optical waveguiding characteristics of the Eu^{3+}-doped glasses were examined to determine how effectively emitted photons propagate to the device edges. Emission collected under bulk, surface, and edge geometries provides insight into photon transport and escape pathways within the host. Figure 4.2a schematically outlines the key optical interactions affecting photon confinement and edge emission.

Corresponding PL spectra from these three geometries are shown in Figure 4.2b, together with schematics highlighting the collection areas (in red) and masked regions (in black). These measurements were used to determine the edge photon efficiency (η_{edge}), which represents the fraction of emitted photons reaching the waveguide edges according to Equation 2.18. Under diffuse 393 nm excitation, η_{edge} was measured as 77.60%, 77.49%, and 77.30% for 0.25, 0.50, and 1.00 mol% samples, respectively, demonstrating consistently strong waveguiding performance across all concentrations.

For a photon emitted by an excited Eu^{3+} ion (step ⑥ in Figure 4.2a), total internal reflection occurs when its emission angle is below the critical angle ($\theta_c \approx 38.7°$ for n = 1.60), redirecting it toward the waveguide edges (step ⑨). In an ideal waveguide, approximately 78% of photons would remain trapped. [128] Experimentally, the observed η_{edge} values fall slightly below this theoretical limit. The small discrepancy stems from three loss channels: (i) reabsorption by Eu^{3+} ions (step ⑧), (ii) host-induced scattering and attenuation (step ⑤), and (iii) escape-cone losses (step ⑦). Because the Stokes shift between the dominant excitation ($^7F_0 \rightarrow {}^5L_6$) and emission ($^5D_0 \rightarrow {}^7F_2$) transitions is large (~1.13 eV), reabsorption is minimal. Thus, the slight decline in η_{edge} at higher dopant levels arises from increased scattering by densely distributed Eu^{3+} centers, promoting photon leakage through the escape cone and reducing guided output.

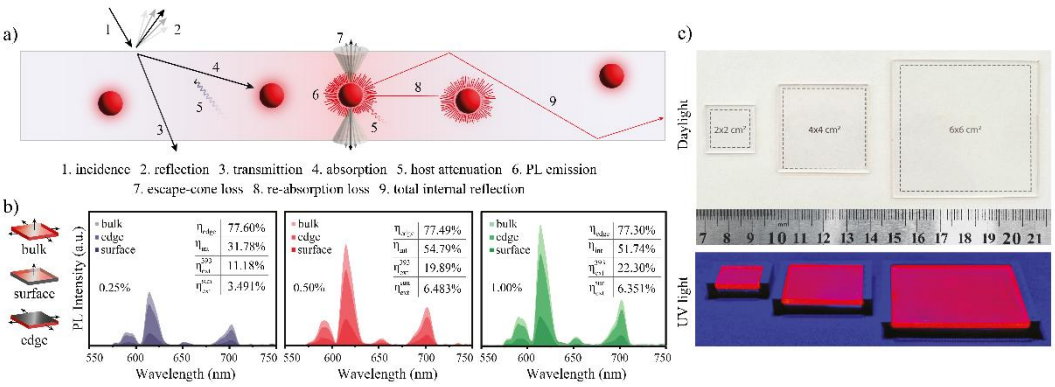


Figure 4.2 (a) Conceptual illustration of the Eu^{3+}-doped glass waveguide showing the principal optical events, including photon absorption, photoluminescence emission, and confinement via total internal reflection. (b) Photoluminescence spectra collected from the bulk, surface, and edge regions using an integrating sphere. The inset tables summarize the extracted η_{edge}, η_{int}, and η_{ext} parameters,

where η_{ext} is calculated for both monochromatic 393 nm excitation and the full AM1.5G solar spectrum. Schematics on the left depict the corresponding detection geometries, with black-shaded areas indicating masked surfaces used to block undesired emission. (c) Photographic images of Eu^{3+}-doped glass waveguides containing 0.50 mol% Eu_2O_3 with lateral lengths of 2, 4, and 6 cm (L = 2, 4, 6 cm), shown under normal illumination and under UV excitation.

To evaluate the combined effect of luminescence yield and waveguiding efficiency, the internal photon efficiency (η_{int}) was calculated using Equation 2.19. The resulting values were 31.78%, 54.79%, and 51.74% for the 0.25, 0.50, and 1.00 mol% samples. This clearly identifies the 0.50 mol% composition as providing the best compromise between emission strength and guided transport. External photon efficiencies (η_{ext}) were then obtained via Equation 2.20. Under the assumption of normal incidence and specular reflection, justified by the high surface quality of the samples, $(1 - R)$ was calculated as 0.9467. Using Equation 2.8, η_{abs} values at 393 nm were determined as 31.28%, 38.39%, and 45.60% for 0.25, 0.50, and 1.00 mol% glasses. Combining these parameters yielded η_{ext} values of 11.18%, 19.89%, and 22.30%, demonstrating a consistent rise in edge-emitted photon flux with increasing Eu^{3+} concentration.

While these values accurately describe monochromatic excitation at 393 nm, real-world LSCs operate under the full AM1.5G solar spectrum. Therefore, η_{ext} must be generalized to account for broadband illumination. The solar-weighted approach defined in Equation 2.9 is widely used in LSC studies, especially for broadband absorbers such as colloidal quantum dots, where the absorber contribution can be isolated from that of the host. However, applying this method to Eu^{3+}-doped glasses introduces complications. The host glass exhibits strong intrinsic UV absorption unrelated to Eu^{3+} emission, and its contribution cannot be removed simply by subtracting an undoped reference because the doped and undoped glasses differ structurally and optically.

Additionally, Eu^{3+} emission stems primarily from the lowest excited state within a given manifold. After absorption through higher-lying 4f–4f transitions, the system relaxes non-radiatively into the $^5D_0$ level, with varying transition-specific efficiencies. To properly capture this behavior, a modified approach was used in

which the intrinsic quantum yield η_{pl} was expressed as a wavelength-dependent function $\eta_{pl}(\lambda)$. [144] In regions where the host absorbs strongly and does not contribute to Eu^{3+} emission—particularly in the UV—$\eta_{pl}(\lambda)$ was set to zero.

This refinement accounts for the selective excitation behavior of Eu^{3+} ions and the parasitic UV absorption of the host, offering a physically consistent evaluation of the solar-weighted external photon output. Accordingly, the generalized η_{ext} was expressed as a wavelength-dependent form:

$$\eta_{ext}(\lambda) = \int \eta_{abs}(\lambda)\eta_{\mathrm{pl}}(\lambda)\eta_{\mathrm{edge}}d\lambda \tag{4.1}$$

In this refined model, $\eta_{abs}(\lambda)$ retains the exponential form given in Equation 2.8 but incorporates the wavelength-dependent absorption coefficient α(λ). The refractive index of the host was taken as wavelength-independent (n ≈ 1.60) across the relevant spectral range, and η_{edge} was assumed constant with respect to wavelength because the guiding environment experienced by emitted photons does not change significantly across the visible band. Using this framework, the wavelength-resolved external photon efficiencies were calculated as 3.491%, 6.483%, and 6.351% for the glasses containing 0.25, 0.50, and 1.00 mol% Eu^{3+}, respectively. The 0.50 mol% composition again delivered the highest photon-output efficiency, reinforcing its suitability for efficient solar excitation and edge-emission performance.

To investigate the influence of device length on photon transport, additional Eu^{3+}-doped glass plates (0.50 mol% Eu_2O_3) with lateral sizes of 4 cm and 6 cm (thickness fixed at 0.25 cm) were fabricated. Photographs of these samples under ambient light and UV irradiation are shown in Figure 3.2c. For clarity, the samples with side lengths of 2, 4, and 6 cm are denoted as L = 2 cm, L = 4 cm, and L = 6 cm. The corresponding η_{edge} values—77.49%, 77.44%, and 77.30%—indicate that the guiding efficiency remains unchanged as the device size increases. Consistently, the $\eta_{abs}(\lambda)$ and $\eta_{pl}(\lambda)$ functions measured under identical excitation conditions produced $\eta_{ext}(\lambda)$ values of 6.483%, 6.475%, and 6.442% for L = 2, 4, and 6 cm, confirming that photon confinement and waveguiding behavior are practically independent of the waveguide dimensions.

A complementary method for evaluating photon transport involves photoluminescence measurements performed as a function of in-plane optical path length. In this technique, a tightly focused excitation beam is directed onto the top surface of the glass plate at normal incidence, while the resulting luminescence is collected exclusively from one edge using a fiber-coupled spectrometer, detailly given in Experimental Section. By translating the excitation spot in discrete steps across the surface, the lateral distance L between the illuminated region and the collection edge is systematically varied (Figure 4.3a). Although this measurement is conceptually related to the η_{edge} parameter, it differs in scope: η_{edge} reflects the overall probability of photon survival within the entire three-dimensional volume, whereas the optical-path experiment probes transport specifically along a controlled two-dimensional propagation direction.

The measurement configuration is shown in Figure 4.3b. Each glass specimen was secured within a custom 3D-printed PLA holder that exposed only the front and right faces, thereby minimizing external scattering and ambient-light contamination. A collimated excitation beam (1 × 6000 μm^2) was incident on the front surface, producing a narrow, bright emission band aligned with the excitation axis. The collection fiber, positioned at the right-hand edge, was aligned with the region of highest emission intensity. During data acquisition, the sample holder was translated laterally to increment L, while maintaining constant mechanical contact between the fiber tip and the edge to ensure reproducible optical coupling. Typical edge-emission spectra for the largest device (L = 6 cm) are presented in Figure 4.3c, accompanied by a schematic definition of the optical path. As the excitation spot moved farther from the collection edge, the detected PL intensity decreased gradually, although the spectral profile remained unchanged. The integrated peak intensities exhibited a clear exponential attenuation behavior:

$$I_L = I_0 e^{-\mu(\lambda)\, L} \tag{4.2}$$

Here, I_L denotes the emission intensity recorded at a given optical distance L, while I_0 represents the reference signal measured at a fixed offset of 5 mm. Fitting the experimental data to this exponential decay model yielded an attenuation coefficient of $\beta = 0.054$ mm^{-1}, which captures the combined influence of optical scattering, background (parasitic) absorption, and small but non-negligible reabsorption events during photon propagation.

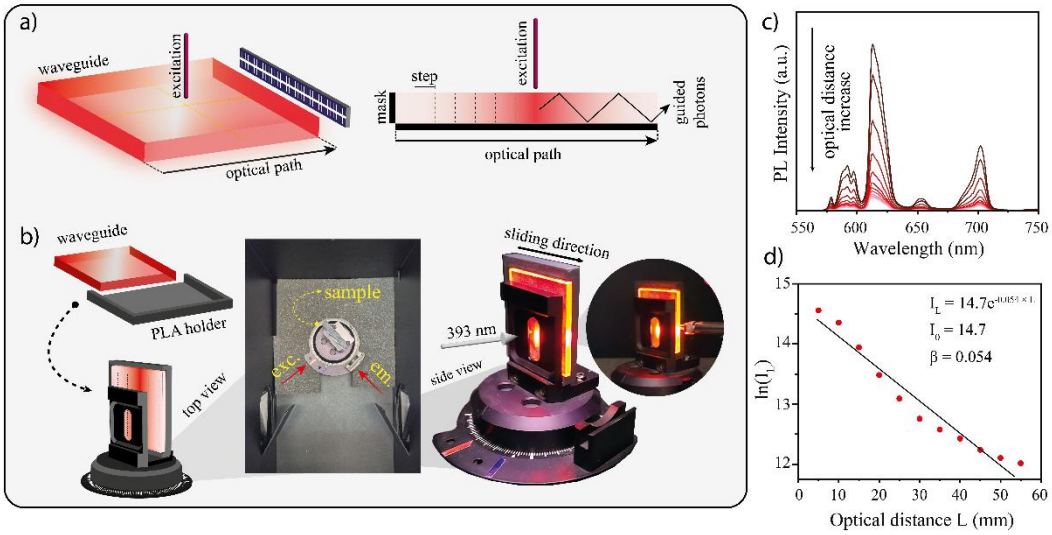


Figure 4.3 (a) Schematic representation of the measurement concept used to evaluate edge-emitted photoluminescence as a function of in-plane optical path length L. (b) Experimental arrangement employed for optical-path–dependent PL measurements, showing the excitation and collection geometry. (c) Representative edge-emission spectra recorded for the Eu^{3+}-doped glass sample with a lateral dimension of 6 cm. (d) Exponential decay fit of the integrated edge-emission intensity I_L as a function of the optical distance L for the 0.50 mol% Eu^{3+} sample.

Although the photoluminescence intensity decreases as photons travel longer distances within the glass, the external photon efficiency $\eta_{ext}(\lambda)$ remains unchanged for all sample sizes. This behavior arises because, under broad-area solar excitation, the entire plate is uniformly illuminated. Photons generated near the edges inherently dominate the measurable output, while those originating farther away contribute proportionally less to the total signal. Consequently, the balance between total absorbed photons and those reaching the edges is preserved, making $\eta_{ext}(\lambda)$ insensitive to propagation length. These results demonstrate that Eu^{3+}-doped glass waveguides maintain stable transport properties across different lateral

dimensions, reinforcing their suitability for large-scale, solar-driven LSC installations.

4.3 Evaluation of Optical, Environmental and Mechanical Performance

In addition to optical efficiency, the glasses were examined for their suitability in architectural applications, where transparency and visual neutrality are essential. The transmittance profile of the 0.50 mol% Eu^{3+} sample is shown in Figure 4.4a: the glass exhibits strong UV absorption below 320 nm while retaining high transparency throughout the visible region above 400 nm. The inset photograph, taken outdoors under natural light, highlights its clear and colorless appearance. This prominent level of transparency results from Eu^{3+} absorption features being confined to the UV, ensuring minimal attenuation of visible wavelengths, and preserving a neutral, aesthetically compatible look.

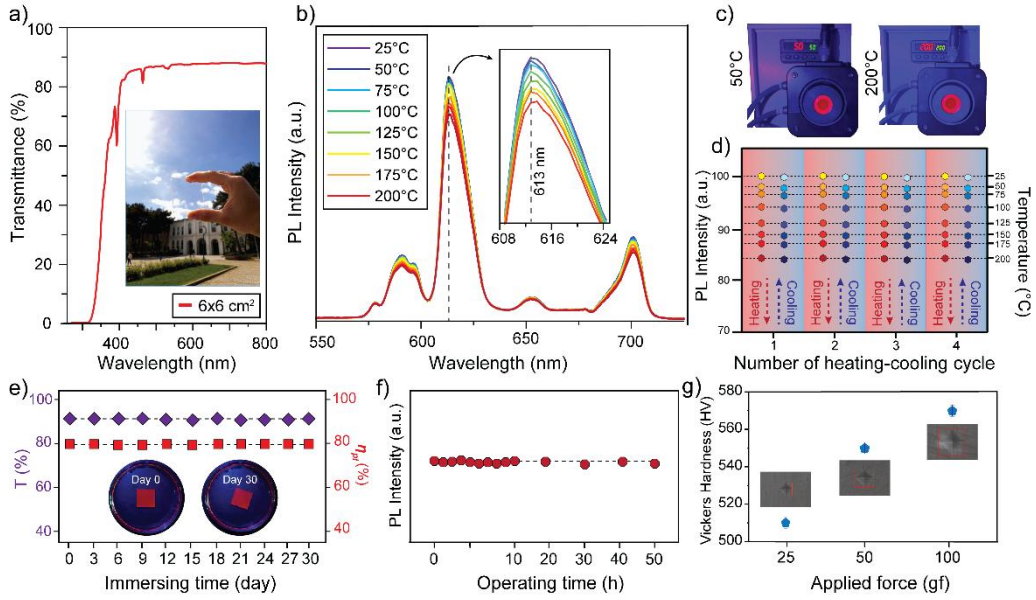


Figure 4.4 (a) Optical transmittance spectrum of the glass containing 0.50 mol% Eu^{3+}, with an inset photograph showing a 6×6 cm^2 sample illuminated by natural sunlight. (b) Temperature-dependent PL emission spectra recorded as the sample was heated from ambient temperature to 200 °C. (c) Corresponding luminescence photographs taken at 50 °C and 200 °C, illustrating thermal effects on emission. (d) Variation in PL intensity tracked over four sequential heating–cooling cycles. (e) Time evolution of optical transmittance and photoluminescence quantum yield

during 30 days of immersion in deionized water. (f) Photoluminescence stability under continuous 393 nm excitation monitored over a period of 50 hours. (g) Vickers microhardness values obtained under different applied loads, with the inset showing representative indentation marks at 100× magnification.

Table 4.1 summarizes the average visible transmittance (AVT), color rendering index (CRI), and CIELAB chromaticity coordinates for both undoped and Eu^{3+}-doped glasses. All samples exhibit excellent optical clarity, with AVT values at or above 87.2%, and maintain exceptional color fidelity, reflected in CRI values of 97 or higher. Among the compositions, the 0.50 mol% Eu^{3+} glass achieves the highest visible transmittance (89.42%) and a CRI of 98, accompanied by CIELAB coordinates of L* = 95.7, a* = 2.5, and b* = 7.2 indicating high luminance and only minimal deviation from a neutral color point. These measurements demonstrate that introducing Eu^{3+} ions enhances photoluminescence while preserving the inherent visual neutrality of the host glass. Consistent with its superior photonic performance, the 0.50 mol% composition also delivers the most favorable visual attributes, representing an optimal compromise between functional efficiency and architectural suitability.

Table 4.1 Average visible transmittance (AVT), color rendering index (CRI), and CIELAB chromaticity values for the undoped glass and the Eu^{3+}-doped samples containing 0.25%, 0.50%, and 1.00% Eu_2O_3.

Eu_2O_3 concentration (mol%)	AVT (%)	CRI	CIELAB (L*, a*, b*)		
			*L**	*a**	*b**
0.00%	87.69	97	95.0	1.5	10.4
0.25%	87.86	97	95.1	1.5	10.8
0.50%	89.42	98	95.7	2.5	7.2
1.00%	87.23	97	94.8	2.5	9.0

Preserving high transparency and a visually neutral appearance is essential for incorporating LSCs into architectural settings, yet these attributes alone are insufficient without long-term environmental resilience. For this reason, the durability of the optimized 0.50 mol% Eu^{3+}-doped glass was examined through a series of thermal, chemical, photochemical, and mechanical tests to determine its suitability for outdoor deployment.

Temperature-dependent PL experiments conducted from 25 °C up to 200 °C (Figure 4.4b) showed a gradual reduction in overall emission intensity, while the characteristic 613 nm transition remained fixed in both position and spectral shape,

signifying strong resistance to thermally driven structural changes. Photographs captured at intermediate (50 °C) and elevated (200 °C) temperatures (Figure 4.4c) exhibited no detectable shift in color or brightness. Repeated heating–cooling cycles (Figure 3.4d) further demonstrated that the luminescence response is highly reversible, with negligible permanent loss, highlighting the thermal robustness of the glass matrix, an essential requirement for LSCs operating in outdoor environments.

Chemical stability was evaluated by submerging samples in deionized water for a period of 30 days. Throughout this interval, periodic measurements of transmittance and η_{pl} (Figure 4.4e) showed no measurable changes. No haziness, surface degradation, or spectral shifts were observed, indicating strong resistance to aqueous corrosion.

Photochemical stability was assessed under continuous 393 nm irradiation over 50 hours (Figure 4.4f). Apart from minor short-term fluctuations, the PL output remained constant, demonstrating that long-term UV exposure does not induce photobleaching or generate additional non-radiative centers within the Eu^{3+}-doped network.

Mechanical performance was examined via Vickers indentation (Figure 4.4g). The measured hardness values reaching 5.6 GPa under a 100-gf load are consistent with the performance of high-strength borosilicate glasses, confirming that the material can withstand stresses relevant to overseeing and processing.

Together, these evaluations provide compelling evidence that the Eu^{3+}-doped glass exhibits excellent resistance to thermal cycling, water exposure, sustained UV irradiation, and mechanical loading. This comprehensive resilience positions the material as a promising luminescent component for LSCs intended for BIPV applications. Nonetheless, the current configuration serves primarily as a proof-of-concept; further development of fully integrated and industrially qualified glass-based LSC modules remains an important future direction.

4.4 LSC Device Study

Figure 4.5a presents the arrangement used to characterize the photovoltaic response of the assembled LSC devices under standard AM1.5G illumination. In this setup,

the Eu^{3+}-doped glass plates were optically coupled to laser-cut monofacial PERC silicon strips (8.0 × 1.0 cm^2). The figure includes both a schematic depiction and a photograph of the actual device. Each plate was positioned inside a black PLA holder that masked the bottom surface and three side faces to eliminate stray light contributions. No refractive-index-matching material was applied; instead, the emitting edge was brought directly into contact with the active region of the silicon cell, with the effective coupling area defined by the holder geometry. To prevent the PV element from receiving direct ambient illumination, the cell was placed approximately 1 mm below the outer edge of the holder, and any non-active or uncovered sections were covered with an opaque, light-absorbing layer.

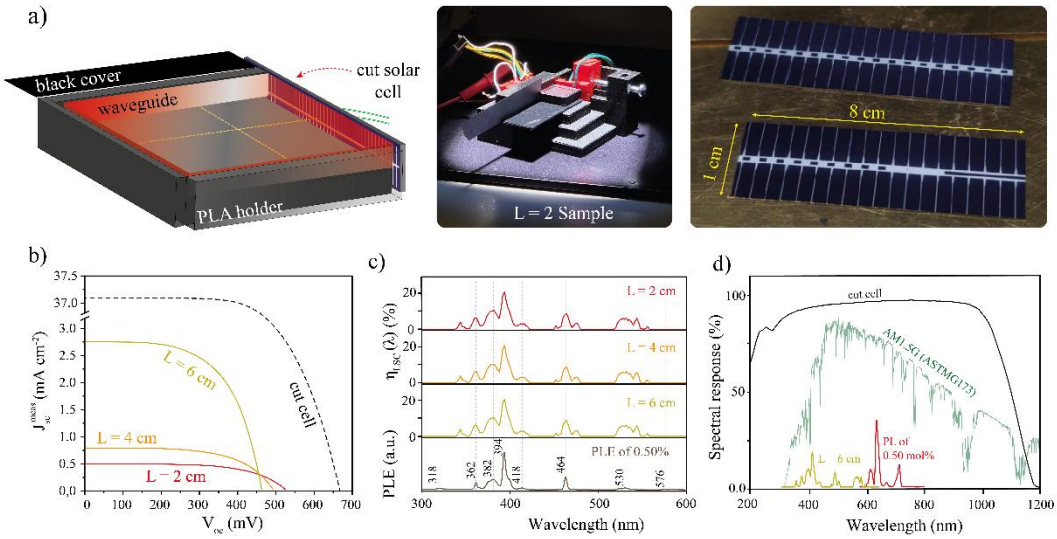


Figure 4.5 (a) Schematic representation and corresponding photograph of the customized measurement platform used to couple the Eu^{3+}-doped glass waveguide to the laser-cut silicon cell, illustrated for the device with L = 2 cm under AM1.5G illumination. (b) Current–voltage curves of LSCs fabricated with waveguide lengths of 2, 4, and 6 cm, shown together with the reference cut-cell for comparison. (c) External quantum efficiency of the LSC devices as a function of waveguide length. (d) Wavelength-dependent $EQE_{lsc}(\lambda)$ for the 6 cm device, plotted alongside the PL emission profile, the EQE of the standalone cut-cell, and the AM1.5G solar spectrum. $EQE_{lsc}(\lambda)$ and the reference EQE are given in percentage units, whereas the PL and AM1.5G spectra are displayed in arbitrary units.

The J–V behavior of the reference silicon cut-cell under standard AM1.5G irradiation (100 mW cm^{-2}) is presented in Figure 4.5b. The measured short-circuit

current density (J_{sc}^{meas}) was evaluated using the illuminated top surface as the effective active area, consistent with the photon-coupling geometry in the LSC configuration. As the device area increased, J_{sc}^{meas} decreased from 0.687 mA cm^{-2} to 0.124 mA cm^{-2}. This trend aligns with expectations based on the geometric gain factor: as G increases with the lateral dimensions of the waveguide, the absolute photon flux delivered to the PV cell grows, but the normalized current density correspondingly decreases.

Table 2.2 compiles the photovoltaic characteristics (V_{oc}, I_{sc}, FF, and J_{sc}) for LSC devices with L = 2, 4, and 6 cm, including both calculated values and experimentally measured parameters normalized to four edges. With increasing waveguide length, V_{oc} increased from 463 mV to 525 mV and I_{sc} rose from 2.749 mA to 4.472 mA, indicating enhanced overall photon harvesting in larger devices. The fill factor remained constant at ~67%, demonstrating stable charge-collection behavior across all configurations. This stability is expected, as the emission wavelength remains independent, thus illumination condition of PVs is unchanged with the LSC dimensions. For direct comparison among devices, the reported 4×J_{sc} values denote the equivalent current density expected for a configuration in which all four edges are coupled to PV cells.

Table 4.2 Photovoltaic parameters of LSC devices with waveguide lengths of L = 2, 4, and 6 cm, presenting both calculated values and experimentally measured parameters normalized to four-edge coupling.

L (cm)	**V_{oc} (mV)**	**I_{sc} (mA)**	**J_{sc}^{meas} (mA/cm^2)**	**J_{sc}^{calc} (mA/cm^2)**	**$4 \times J_{sc}^{meas}$ (mA/cm^2)**	**$4 \times J_{sc}^{calc}$ (mA/cm^2)**	**FF (%)**
2	463	2.749	0.687	0.598	2.749	2.392	66.85
4	493	3.165	0.198	0.299	0.792	1.196	67.14
6	525	4.472	0.124	0.199	0.496	0.796	67.11

The wavelength-dependent external quantum efficiency of the LSC, $EQE_{LSC}(\lambda)$, was derived from the external photon efficiency $\eta_{ext}(\lambda)$ according to the mathematical model reported in the relevant reference. [173] The average spectral response of the silicon cell within the Eu^{3+} emission range, EQE_{pv}^{*}, was approximately 95%. Figure 4.5c compares the $EQE_{lsc}(\lambda)$ profiles of the L = 2, 4, and 6 cm devices with the excitation spectrum of the 0.50 mol% Eu_2O_3-doped glass. The curves exhibit identical spectral shapes, with only minor deviations around 318 nm and 576 nm. These differences possibly arise from strong host absorption in the

deep-UV region, where $\eta_{pl}(\lambda) = 0$, and the intrinsically weak transition near 576 nm.

Short-circuit current densities (J_{SC}^{meas}) were subsequently calculated using equation 23, [173] yielding 0.598, 0.299, and 0.199 mA cm^{-2} for waveguide lengths of 2, 4, and 6 cm, respectively. The calculated values agree well with the measurements for smaller devices and remain consistent as dimensions increase. Small discrepancies are attributed to optical losses at the glass–cell interface, caused by microscopic air gaps introduced during assembly. These losses could be significantly reduced by applying a refractive-index–matching layer in future device configurations.

Figure 4.5d presents $EQE_{lsc}(\lambda)$ for the 6 cm device alongside the PL spectrum of Eu^{3+}-doped glass, the EQE of the reference silicon cell, and the AM1.5G solar spectrum. The strong alignment between the LSC emission band and the Si-cell EQE confirms excellent spectral compatibility under solar illumination.

Table 4.3 summarizes the performance of the 0.50 mol% Eu^{3+}-doped LSCs developed in this study and compares them with previously reported Eu^{3+}-based systems. In addition to reporting the PCE values for three device sizes (L = 2, 4, and 6 cm), the table compiles key literature data, including LSC type (planar or cylindrical), luminescent species, host matrix, processing method (film, fiber, or bulk), device size, and measurement conditions. [180] As early discussed optical efficiency is measured/calculated using different methods, therefore, this metric is not included in the table. To ensure clarity and consistency in performance comparison, PCE is selected as the primary metric, as it provides a more robust and standardized measure of LSC performance. [180] The resulting LSC prototypes exhibit excellent optical transparency and color neutrality, yielding PCE values of 0.213%, 0.066%, and 0.041% for device lengths of 2, 4, and 6 cm, respectively, coupled to a single PV cell mounted along one edge. For a fair comparison with fully edge-coupled configurations, these values can be scaled by a factor of four to represent a device in which all four edges are interfaced with PV cells. Under this assumption, the corresponding four-edge–equivalent PCEs (4×PCEs) are 0.852%, 0.264%, and 0.164% for the 2, 4, and 6 cm devices, respectively comparable to or surpassing the performance of many previously reported Eu^{3+}-based systems.

The observed decrease in PCE can be primarily explained by the geometric gain factor (G), which is inversely proportional to the device length ($G \propto 1/L$). This geometric scaling alone accounts for approximately a threefold efficiency reduction when the device dimension increases from 2 cm to 6 cm. However, the experimental results reveal a slightly larger decrease (~4.8-fold), suggesting the presence of additional loss mechanisms. The slightly larger-than-expected reduction is attributed to minor interfacial losses at the glass–PV interface, likely caused by small air gaps in the proof-of-concept assembly. These losses are not intrinsic to the Eu^{3+}-doped glass and could be minimized using standard index-matching techniques in future scalable devices.

Table 4.3 Overview of Eu^{3+}-based LSC studies, classified according to LSC architecture, luminophore properties, host material, fabrication route, device dimensions, η_{pl}, optical efficiency (OE), and power conversion efficiency (PCE). The table highlights performance variations, compliance with the LSC consensus reporting guidelines, and peak or representative PCE values, with complete bibliographic details given in the reference section.

Luminophore	Host material	Processing Method	Device size (cm)	η_{pl} (%)	OE (%)	PCE (%)	Deviations	Year	Ref.
$Eu(tta)_3(Phen)$	PVB	Film	7.8×7.8×0.3	44	-	0.0499	(iii)	2011	[22]
$Eu(tta)_3(TPPO)_2$	PMMA	Film	10×10×0.3	73	-	0.28	(iii)	2011	[133]
Eu^{3+}@diureido-bipyridine	Bridged Silsesquioxane (BS)	Film	~2.5×2.5×0.8	34	1.7	-	-	2011	[114]
Eu^{3+}@diureido-bipyridine	Modified Organosilane	Film	2.5×2.5×0.08	8	1.2	-	-	2012	[142]
$Eu(tta)_3(Phen)$	Tri-ureasil 5000	Film	-	63	-	-	-	2013	[143]
$Eu(btfa)_3(MeOH)_2]_2bpta_2$	Tri-ureasil 5000	Film	2.5×2.5×1.0	27	3.2	0.07	(ii)	2014	[144]
$Eu(TTA)_3phen$	Parylene	Film	5×5×0.5	-	2.47	0.19	*	2015	[145]
Eu^{3+} @diureido-bipyridine	BS	Film	2.5×2.5×0.14	23	0.43	0.3	(iii)	2015	[181]
Eu^{3+}:ionossilica	PMMA	Film	7.5×2.0×0.1	31	0.34	0.0019	(ii)	2019	[182]
$Eu(2mCND)_3$	Di-ureasil	Film	5×5×0.4	69	0.51	0.138	(i, ii)	2022	[146]
Lu Red (commercial)	Acrylic resin	Film	5×5×0.3	20-36	-	0.70	*	2022	[140]
Eu^{3+} tetrakis(β-diketonate)	PMMA	Film	3×3×0.4	63	5.40	0.096	(i)	2022	[134]
$[Eu_2LF_4](NEt_4)_2$	PMMA	Bulk	5×5×0.27	50	-	0.124	*	2024	[21]
Eu^{3+}	Glass	Bulk	2×2×0.25 4×4×0.25 6×6×0.25	78	-	0.213 × 4 0.066 × 4 0.041× 4	*	2025	This work

*Studies classified as "in agreement" with the consensus statement adhere to standardized LSC measurement protocols. [172] In contrast, deviations include one or more of the following: (i) lack of edge covering, (ii) use of a reflective background/edge covering, and (iii) insufficient experimental detail. Studies that do not report any PCE values are marked with (–), as the comparison is based solely on reported PCE data.

Literature surveys indicate that the majority of Eu^{3+}-based LSCs rely on polymer hosts such as PMMA, PVB, or resin matrices in either thin-film or bulk form. Although these materials allow straightforward processing and provide high initial transparency, they suffer from limited thermal, photochemical, and mechanical stability, which restricts their long-term outdoor usability. Even when Eu^{3+} complexes or co-dopants are incorporated to enhance performance, reported PCE values often remain below 0.01%, due to insufficient photon confinement and the inherent incompatibility of polymer-based architectures with scalable, fully integrated device designs.

Alongside the optical efficiencies, direct comparison of PCE values across published studies is also complicated by inconsistencies in experimental procedures. As summarized in Table 4.3, many reports do not follow standardized testing conditions (AM1.5G, 100 mW cm^{-2}) or omit essential details such as spectral mismatch corrections, optical-coupling geometry, or edge-masking conditions. In several cases, efficiencies are derived from non-standard or extrapolated measurements, introducing substantial uncertainty. These methodological variations can easily lead to inflated or underestimated performance values, emphasizing the need for unified and transparent characterization protocols within the LSC community. In contrast, the present work adheres to established measurement practices, enabling fair, reproducible, and directly comparable evaluation of device-level efficiency.

Despite the variability in literature, a small number of studies present robust methodologies and thus provide reliable reference points. Bertozzi et al., for example, demonstrated a film-type LSC employing a commercial red dye in an acrylic resin and achieved a peak PCE of 0.70% while maintaining high optical clarity and architectural flexibility. [145] Motta et al. reported supramolecular Eu^{3+} cages as hybrid emitters, reaching a PCE of 0.124% and illustrating the promise of molecular-level design strategies for improved optical performance. [21] Together, these examples highlight meaningful progress toward optimizing Eu^{3+}-based LSCs through advances in luminophore chemistry and device engineering.

However, polymer- and hybrid-based Eu^{3+} LSCs continue to face major limitations, particularly regarding environmental robustness and scalability. In this regard, the Eu^{3+}-doped glass LSCs developed here provide several critical advantages: high

visible transparency, near-colorless appearance, intrinsic UV-blocking behavior, and exceptional chemical, thermal, and mechanical durability. These attributes directly address the durability and manufacturability issues that constrain polymeric systems, positioning glass as a compelling platform for large-area, regulation-compliant BIPV integration.

5
PQD GNC-BASED LSCs

The central aim of this study is to quantify the optical scaling limits of $CsPbBr_3$ PQD-glass nanocomposites and demonstrate that, despite reabsorption effects, these systems achieve a stable performance regime suitable for large-area BIPV applications.

5.1 Thermal, Structural, Optical and Photoluminescence Properties

The thermal characteristics of the as-cast glass were examined to determine suitable annealing and heat-treatment conditions for PQD-GNC fabrication. As shown in Figure 5.1a, the STA curve exhibits characteristic thermal events, with T_g, T_c, and T_p appearing at 508 °C, 665 °C, and 695 °C, respectively. Based on these data, the annealing temperature was fixed at 450 °C, slightly below T_g to prevent spontaneous crystallization during relaxation. Subsequent heat treatments were performed at 510–570 °C in 10 °C increments for 4h, promoting structural reorganization and controlled in-situ crystallization of $CsPbBr_3$ PQDs within the glass host. The STA profiles also verify the high thermal stability of the synthesized glasses, ensuring structural integrity suitable for outdoor LSC applications.

Figure 5.1b displays the XRD patterns of the as-cast and heat-treated PQD-GNCs processed between 510 °C and 570 °C. The as-cast glass shows a broad diffuse halo without sharp reflections, confirming its amorphous nature. Samples treated at 510 °C and 520 °C retain this amorphous character, as any nanocrystals formed remain below the XRD detection threshold indicating either incomplete PQD formation or exceedingly small particle sizes dispersed within the matrix. In contrast, samples treated between 530 °C and 570 °C exhibit distinct diffraction peaks at

approximately 2θ = 15.17°, 21.52°, 30.39°, 37.56°, and 43.62°, corresponding to the (100), (110), (200), (211), and (220) planes of cubic $CsPbBr_3$ (PDF No. 54–0752). The absence of secondary phases confirms phase-pure PQD crystallization, while the gradual narrowing and intensification of peaks with increasing temperature suggest crystal growth and improved size uniformity.

TEM characterization further validates PQD formation and size distribution within the glass matrix (Figures 5.1c–k). The bright-field TEM image (Figure 5.1c) reveals a uniform nanoparticle dispersion across a wide region, while the HAADF-STEM image (Figure 5.1d) highlights enhanced Z-contrast consistent with the presence of Cs- and Pb-containing domains. Particle size analysis (Figure 5.1e), based on over 300 individual PQDs, shows diameters ranging from 4 to 18 nm with an average of 9.35 ± 2.13 nm. High-resolution TEM images (Figures 5.1f, i) confirm the presence of crystalline PQDs embedded in the amorphous matrix. A magnified HRTEM image (Figure 5.1g) of a single PQD (indicated in Figure 4.3f) and its corresponding FFT (Figure 5.1h) identify cubic $CsPbBr_3$ (Pm-3m, a = 0.587 nm) along the [001] zone axis. Similarly, another nanoparticle (highlighted in Figure 1i) and its FFT pattern (Figure 5.1k) confirm the same cubic phase viewed along the [011] zone axis.

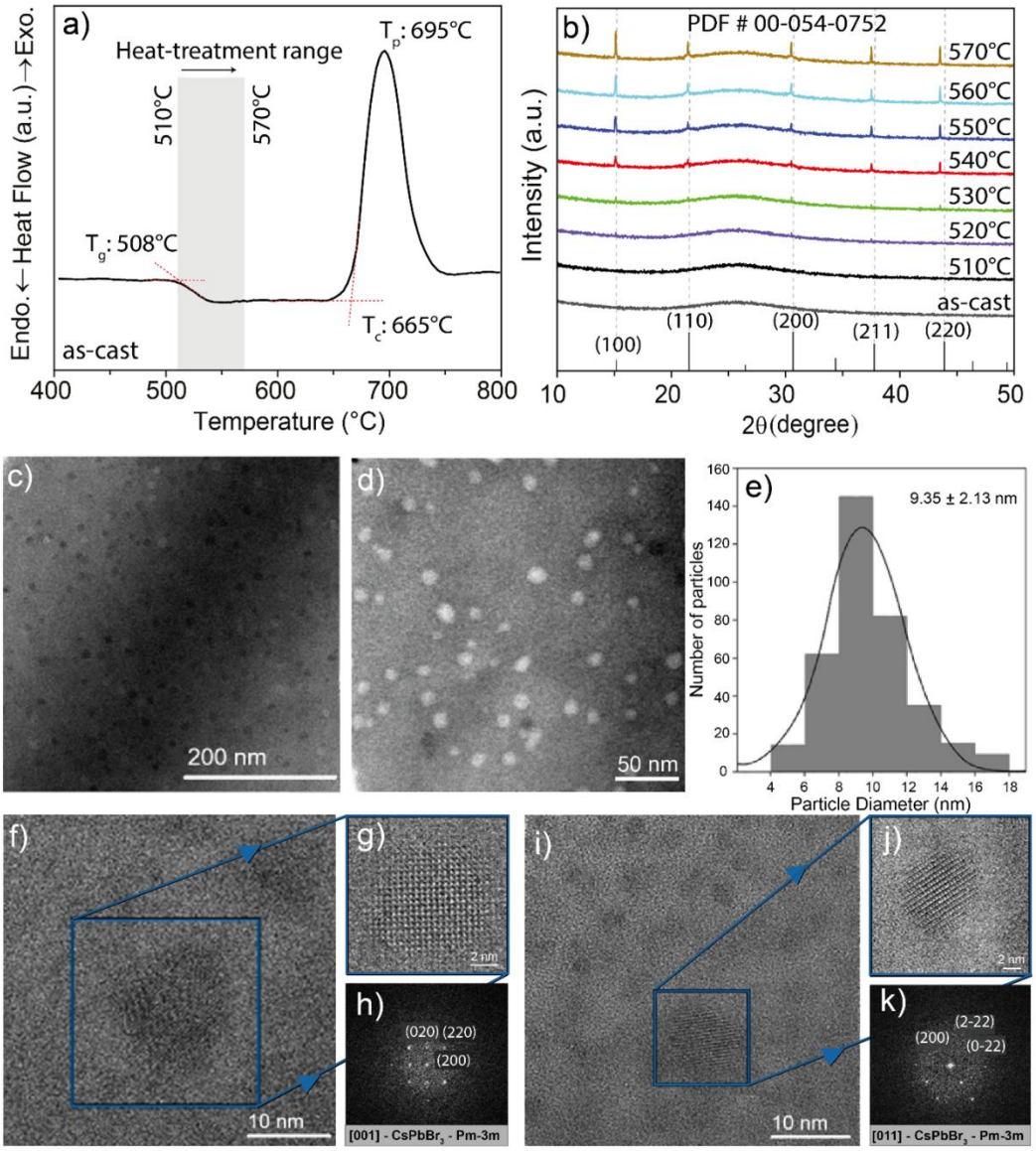


Figure 5.1 (a) STA curve of the as-cast glass. (b) XRD patterns of the as-cast sample and PQD GNCs heat-treated between 510–570 °C (10 °C increments, 4h). (c) Bright-field TEM and (d) HAADF-STEM images of the 540 °C–4h GNC sample, showing a uniform distribution of $CsPbBr_3$ PQDs within the glass matrix. (e) Particle size histogram obtained from measurements of more than 300 PQDs. (f, i) HRTEM images confirming $CsPbBr_3$ nanocrystals embedded in the glass. (g, j) Magnified HRTEM views of the PQDs marked in (f) and (i). (h, k) Corresponding FFT power spectra of the nanoparticles shown in (g) and (j), verifying the cubic $CsPbBr_3$ phase.

Figure 5.2a shows photographs of the as-cast and heat-treated samples (510–570 °C, 4h) under daylight and UV illumination. The as-cast glass is colorless and highly transparent, confirming that no spontaneous crystallization occurred during melt-quenching. Upon heat treatment, the samples gradually transition from pale to deeper yellow, reflecting the growth of $CsPbBr_3$ PQDs. The very slight coloration at 510 °C and 520 °C suggests incomplete or nanoscale crystallization, consistent with the XRD patterns shown in Figure 5.2b.

This visual evolution is directly mirrored in the optical absorption spectra given in Figure 5.2b. The as-cast sample displays an absorption edge at 333 nm, which progressively redshifts with increasing heat-treatment temperature (510–570 °C; see Table 5.1). This shift is attributed to the enlargement of PQDs within the glass matrix. A distinct first excitonic peak is visible for the 510 °C and 520 °C samples but disappears at higher temperatures, either due to increased PQD concentration causing spectral saturation or because the intrinsic absorption edge of the host glass obscures these features.

Table 5.1 Summary of the as-cast and heat-treated PQD GNCs at various temperatures, including their absorption edge, direct optical bandgap energies, particle radii determined by the EMA method, PL center peak wavelengths, FWHM, and Stokes shift values.

Sample	Absorption edge (nm)	E_g (eV)	Particle radius (nm)	PL peak wavelength (nm)	FWHM (nm)	Stokes Shift (meV)
As-cast	333	3.83	-	-	-	-
510°C	473	2.54	3.67	494	27	111.44
520°C	491	2.45	4.36	511	24	98.84
530°C	506	2.41	4.85	519	24	61.38
540°C	513	2.38	5.37	529	20	73.11
550°C	516	2.37	5.59	531	24	67.88
560°C	517	2.36	5.84	532	21	67.63
570°C	520	2.34	6.51	534	16	62.51

Figure 5.2c presents the derivative absorption spectrum fitting (DASF) plots, obtained from $[d\ln(A(\lambda)^{-1}/d(\lambda)^{-1}]$ vs. λ^{-1}, for as cast and heat-treated samples. All curves show a characteristic discontinuity at λ_g^{-1}, defining the optical bandgap wavelength (λ_g), from which the bandgap energy (E_g = 1239.83/λ_g) is calculated. The as-cast sample exhibits an E_g of 3.83 eV, while heat-treated samples show a systematic decrease from 2.54 to 2.34 eV as temperature increases from 510 °C to 570 °C (Table 5.1). This bandgap narrowing reflects the progressive growth of $CsPbBr_3$ PQDs. Using these bandgap values, PQD crystallite radii were estimated

via the effective mass approximation (EMA, equation 3.1), yielding sizes from 3.67 nm to 6.51 nm over the same temperature range. Notably, the crystallite size obtained for the 540 °C sample closely matches the TEM-derived size distribution, validating the EMA estimations.

Figure 5.2d shows the normalized PL emission spectra (under 450 nm excitation) for samples treated between 510 °C and 570 °C. The maximum emission red shifts steadily from 494 nm to 534 nm with increasing temperature, consistent with PQD growth. The general emission profile remains unchanged, while the FWHM decreases from 27 nm to 16 nm, indicating improved size uniformity (Table 5.1). The Stokes shift varies from 111 meV to 63 meV across this series. A decrease up to 540 °C suggests reduced structural disorder and narrower PQD size distribution, alongside the increase in absorption cross-section, while the modest rise at 540 °C (to 73 meV) suggests enhanced radiative recombination. At higher temperatures, the Stokes shift decreases again, attributed to further PQD coarsening and changes in electronic confinement, negatively affecting the quality of radiative recombination.

Figure 5.2e summarizes the PLQY values of heat-treated samples from 510 °C to 570 °C. To minimize reabsorption effects, PLQY measurements were performed on small 1×1×1 mm^3 pieces. The measured PLQY values are 23%, 58%, 78%, 97%, 73%, 39%, and 35% from 510 °C to 570 °C, respectively. Figure 5.2f shows the PLQY spectrum of the 540 °C sample, which exhibits the highest efficiency of 97%, exceeding previously reported values for bromide-based PQD-GNCs, before declining at higher temperatures.

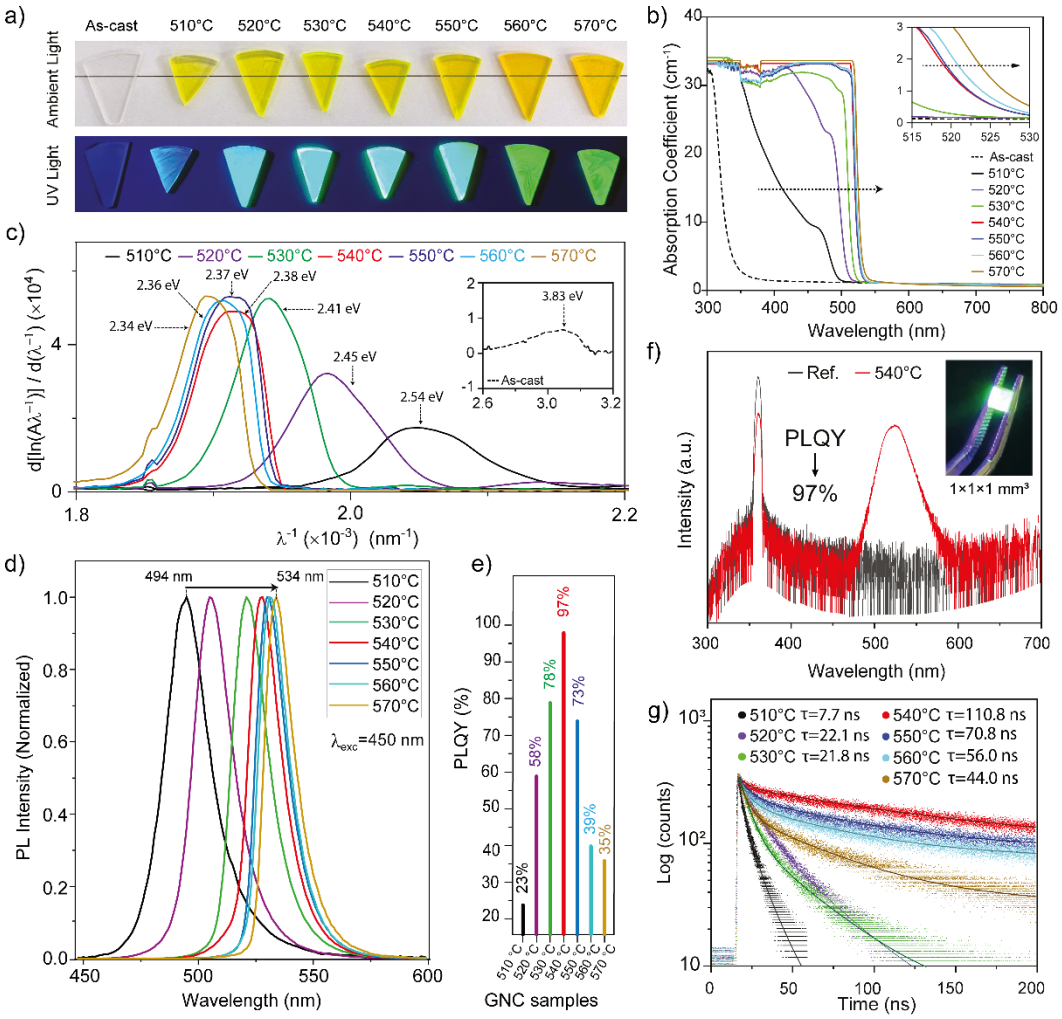


Figure 5.2 (a) Photographs of the as-cast glass and samples heat-treated between 510–570 °C under daylight and UV illumination. (b) Optical absorption spectra and (c) corresponding DASF plots of the same series. (d) PL emission spectra of the heat-treated samples under 450 nm excitation. (e) PLQY values measured for ~1×1×1 mm^3 pieces under 360 nm excitation. (f) PLQY spectrum of the 540 °C sample, with an inset showing the measured piece. (g) Time-resolved PL decay curves of the heat-treated samples under 450 nm pulsed excitation.

Figure 5.2g shows the time-resolved PL decay curves for samples heat-treated between 510 °C and 570 °C, recorded under 450 nm pulsed excitation while monitoring each sample's dominant emission peak. The corresponding lifetime parameters, non-radiative (τ_1), radiative (τ_2), and average (τ_{ave}), are summarized in Table 5.2. The short components τ_1, ranging from 3–10 ns (average ~6 ns), indicate consistently low defect densities throughout the series. In contrast, the radiative lifetimes τ_2 follow a clear temperature-dependent trend, increasing from

9.9 to 112.7 ns up to 540 °C before decreasing to 50.2 ns at 570 °C. A similar pattern is observed for τ_{ave}, which rises from 7.7 to 110.8 ns and then declines to 44.0 ns across the same temperature range.

Table 5.2 Photoluminescence lifetime parameters of PQD GNCs heat-treated at temperatures between 510°C and 570°C.

Sample	τ_1 (non-radiative) (ns)	τ_2 (radiative) (ns)	τ_{ave} (average) (ns)	χ^2
510 °C	3.0	9.9	7.7	1.056
520 °C	10.4	30.1	22.1	1.039
530 °C	6.1	31.4	21.8	1.044
540 °C	5.8	112.7	110.8	1.022
550 °C	7.6	75.9	70.8	1.035
560 °C	6.3	61.7	56.0	1.034
570 °C	5.4	50.2	44.0	1.065

The pronounced increase in τ_2 at 540 °C reflects improved excitonic stability and more efficient radiative recombination, consistent with the peak PLQY, reduced FWHM, and favorable Stokes shift for this heat-treatment condition. The subsequent drop in τ_2 at higher temperatures signals diminished radiative efficiency, in agreement with the PLQY decrease. Based on these results, 540 °C (4h) is identified as the optimal heat-treatment condition, and GNC waveguides with lateral dimensions ranging from 1×1 cm^2 to 5×5 cm^2 were fabricated using this optimized protocol.

5.2 Evaluation of Optical, Environmental, and Mechanical Performance

To evaluate the practical viability of the GNC waveguides, their optical transmittance, thermal stability, chemical durability, photostability, and mechanical hardness were examined. Figure 5.3a shows the transmittance spectrum of the largest device (5×5 cm^2), which maintains a high transmittance of 89.4%. The inset photographs highlight its uniform structure and excellent optical clarity. Despite the slight yellow tint visible under ambient light, the high transparency confirms its suitability for functional applications.

Thermal stability was assessed through temperature-dependent PL measurements on a 1×1 cm^2 waveguide placed in a heated spectrofluorometer accessory (Figure 5.3b). Across the 25–200 °C range, the samples retain most of their emission

intensity under typical operational conditions (25–75 °C), and although PL decreases at higher temperatures, it remains clearly detectable even at 200 °C. Repeated heating–cooling cycles (five cycles, 25–200 °C) show nearly identical and fully reversible emission behavior, demonstrating the strong thermal robustness of the GNC waveguides.

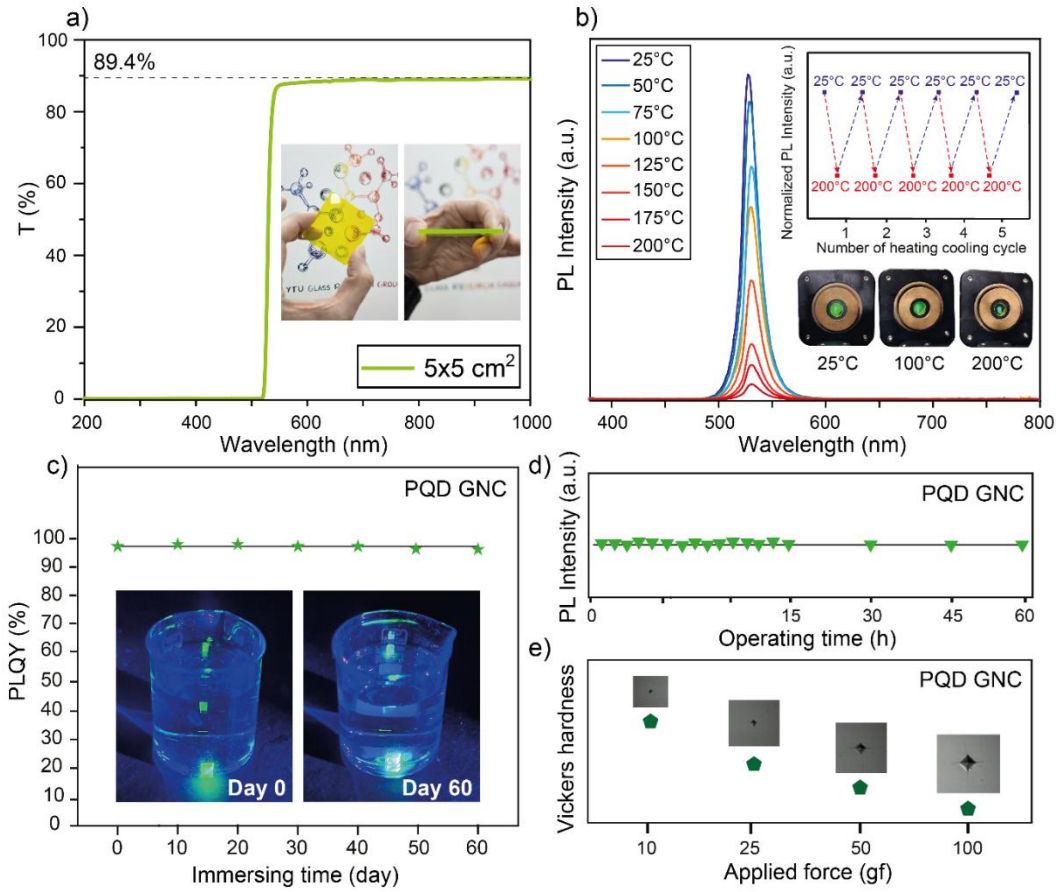


Figure 5.3 (a) Transmittance spectrum of the 5×5 cm^2 GNC waveguide, with inset images highlighting its uniform structure and optical clarity. (b) Temperature-dependent PL emission spectra; the inset shows heating–cooling cycles between 25–200 °C and corresponding luminescence images. (c) PLQY values of a 1×1×1 mm^3 reference sample measured periodically over 60 days of water immersion. d) Photostability of the GNC waveguide under continuous excitation. (e) Vickers hardness measurements under various loads, with insets showing indentations at 100× magnification. All stability characterizations were performed under 360 nm excitation.

Chemical durability was evaluated by immersing a 1×1×1 mm^3 PLQY reference cube in water for 60 days (Figure 5.3c). PLQY measurements recorded every 10

days show no noticeable degradation, confirming that the glass matrix effectively protects the embedded PQDs from moisture-induced deterioration.

Photostability was evaluated using a 5×5 cm^2 waveguide under continuous 360 nm excitation (Figure 5.3d). The emission intensity remains stable over the test duration, indicating excellent resistance to long-term optical stress.

Finally, Vickers hardness tests performed under different loads (Figure 5.3e) reveal hardness values decreasing with increasing applied force, reaching 5.5 GPa at 1000 gf. These values reflect the strong mechanical integrity of the borosilicate glass matrix and support its reliability for real-world use.

5.3 Photonic Collection, Conversion, and Waveguiding Properties

Figure 5.4a shows photographs of GNC waveguides with surface areas ranging from 1×1 cm^2 to 5×5 cm^2 and a uniform thickness of 0.25 mm, corresponding to G-factors between 1 and 5. Images were taken under both daylight and UV illumination. Under ambient lighting, dashed outlines and G-factor annotations highlight the uniform structure and transparency of the waveguides. Under UV excitation, samples placed in PLA holders emit bright green light from the exposed top and right edges.

Figure 5.4b displays PL spectra collected from the total, surface, and edge emissions of GNC-LSC waveguides using diffuse 360 nm illumination inside an integrating sphere. Selective masking was used to isolate surface and edge contributions (schematics shown in the inset). In all cases, emission intensity increases with waveguide area due to a larger luminescent volume. Diffuse excitation ensures that all surfaces contribute to the detected signal. Photons emitted near the surface exhibit minimal reabsorption and form a short-wavelength peak, while reabsorbed photons generate a second, red shifted peak. Thus, surface PL spectra show two peaks, whereas edge emission that is dominated by multiple reabsorption/re-emission events shows a single, red shifted peak that shifts further with increasing waveguide size.

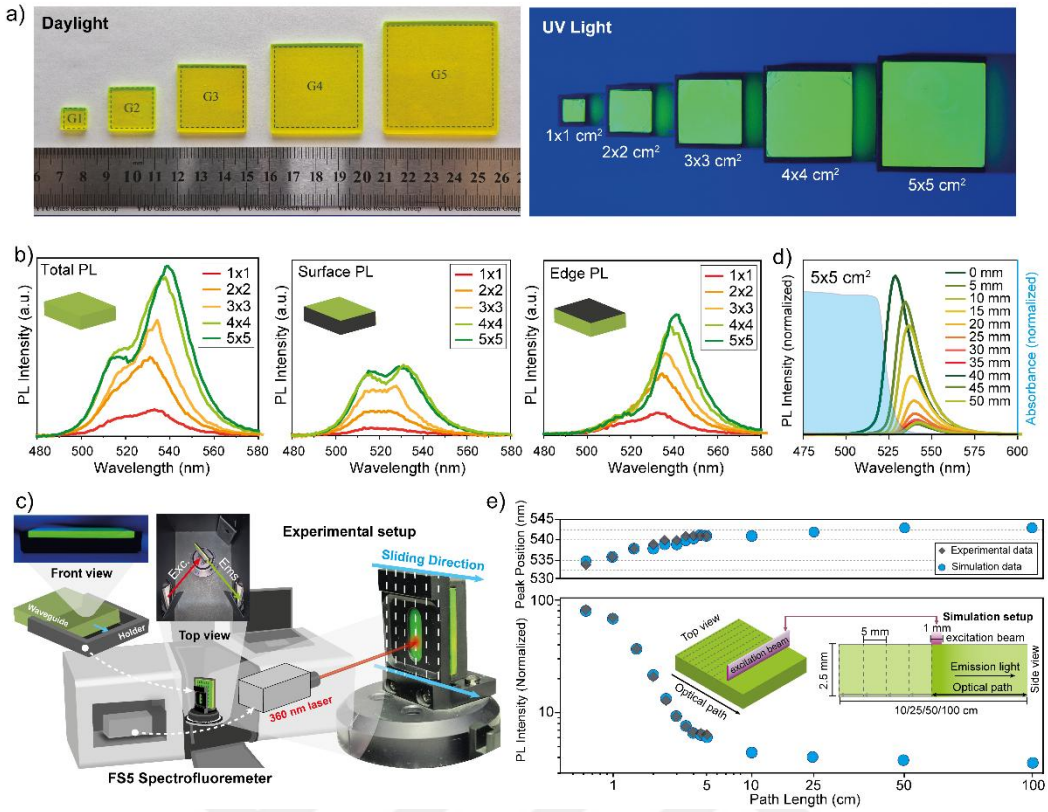


Figure 5.4 (a) Digital images of GNC waveguides (1×1 cm^2 to 5×5 cm^2) under daylight and under UV illumination in PLA holders, in which three edges and the back surface act as blackbody absorbers. (b) PL spectra of total, surface, and edge emissions measured under diffuse 360 nm excitation inside an integrating sphere; inset schematics indicate emitting surfaces, with black regions denoting masked areas. (c) Schematic of the experimental setup showing the definition of optical path length and the measurement procedure. (d) PL spectra of the 5×5 cm^2 waveguide collected at varying optical path lengths. (e) PL peak position and intensity as a function of optical path length, combining experimental data up to 5 cm with Monte Carlo simulations extending from 10 to 100 cm; the inset illustrates the simulation approach.

The optical performance of waveguides was quantified through the edge emission efficiency (η_{edge}), internal photon efficiency (η_{int}), and external photon efficiency (η_{ext}). Numerical values are summarized in Table 5.3. As the device area increases from 1×1 cm^2 to 5×5 cm^2, η_{edge} decreases from 65.2% to 45.9%, with the steepest drop occurring up to 3×3 cm^2 before stabilizing. η_{int}, calculated assuming an intrinsic PLQY of 97% (from the 1×1×1 mm^3 reference sample), shows a similar trend, decreasing from 63.3% to 44.5%. These results indicate that optical losses

are primarily reabsorption and escape-cone losses that are most significant at smaller sizes; beyond ~3×3 cm^2, the flux reaching the edges remains constant, though with reduced photon energy due to cumulative re-emission.

Table 5.3 Edge emission efficiency (η_{edge}), internal photon efficiency (η_{int}), and external photon efficiency (η_{ext}) of GNC-LSC waveguides under 360 nm monochromatic and AM1.5 illumination.

GNC-LSC Waveguide	η_{edge}	η_{int} (%)	η_{ext}^{360nm} (%)	$\eta_{ext}^{AM1.5}$ (%)	$\eta_{ext}^{simulation}$ (%)
1x1 cm^2	65.2	63.3	59.9	56.7	53.7
2x2 cm^2	57.2	55.5	52.6	49.7	48.5
3x3 cm^2	49.3	47.8	42.3	42.8	38.6
4x4 cm^2	46.8	45.4	42.9	40.6	36.2
5x5 cm^2	45.9	44.5	42.1	39.9	35.2
10x10 cm^2					33.9
25x25 cm^2					30.2
50x50 cm^2					27.8
100x100 cm^2					24.7

External photon efficiency was evaluated for both monochromatic 360 nm excitation and standard AM1.5G illumination. $\eta_{ext}^{360\,nm}$ decreases from 59.9% to 42.1% as size increases from 1×1 cm^2 to 5×5 cm^2, while $\eta_{ext}^{AM1.5}$ drops slightly from 42.1% to 39.9%. Simulations predict $\eta_{ext}^{simulation}$ values reaching 24.7% for waveguides up to 100×100 cm^2, confirming that large-area GNC waveguides retain strong photon collection and guiding capability under solar illumination.

Figure 5.4c outlines the methodology for evaluating optical losses as a function of propagation distance. The optical path corresponds to a horizontal midline through the device. Samples mounted in PLA holders were excited at 360 nm with a collimated 0.2×6000 μm^2 beam, and emission was collected at the right edge using a fixed fiber. The sample was translated into 5 mm increments to vary the optical path length. Time-resolved PL measurements were performed using a 450 nm pulsed laser in the same geometry.

Figure 5.4d shows the PL spectra of a 5×5 cm^2 waveguide as a function of optical path length (0–5 cm), alongside its absorption spectrum. Spectra from waveguides of other dimensions were also examined (within their allowable optical path ranges) to confirm the reproducibility and validity of the trends observed in the 5×5 cm^2 sample. For short optical paths, the emission strongly overlaps with the absorption spectrum; as the optical path increases to ~3.5 cm, the emission peak redshifts from 527 nm to 540 nm and gradually decreases in intensity. Beyond ~3.5 cm, the redshift saturates and intensity losses become minimal, indicating that reabsorption

dominates spectral evolution up to this threshold. At longer distances, non-unity PLQY and escape-cone losses become the main factors. Lifetime parameters for the 5×5 cm^2 sample (Table 5.4) also reflect this behavior: τ_1 increases slightly with distance (8.42 → 9.11 ns), suggesting altered recombination dynamics caused by reabsorption. Meanwhile, τ_2 decreases from 74.31 to ~59 ns, and $\tau_{average}$ decreases from 68.85 to ~50 ns, showing each photon recycling process occurs with a lower emission efficiency. Notably, the $\tau_{average}$ at 0.5 cm (68.85 ns) is significantly lower than that of the reference (112.67 ns), indicating that reabsorption is strong even at short distances but weakens as propagation length increases.

Table 5.4 Lifetime parameters for optical path dependent PL measurements for the largest sample, 5x5 cm^2.

Optical Path Length	Waveguide	τ_1 (non-radiative)	τ_2 (radiative)	τ_{ave} (average)	χ^2
0.5 cm	5x5 cm^2	8.42	74.31	68.85	1.024
2.5 cm		8.53	58.3	50.3	1.023
4.5 cm		9.11	58.81	51.43	1.012

Figure 5.4e plots the PL peak position and intensity versus optical path length, combining measurements up to 5 cm with extended Monte Carlo simulations up to 100 cm. The simulations involved injecting 10^5 monochromatic photons (360 nm) into a 1 mm subsurface region, a volume significantly smaller than the rectangular light beam used in the experiments. Boundary conditions were established by treating the three lateral and back faces as perfect black absorbers. Despite the larger excitation area, the simulations closely matched experimental trends. Both datasets show minimal spectral shift beyond 5 cm (from 541 nm at 5 cm to only 543 nm at 100 cm) and negligible intensity loss. These results confirm that once a critical optical path is reached, further increases in device size do not significantly increase total optical losses.

5.4 LSC Device Study

Figure 5.5a shows the custom-built platform used to integrate GNC-LSC waveguides with cut silicon solar cells for optoelectronic characterization under a solar simulator. No refractive index–matching material is used in this configuration. Figure 5.5b provides a schematic of the setup together with a photograph of the resized PERC c-Si cells (8.0×1.0 cm^2). The waveguides are held in PLA mounts

that mask the non-contact regions of the solar cells to eliminate direct illumination. The remaining exposed width of each cut-cell is shaded with an opaque black absorber to ensure accurate photocurrent measurements.

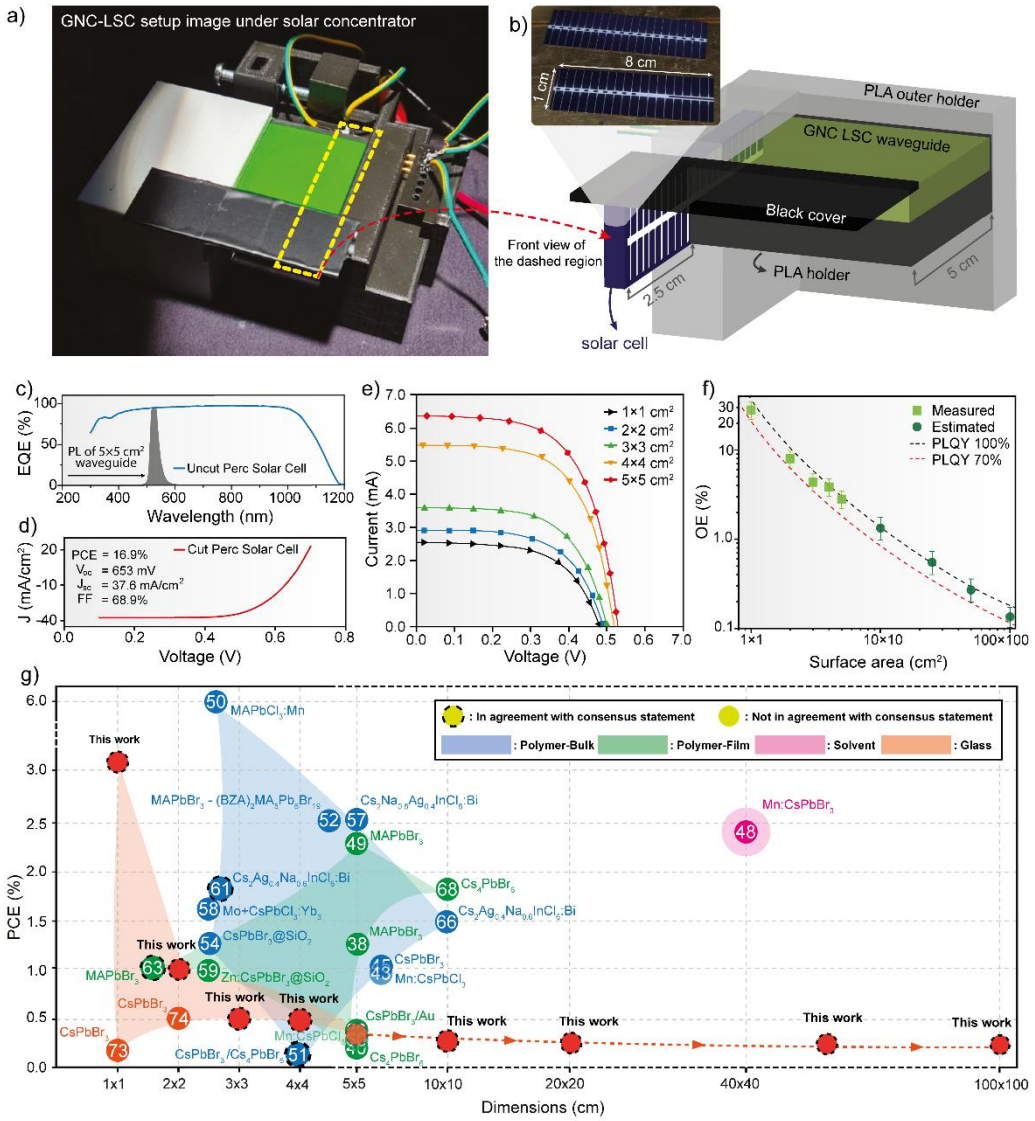


Figure 5.5 a) Custom measurement setup integrating GNC-LSC waveguides with cut silicon solar cells, shown here with a 5×5 cm^2 device under AM1.5 illumination. b) Schematic of the system layout and a photograph of the cut solar cell (8.0×1.0 cm^2). c) EQE spectrum of the uncut PERC cell overlaid with the PL emission range of a 5×5 cm^2 GNC-LSC waveguide. d) Electrical performance of the cut solar cell. e) I–V characteristics of GNC-LSC devices with sizes from 1×1 cm^2 to 5×5 cm^2. f) Optical efficiency (OE) of GNC-LSC devices spanning 1×1 cm^2 to 100×100 cm^2, showing experimental results (up to 5×5 cm^2) and analytical predictions (dashed lines). g) Power conversion efficiencies of GNC-LSC devices

(PCE_{lsc}) from 1×1 cm^2 to 100×100 cm^2, combining experimental data and simulation results, together with a comparison of representative PQD-based LSC studies across different hosts, PQD types, and device dimensions. Reported PCE values are evaluated for methodological consistency and linked to their original literature sources.

Figure 5.5c compares the EQE spectrum of the uncut PERC c-Si cell with the position-dependent PL spectrum of a 5×5 cm^2 waveguide. The silicon cell exhibits ~95% quantum efficiency across the full emission range of the waveguide, indicating excellent spectral compatibility for photon-to-electron conversion. The J–V curve of the cut cell is shown in Figure 5.5d. Cutting reduces the PCE from ~22% to 16.9%, due to reduced active area, edge damage, and contact disruption.

Figure 5.5e presents the I_{SC}–V_{OC} characteristics of GNC-LSC devices (additional data in Table 5.5). As device area increases, I_{SC} rises from 2.55 mA to 6.31 mA and V_{OC} increases from 0.48 V to 0.53 V, confirming that larger devices deliver higher photogenerated current and voltage. This scaling behavior is advantageous for BIPV applications, where a larger footprint can enhance instantaneous power output.

Table 5.5 Photovoltaic parameters of GNC-LSC devices as a function of device size, including experimentally measured values up to 5×5 cm^2 and simulated results for larger devices extending to 100×100 cm^2.

Surface area	$I_{sc,LSC}$ (mA)	$V_{oc,LSC}$ (V)	FF_{LSC} (%)	OE (%)	PCE (%)
1x1	2.55	0.48	67.08	27.13	3.17*
2x2	2.91	0.49	67.18	7.74	1.00*
3x3	3.59	0.50	68.36	4.26	0.55*
4x4	5.57	0.52	69.56	3.71	0.50*
5x5	6.31	0.53	70.71	2.78	0.38*
10x10	Simulation			1.32	0.36
25x25				0.53	0.33
50x50				0.26	0.30
100x100				0.13	0.28

Figure 5.5f summarizes the optical efficiency (OE%) of GNC-LSC devices ranging from 1×1 cm^2 to 100×100 cm^2. Experimental OE values are reported up to 5×5 cm^2, while analytical predictions based on equation 2.12 (η_{opt}^{Klimov}, dashed curves, using

various representative PLQY values) describe behavior at larger scales. The 1×1 cm^2 device exhibits a high OE of 27.1%, functioning primarily as a waveguide due to its unity geometric gain. OE decreases as surface area increases, while geometric gain improves. At 2×2 cm^2, OE is 3.5 times lower while gain doubles; at 3×3 cm^2, OE falls to 4.2% despite a threefold gain. Although earlier waveguide analyses suggest OE might plateau at large sizes, this stabilization is not observed. The analytical model assumes a fixed PL peak wavelength (based on the shortest optical path) and therefore does not account for dynamic peak shifting that affects the $\langle \alpha_2 \rangle$ term in equation 2.14. This simplification contributes to the divergence between experimental and modeled behaviors. Nevertheless, the model predicts OE values of 1.32% for 15×15 cm^2 (G = 15) and 0.13% for 100×100 cm^2 (G = 100).

Figure 5.5g presents the PCE values of GNC-LSCs across device sizes ranging from 1×1 cm^2 to 100×100 cm^2. Experimental measurements up to 5×5 cm^2 are corroborated by Monte Carlo simulations, while larger-area predictions rely solely on simulation output. Figure 5.5g also compiles PCE values from representative PQD-based LSC literature, including polymer films, bulk polymers, solvent-based systems, and glass hosts. Reported values are evaluated for methodological consistency following the consensus guidelines. [172] Further details—including encapsulation hosts, PQD types, device thickness, QY, OE, and relevant methodological inconsistencies—are provided in Table 5.6.

Table 5.6 Overview of PQD-based LSC studies categorized by encapsulating hosts, PQD luminophore types, host materials, LSC dimensions, thicknesses, quantum yield (QY) values, optical efficiencies (OE), and power conversion efficiencies (PCE). The table also highlights variations or compatibility with the consensus statement. (PCE and OE values represent the highest-performing or most representative examples reported in each study).

Host	Luminophore	Host Material	Dimension (cm^2)	Thickness (mm)	QY (%)	OE (%)	PCE (%)	Incompatibility with the consensus statement	Year	Ref.
Polymer-Bulk	$CsPb(Br_xI_{3-x})$	PLMA-EGDA	9.0x1.3	2.0	60.0	2.00	-	i, iv	2017	[96]
	$CsPb(Br_{0.8}I_{0.2})_3/(Br_{0.8}Cl_{0.2})_3$/CDs	PLMA-EGDA	10×10	2.0	70.0	3.05	-	vi	2018	[112]
	$CsPbBr_3$	Thiol-ene	6.0×6.0	5.0	78.0	2.11	1.06	vi	2021	[139]
	$Bi:Cs_2Ag_{0.4}Na_{0.6}InCl_6$	PMMA	10x10	2.0	39.2	0.7	1.5	i, ii	2021	[95]
	$Mn:MAPbCl_3$	PDMS	2.8×2.5	14.0	4.0	8.43	6.11	iii, iv	2021	[92]
	$Mn:CsPbCl_3$	Resin	6.0x6.0	5.0	40.7	2.23	0.97	vi	2022	[141]
	$CsPbBr_3/Cs_4PbBr_6$	PLA	4.0×4.0	3.0	65.0	0.15	0.05	*	2023	[148]
	$MAPbBr_3$-$(BZA)_2MA_5Pb_6Br_{19}$	PMMA	5.0x4.0	5.0	81.0	-	2.54	v	2024	[125]
	$CsPbBr_3@SiO_2$	PDMS	2.5x2.5	2.0	46.0	10.92	1.29	vi	2024	[135]
	$Cs_2Na_{0.6}Ag_{0.4}InCl_6$:Bi	PDMS	5.0x5.0	5.0	46.6	2.57	2.56	vi	2024	[136]
	$Mo+CsPbCl_3:Yb_3$	PMMA	2.5x2.5	3.0	92.4	-	1.62	i	2024	[126]
	$Bi:Cs_2Ag_{0.4}Na_{0.6}InCl_6$	Si-EL	2.6x2.6	3.0	57.0	5.40	1.85	*	2024	[183]
Polymer-Film	$FAPbBr_3$	PMMA	5.0×12	3.0	92.0	-	-	vi	2019	[127]
	Cs_4PbBr_6	PS	10×10	4.0	58	2.40	1.80	i, ii, v	2019	[184]
	Perovskite nano pellets	PMMA	10x10	2.0	70.0	0.87	-	i, ii	2019	[185]
	$(HA)_2(MA)_{n-1}Pb_nI_{3n+1}$	PMMA	10x10	2.0	56.0	2.00	-	vi	2020	[129]
	$CsPbBr_3$	PMMA	7.5x5.0	4.0	60.0	5.40	-	i, ii	2020	[130]
	$CsPbI_3$	PU	15×5.0	2.0	99.4	3.10	-	vi	2020	[147]
	Cs_4PbBr_6	PS	5.0x5.0	4.0	79.0	1.10	0.20	ii, iii	2021	[186]
	$Cs_3Cu_2I_5/CsCu_2I_3$	PMMA	3.5×2.0	5.0	-	1.15	-	i	2021	[131]
	$MAPbBr_3$	PMMA	5.0×5.0	4.5	-	12.26	2.35	i	2022	[132]
	$CsPbBr_3$	EVA	2.5×2.5	2.0	36.0	3.08	-	vi	2023	[149]
	$CsPbBr_3$/Au	Thiol-ene	5.0x5.0	5.0	61.0	2.90	0.44	vi	2023	[138]
	$MAPbBr_3$	PMMA	5.0x5.0	3.0	-	4.12	1.25	vi	2023	[106]
	$MAPbI_3$	P(VDF-TrFE)	2.0x1.5	2.0	88.6	5.82	1.01	*	2023	[150]
	$Zn:CsPbBr_3@SiO_2$	PDMS	2.5x2.5	2.5	51.5	9.30	0.98	i, ii	2024	[107]
	$Mn:CsPbCl_3$	PS	5.0x5.0	2.5	40.5	8.40	0.69	i	2024	[137]
	$PEA_2MA_{x-1}Pb_xBr_{3x+1}$	PVDF	5.0x5.0	1.5	81.8	5.10	-	i, ii	2024	[151]
Solvent	$MAPbI_3$	DMSO-NMP	15×15	10	-	29.00	-	vi	2016	[187]
	$Mn:CsPbBr_3$	Toluene	40×40	5.0	-	11.00	2.42	i	2022	[188]
	$PEA_2(Cs_{0.8}FA_{0.2})_{n-1}PbBr_{3n+1}$	DMSO	5.0x5.0	4.0	86.0	6.50	-	ii	2024	[189]
Glass	$CsPbBr_3$	Glass	1.0x1.0	1.5	9.2	-	0.17	vi	2020	[160]
	$CsPbBr_3$	Glass	2.0×2.0	1.1	81	6.17	0.57	i	2022	[161]
	$CsPbBr_xCl_{3-x}$	Glass	-	-	21.7	-	-	vi	2024	[159]
	$CsPbBr_3$	Glass	1.0×1.0	2.5	97	27.13	3.16	*	2025	**This work**
			5.0×5.0			2.78	0.38	*		
			100×100			0.13	0.30	*		

*Studies in agreement with the consensus statement [172] and studies that deviate from the consensus statement include those with: (i) no black background, (ii) no edge cover, (iii) a reflective background, (iv) a reflective edge cover, (v) non-standard illumination, and (vi) insufficient detail.

The 1×1 cm^2 device achieves a PCE of 3.16%, ranking among the highest values reported for glass-based LSCs. With increasing device size, PCE decreases to 1.00%, 0.55%, 0.50%, and 0.38% for 2×2 cm^2 to 5×5 cm^2, respectively. Monte Carlo simulations predict further reductions to 0.36%, 0.33%, 0.30%, and 0.28% for 10×10 to 100×100 cm^2 devices. While PCE drops sixfold from 1×1 to 3×3 cm^2, the decline slows beyond this point, with only a twofold reduction up to 1×1 m^2. These results reveal inherent scalability limits but also indicate that once waveguide-induced losses saturate, further design and materials optimization could improve light-concentration performance.

Most reported PQD-based LSCs rely on polymeric hosts, with PCEs up to 6.11% for small bulk-polymer devices (~2.5×2.5 cm^2). However, these high values often do not meet consensus measurement standards, such as requiring a true black background and complete edge masking. More rigorously reported polymer-bulk devices (10×10 cm^2) show maximum PCEs around 1.50%, although missing background and uncontrolled edge exposure limit comparability. Polymer-film LSCs show PCEs of 2.35% (5×5 cm^2) and 1.80% (10×10 cm^2), again compromised by measurement inconsistencies. Solvent-based LSCs containing PQDs have reached 2.42% for a large 40×40 cm^2 device, though the lack of proper background control inflated this value.

GNC-based LSCs have been explored in only a few studies. Laser-induced crystallization of $CsPbBr_3$ [160] and $CsPbBr_XCl_{3-x}$ [159] PQDs in glass produced extremely low PCEs due to limited PQD volume. Another proof-of-concept using ultrathin $CsPbBr_3$ GNC sheets (2×2 cm^2) reported PCEs of 0.57–0.06%, but the approach suffers from fragility and scalability constraints. [161]

In contrast, this work achieves a record PCE of 3.16% for small-scale GNC-based LSCs, decreasing to 0.38% for mid-scale (5×5 cm^2) devices. Simulations indicate that even for exceptionally large devices (1×1 m^2), PCE remains around 0.30%, demonstrating strong scalability and practical feasibility for large-area BIPV applications.

6
CONCLUSION

6.1 Conclusions

This thesis successfully establishes durable and scalable glass-based LSCsas a superior alternative to conventional polymer LSCs for BIPV applications. Two complementary solutions were proposed by employing Eu^{3+}-doped glasses and $CsPbBr_3$ PQD-GNCs, adressing the trade-off between aesthetic neutrality and high photon-conversion efficiency.

Eu^{3+}-doped borosilicate glasses are demonstrated to be ideal for BIPV applications that require high transparency and color neutrality, due to their ~90% AVT and near-perfect color rendering (CRI 98). The large Stokes shift of Eu^{3+} ions effectively surpresses reabsorption losses, as evidenced by the size-invariant external photon efficiency (η_{ext} ~6.4%) across all device dimensions. Although the PCE_{lsc} decreases from 0.852% (2×2 cm^2) to 0.164% (6×6 cm^2) due to geometric scaling, the total current, voltage, and power outputs increase with size. These results confirm that lanthanide-doped glassLSCs maintain meaningful electrical performance, transparency and color-neutrality even at large scales, supporting seamless integration into building facades for BIPV applications.

In PQD-GNC LSCs, the combination of a broad absorption and high QY ≈ 97% enables efficientphoton-conversion. At the 1×1 cm^2 scale (G=1), the device achieved a PCE_{lsc} of 3.16%, an optical efficiency of 27.13%, and a η_{ext} of 53.7%.Increasing the scale to 3×3 cm^2 (G = 3) reduced these values to 0.55%, 4.26%, and 38.6%, respectively, whilefurther expansion to 5×5 cm^2 (G = 5) led to a PCE_{lsc} of 0.38%, an optical efficiency of 2.78%, and a η_{ext} of 35.2%. Simulations up to 100×100 cm^2 (G = 100) projected a PCE_{lsc} of 0.28%, an optical efficiency of

0.13%, and a η_{ext} of 24.7%. Notably, a 100-fold increase in geometric gain produces only a twofold decrease in η_{ext}, indicating that waveguide-related losses are effectively managed in the GNC matrix. The PCE_{lsc} decline reaches a saturation threshold at a geometric gain of ~3, beyond which performance remains stable, confirming that waveguide losses and geometric gain reach equilibrium and validating the feasibility of large-area PQD-GNC LSCs. Notably, while experimental trends reflect this stabilization, empirical optical efficiency values may underestimate the behavior due to limitations in analytical modeling.

Overall, Eu^{3+}-doped glasses and PQD-GNCs emerge as complementary platforms, emphasizing aesthetic neutrality and high photon-conversion efficiency, respectively. These findings confirm the feasibility of durable, scalable glass-based LSCs that provide both high design flexibility and robust performance for architectural BIPV applications.

6.2 Future Outlook

The outputs obtained in this thesis provide a roadmap for transitioning glass-based LSC technology from the laboratory scale to commercial building facades. The following directions are of critical importance for future research:

- LSC performance is contingent not only on the efficiency of the luminophore but also on the constructive interaction between the photonic collector and the PV cell. Consequently, rather than pursuing isolated and potentially impractical improvements in luminophore performance, a holistic design paradigm focused on optimizing the equilibrium between all system components must be established.
- One of the most critical factors limiting efficiency observed in current prototypes is the microscopic air gaps at the glass-PV interface. In future designs, the development of advanced index-matching optical adhesives that minimize light escape and cell mounting techniques fully compatible with waveguide geometry should be considered to minimize device-level losses.
- Since LSC devices operate with narrow-band fluorescent emission rather than direct sunlight, the design principle should shift from "broad-spectrum absorption" to "full spectral overlap between luminophore emission and PV cell sensitivity." In the future, integrating perovskite solar cells with bandgaps

specifically tuned to respond to various emission bands, or high-performance III-V semiconductors like GaAs into the LSC edges, will bring system PCE values closer to theoretical limits.

- Harvesting the entire solar spectrum with a single luminophore is challenging; therefore, future studies should focus on multi-layered (tandem) LSC architectures. For instance, the aesthetic neutrality of the Eu^{3+}-doped glasses investigated in this thesis can be combined with the high photon conversion capacity of PQD-GNCs in a layered structure within the same device. This would expand the spectral coverage without compromising visual quality. Additionally, increasing light trapping efficiency through scattering centers integrated into the waveguide should be evaluated as another structural design strategy.
- The observation in PQD-GNC based LSCs that reabsorption-induced losses stabilize (reaching a plateau) after a certain critical path length presents an opportunity for large-scale modules. Future design principles should focus on determining optimized cell-to-edge ratios that minimize photon loss in meter-scale facade panels by leveraging this "plateau effect." Monte Carlo simulations predict that a stable efficiency regime can be maintained even over large areas such as 1 m^2.
- For the transition of LSC technology from the laboratory to industry, the international consensus measurement protocols applied in this thesis (e.g., use of black background, full edge masking) must be transformed into industrial standards. In the future, characterizing glass-based LSCs not only by their optical performance but also through fire resistance, wind load resistance, and long-term outdoor aging tests in accordance with building regulations will solidify the technology's position in the BIPV market**.**

7
REFERENCES

[1] IEA, *Empowering Cities for a Net Zero Future*, Paris, **2021**.

[2] Ember, *Global Electricity Review 2024*, **2024**.

[3] Q. Hassan, P. Viktor, T. J. Al-Musawi, B. Mahmood Ali, S. Algburi, H. M. Alzoubi, A. Khudhair Al-Jiboory, A. Zuhair Sameen, H. M. Salman, M. Jaszczur, *Renewable Energy Focus* **2024**, *48*, 100545.

[4] W. Shen, Y. Zhao, F. Liu, *Frontiers in Energy* **2024**, *18*, 8.

[5] J. Rantaniemi, J. Jääskeläinen, J. Lassila, S. Honkapuro, *Energies (Basel)*. **2022**, *15*, 423.

[6] Z. Li, T. Ma, H. Yang, L. Lu, R. Wang, *Solar RRL* **2021**, *5*, DOI: 10.1002/solr.202000614.

[7] B. Petter Jelle, C. Breivik, H. Drolsum Røkenes, *Solar Energy Materials and Solar Cells* **2012**, *100*, 69.

[8] C. Xiang, B. S. Matusiak, A. Røyset, T. Kolås, *Solar Energy* **2021**, *224*, 1222.

[9] K. Lee, H.-D. Um, D. Choi, J. Park, N. Kim, H. Kim, K. Seo, *Cell Rep. Phys. Sci.* **2020**, *1*, 100143.

[10] H. Lee, H. Song, *WIREs Energy and Environment* **2021**, *10*, DOI: 10.1002/wene.403.

[11] T. A. de Bruin, W. G. J. H. M. van Sark, *Adv. Photonics Res.* **2025**, *6*, DOI: 10.1002/adpr.202400068.

[12] S. Castelletto, A. Boretti, *Nano Energy* **2023**, *109*, 108269.

[13] Q. Nie, K. Li, W. Li, F. Liu, X. Luo, *Renewable and Sustainable Energy Reviews* **2026**, *227*, 116557.

[14] J. ter Schiphorst, M. L. M. K. H. Y. K. Cheng, M. van der Heijden, R. L. Hageman, E. L. Bugg, T. J. L. Wagenaar, M. G. Debije, *Energy Build.* **2020**, *207*, 109625.

[15] J. Roncali, *Adv. Energy Mater.* **2020**, *10*, DOI: 10.1002/aenm.202001907.

[16] J.-M. Delgado-Sanchez, *Solar Energy Materials and Solar Cells* **2019**, *202*, 110134.

[17] L. H. Slooff, E. E. Bende, A. R. Burgers, T. Budel, M. Pravettoni, R. P. Kenny, E. D. Dunlop, A. Büchtemann, *physica status solidi (RRL) – Rapid Research Letters* **2008**, *2*, 257.

[18] L. Desmet, A. J. M. Ras, D. K. G. de Boer, M. G. Debije, *Opt. Lett.* **2012**, *37*, 3087.

[19] F. Mateen, S. Y. Lee, S.-K. Hong, *J. Mater. Chem. A Mater.* **2020**, *8*, 3708.

[20] J. L. Banal, B. Zhang, D. J. Jones, K. P. Ghiggino, W. W. H. Wong, *Acc. Chem. Res.* **2017**, *50*, 49.

[21] I. Motta, G. Bottaro, M. Rando, M. Rancan, R. Seraglia, L. Armelao, *J. Mater. Chem. A Mater.* **2024**, *12*, 22516.

[22] X. Wang, T. Wang, X. Tian, L. Wang, W. Wu, Y. Luo, Q. Zhang, *Solar Energy* **2011**, *85*, 2179.

[23] J. Wang, T. Cai, O. Chen, *Nano Lett.* **2023**, *23*, 4367.

[24] G. Liu, X. Wang, G. Han, J. Yu, H. Zhao, *Mater. Adv.* **2020**, *1*, 119.

[25] P. Moraitis, R. E. I. Schropp, W. G. J. H. M. van Sark, *Opt. Mater. (Amst).* **2018**, *84*, 636.

[26] M. G. Debije, P. P. C. Verbunt, *Adv. Energy Mater.* **2012**, *2*, 12.

[27] X. Li, J. Qi, J. Zhu, Y. Jia, Y. Liu, Y. Li, H. Liu, G. Li, K. Wu, *J. Phys. Chem. Lett.* **2022**, *13*, 9177.

[28] B. Zhang, G. Lyu, E. A. Kelly, R. C. Evans, *Advanced Science* **2022**, *9*, DOI: 10.1002/advs.202201160.

[29] C. Tummeltshammer, M. Portnoi, S. A. Mitchell, A.-T. Lee, A. J. Kenyon, A. B. Tabor, I. Papakonstantinou, *Nano Energy* **2017**, *32*, 263.

[30] B. Zhang, P. Zhao, L. J. Wilson, J. Subbiah, H. Yang, P. Mulvaney, D. J. Jones, K. P. Ghiggino, W. W. H. Wong, *ACS Energy Lett.* **2019**, *4*, 1839.

[31] Y. Zhou, H. Zhao, D. Ma, F. Rosei, *Chem. Soc. Rev.* **2018**, *47*, 5866.

[32] J. Bomm, A. Büchtemann, A. J. Chatten, R. Bose, D. J. Farrell, N. L. A. Chan, Y. Xiao, L. H. Slooff, T. Meyer, A. Meyer, W. G. J. H. M. van Sark, R. Koole, *Solar Energy Materials and Solar Cells* **2011**, *95*, 2087.

[33] F. Meinardi, A. Colombo, K. A. Velizhanin, R. Simonutti, M. Lorenzon, L. Beverina, R. Viswanatha, V. I. Klimov, S. Brovelli, *Nat. Photonics* **2014**, *8*, 392.

[34] S. Brovelli, R. D. Schaller, S. A. Crooker, F. García-Santamaría, Y. Chen, R. Viswanatha, J. A. Hollingsworth, H. Htoon, V. I. Klimov, *Nat. Commun.* **2011**, *2*, 280.

[35] B. N. Pal, Y. Ghosh, S. Brovelli, R. Laocharoensuk, V. I. Klimov, J. A. Hollingsworth, H. Htoon, *Nano Lett.* **2012**, *12*, 331.

[36] C. K. Gordon, L. D. Browne, S. Chan, M. W. Brett, C. Zemke-Smith, J. Hardy, M. B. Price, N. J. L. K. Davis, *ACS Appl. Mater. Interfaces* **2023**, *15*, 17914.

[37] H.-J. Song, B. G. Jeong, J. Lim, D. C. Lee, W. K. Bae, V. I. Klimov, *Nano Lett.* **2018**, *18*, 395.

[38] L. R. Bradshaw, K. E. Knowles, S. McDowall, D. R. Gamelin, *Nano Lett.* **2015**, *15*, 1315.

[39] Y. Zhou, D. Benetti, Z. Fan, H. Zhao, D. Ma, A. O. Govorov, A. Vomiero, F. Rosei, *Adv. Energy Mater.* **2016**, *6*, DOI: 10.1002/aenm.201501913.

[40] B. Liu, S. Ren, G. Han, H. Zhao, X. Huang, B. Sun, Y. Zhang, *J. Mater. Chem. C Mater.* **2021**, *9*, 5723.

[41] J. L. Pelley, A. S. Daar, M. A. Saner, *Toxicological Sciences* **2009**, *112*, 276.

[42] C. Li, W. Chen, D. Wu, D. Quan, Z. Zhou, J. Hao, J. Qin, Y. Li, Z. He, K. Wang, *Sci. Rep.* **2015**, *5*, 17777.

[43] M. R. Bergren, N. S. Makarov, K. Ramasamy, A. Jackson, R. Guglielmetti, H. McDaniel, *ACS Energy Lett.* **2018**, *3*, 520.

[44] A. Anand, M. L. Zaffalon, G. Gariano, A. Camellini, M. Gandini, R. Brescia, C. Capitani, F. Bruni, V. Pinchetti, M. Zavelani-Rossi, F. Meinardi, S. A. Crooker, S. Brovelli, *Adv. Funct. Mater.* **2020**, *30*, DOI: 10.1002/adfm.201906629.

[45] N. S. Makarov, D. Korus, D. Freppon, K. Ramasamy, D. W. Houck, A. Velarde, A. Parameswar, M. R. Bergren, H. McDaniel, *ACS Appl. Mater. Interfaces* **2022**, *14*, 29679.

[46] F. Meinardi, H. McDaniel, F. Carulli, A. Colombo, K. A. Velizhanin, N. S. Makarov, R. Simonutti, V. I. Klimov, S. Brovelli, *Nat. Nanotechnol.* **2015**, *10*, 878.

[47] K. Wu, H. Li, V. I. Klimov, *Nat. Photonics* **2018**, *12*, 105.

[48] K. Gungor, J. Du, V. I. Klimov, *ACS Energy Lett.* **2022**, *7*, 1741.

[49] Y. Lai, Y. Chen, L. Wang, X. Zhao, K. Zheng, J. Zhong, X. Tong, R. Wang, F. Rosei, Y. Zhou, *Nano Energy* **2025**, *135*, 110632.

[50] Y. Wu, J. Huang, J. Zang, J. Zhou, C. Cheng, Z. Hu, D. Shan, W. Yang, I. Sychugov, L. Sun, B. Xu, *Energy Environ. Sci.* **2024**, *17*, 6338.

[51] R. Terricabres-Polo, T. A. de Bruin, A. Kaul, W. G. J. H. M. van Sark, C. de M. Donega, *Adv. Energy Mater.* **2024**, *14*, DOI: 10.1002/aenm.202402375.

[52] L. Dhamo, F. Carulli, P. Nickl, K. D. Wegner, V. Hodoroaba, C. Würth, S. Brovelli, U. Resch-Genger, *Adv. Opt. Mater.* **2021**, *9*, DOI: 10.1002/adom.202100587.

[53] Y. You, X. Tong, A. Imran Channa, H. Zhi, M. Cai, H. Zhao, L. Xia, G. Liu, H. Zhao, Z. Wang, *Chemical Engineering Journal* **2023**, *452*, 139490.

[54] H. Zhi, X. Tong, Y. You, A. I. Channa, X. Li, J. Wu, G. S. Selopal, Z. M. Wang, *Solar RRL* **2023**, *7*, DOI: 10.1002/solr.202300641.

[55] H. J. Lee, S. Im, D. Jung, K. Kim, J. A. Chae, J. Lim, J. W. Park, D. Shin, K. Char, B. G. Jeong, J.-S. Park, E. Hwang, D. C. Lee, Y.-S. Park, H.-J. Song, J. H. Chang, W. K. Bae, *Nat. Commun.* **2023**, *14*, 3779.

[56] Y. Chen, F. Ge, Y. Lai, L. Wang, X. Zhao, R. Wang, S. Peng, X.-J. Wu, Y. Zhou, *ACS Appl. Mater. Interfaces* **2024**, *16*, 14072.

[57] F. Meinardi, F. Bruni, C. Castellan, M. Meucci, A. M. Umair, M. La Rosa, J. Catani, S. Brovelli, *Adv. Energy Mater.* **2024**, *14*, DOI: 10.1002/aenm.202304006.

[58] M. Siripurapu, F. Meinardi, S. Brovelli, F. Carulli, *ACS Photonics* **2023**, *10*, 2987.

[59] Y. Li, P. Miao, W. Zhou, X. Gong, X. Zhao, *J. Mater. Chem. A* **2017**, *5*, 21452.

[60] Z. Wang, X. Zhao, Z. Guo, P. Miao, X. Gong, *Org. Electron.* **2018**, *62*, 284.

[61] X. Gong, W. Ma, Y. Li, L. Zhong, W. Li, X. Zhao, *Org. Electron.* **2018**, *63*, 237.

[62] X. Liu, D. Benetti, F. Rosei, *J. Mater. Chem. A Mater.* **2021**, *9*, 23345.

[63] J. Li, W. Li, H. Wang, X. Zhao, X. Gong, *Appl. Energy* **2024**, *358*, 122571.

[64] J. Guo, Y. Lu, A. Xie, G. Li, Z. Liang, C. Wang, X. Yang, S. Chen, *Adv. Funct. Mater.* **2022**, *32*, DOI: 10.1002/adfm.202110393.

[65] L. Wang, X. Wang, H. Zhao, *Adv. Funct. Mater.* **2025**, *35*, DOI: 10.1002/adfm.202423422.

[66] Y. Zhou, D. Benetti, X. Tong, L. Jin, Z. M. Wang, D. Ma, H. Zhao, F. Rosei, *Nano Energy* **2018**, *44*, 378.

[67] J. Gan, Q. Lin, Y. Huang, Y. Wu, W. Yu, *ACS Nano* **2023**, *17*, 23512.

[68] H. Zhao, G. Liu, G. Han, *Nanoscale Adv.* **2019**, *1*, 4888.

[69] H. Zhao, G. Liu, S. You, F. V. A. Camargo, M. Zavelani-Rossi, X. Wang, C. Sun, B. Liu, Y. Zhang, G. Han, A. Vomiero, X. Gong, *Energy Environ. Sci.* **2021**, *14*, 396.

[70] J. Li, H. Zhao, X. Zhao, X. Gong, *Nanoscale Horiz.* **2023**, *8*, 83.

[71] J. Li, H. Zhao, X. Zhao, X. Gong, *Adv. Funct. Mater.* **2024**, *34*, DOI: 10.1002/adfm.202404473.

[72] X. Gong, S. Zheng, X. Zhao, A. Vomiero, *Nano Energy* **2022**, *101*, 107617.

[73] K.-B. Cai, H.-Y. Huang, M.-L. Hsieh, P.-W. Chen, S.-E. Chiang, S. H. Chang, J.-L. Shen, W.-R. Liu, C.-T. Yuan, *ACS Nano* **2022**, *16*, 3994.

[74] S. Li, L. Li, H. Tu, H. Zhang, D. S. Silvester, C. E. Banks, G. Zou, H. Hou, X. Ji, *Materials Today* **2021**, *51*, 188.

[75] T. Hu, Z. Wen, C. Wang, T. Thomas, C. Wang, Q. Song, M. Yang, *Nanoscale Adv.* **2019**, *1*, 1413.

[76] M. J. Talite, H.-Y. Huang, Y.-H. Wu, P. G. Sena, K.-B. Cai, T.-N. Lin, J.-L. Shen, W.-C. Chou, C.-T. Yuan, *ACS Appl. Mater. Interfaces* **2018**, *10*, 34184.

[77] M. J. Talite, H.-Y. Huang, K.-B. Cai, K. C. Capinig Co, P. A. Cynthia Santoso, S.-H. Chang, W.-C. Chou, C.-T. Yuan, *J. Phys. Chem. Lett.* **2020**, *11*, 567.

[78] Y. Wu, Y. Zhan, W. Xin, W. Cao, J. Li, M. Chen, X. Jiang, J. Wang, Z. Sun, *ACS Appl. Energy Mater.* **2022**, *5*, 1781.

[79] H.-Y. Huang, M. J. Talite, K.-B. Cai, R. J. Soebroto, S.-H. Chang, W.-R. Liu, W.-C. Chou, C.-T. Yuan, *Nanoscale* **2020**, *12*, 23537.

[80] J. Li, J. Chen, X. Zhao, A. Vomiero, X. Gong, *Nano Energy* **2023**, *115*, 108674.

[81] R. Anthony, U. Kortshagen, *Phys. Rev. B* **2009**, *80*, 115407.

[82] F. Meinardi, S. Ehrenberg, L. Dhamo, F. Carulli, M. Mauri, F. Bruni, R. Simonutti, U. Kortshagen, S. Brovelli, *Nat. Photonics* **2017**, *11*, 177.

[83] S. Ren, C. Shou, S. Jin, G. Chen, S. Han, Z. Chen, X. Chen, S. Yang, Y. Guo, C.-C. Tu, *ACS Photonics* **2021**, *8*, 2392.

[84] R. Mazzaro, F. Romano, P. Ceroni, *Phys. Chem. Chem. Phys.* **2017**, *19*, 26507.

[85] B. G. Lee, J.-W. Luo, N. R. Neale, M. C. Beard, D. Hiller, M. Zacharias, P. Stradins, A. Zunger, *Nano Lett.* **2016**, *16*, 1583.

[86] R. J. Anthony, D. J. Rowe, M. Stein, J. Yang, U. Kortshagen, *Adv. Funct. Mater.* **2011**, *21*, 4042.

[87] L. Lian, M. Zheng, P. Zhang, Z. Zheng, K. Du, W. Lei, J. Gao, G. Niu, D. Zhang, T. Zhai, S. Jin, J. Tang, X. Zhang, J. Zhang, *Chemistry of Materials* **2020**, *32*, 3462.

[88] H. Zhao, R. Sun, Z. Wang, K. Fu, X. Hu, Y. Zhang, *Adv. Funct. Mater.* **2019**, *29*, DOI: 10.1002/adfm.201902262.

[89] Z. Zhou, Y. Li, Z. Xing, H. H. Y. Sung, I. D. Williams, Z. Li, K. S. Wong, J. E. Halpert, *Adv. Mater. Interfaces* **2021**, *8*, DOI: 10.1002/admi.202101471.

[90] Y. Liu, N. Li, R. Sun, W. Zheng, T. Liu, H. Li, Y. Chen, G. Liu, H. Zhao, H. Liu, Y. Zhang, *Nano Energy* **2021**, *85*, 105960.

[91] F. Meinardi, Q. A. Akkerman, F. Bruni, S. Park, M. Mauri, Z. Dang, L. Manna, S. Brovelli, *ACS Energy Lett.* **2017**, *2*, 2368.

[92] S. S. Bhosale, E. Jokar, Y.-T. Chiang, C.-H. Kuan, K. Khodakarami, Z. Hosseini, F.-C. Chen, E. W.-G. Diau, *ACS Appl. Energy Mater.* **2021**, *4*, 10565.

[93] T. A. Cohen, T. J. Milstein, D. M. Kroupa, J. D. MacKenzie, C. K. Luscombe, D. R. Gamelin, *J. Mater. Chem. A Mater.* **2019**, *7*, 9279.

[94] T. Cai, J. Wang, W. Li, K. Hills-Kimball, H. Yang, Y. Nagaoka, Y. Yuan, R. Zia, O. Chen, *Advanced Science* **2020**, *7*, DOI: 10.1002/advs.202001317.

[95] L. Zdražil, S. Kalytchuk, M. Langer, R. Ahmad, J. Pospíšil, O. Zmeškal, M. Altomare, A. Osvet, R. Zbořil, P. Schmuki, C. J. Brabec, M. Otyepka, Š. Kment, *ACS Appl. Energy Mater.* **2021**, *4*, 6445.

[96] H. Zhao, Y. Zhou, D. Benetti, D. Ma, F. Rosei, *Nano Energy* **2017**, *37*, 214.

[97] X. Luo, T. Ding, X. Liu, Y. Liu, K. Wu, *Nano Lett.* **2019**, *19*, 338.

[98] B. Mendewala, E. T. Vickers, K. Nikolaidou, A. DiBenedetto, W. G. Delmas, J. Z. Zhang, S. Ghosh, *Adv. Opt. Mater.* **2021**, *9*, 2100754.

[99] L. Liao, T. Lin, X. Bin, K. Quan, L. Zhang, R. Zeng, J. Zhai, X. Mo, J. Zhao, *J. Lumin.* **2022**, *248*, 118927.

[100] P. Xia, H. Sun, H. Guo, K. Zhao, C. Liang, C. Lu, Z. Wang, S. Xu, C. Wang, *Adv. Funct. Mater.* **2024**, *34*, 2401121.

[101] C.-H. Chou, M.-H. Hsu, F.-C. Chen, *Nano Energy* **2015**, *15*, 729.

[102] H. Liu, S. Li, W. Chen, D. Wang, C. Li, D. Wu, J. Hao, Z. Zhou, X. Wang, K. Wang, *Solar Energy Materials and Solar Cells* **2018**, *179*, 380.

[103] C. Jin, C. Feng, Y. Chen, T. Zhang, H. He, H. Na, J. Zhu, *Energy Environ. Sci.* **2024**, *17*, 5931.

[104] M. J. Currie, J. K. Mapel, T. D. Heidel, S. Goffri, M. A. Baldo, *Science (1979).* **2008**, *321*, 226.

[105] J. C. Goldschmidt, M. Peters, A. Bösch, H. Helmers, F. Dimroth, S. W. Glunz, G. Willeke, *Solar Energy Materials and Solar Cells* **2009**, *93*, 176.

[106] E. C. S. Mahen, A. R. Ummah, F. A. Permatasari, Suprijadi, A. H. Aimon, F. Iskandar, *Mater. Lett.* **2023**, *337*, 134008.

[107] C. Li, Y. Gao, Z. Ren, S. Xiong, C. Li, J. Wu, J. Li, X. Wang, J. Wang, *J. Mater. Chem. C Mater.* **2025**, *13*, 945.

[108] L. Zdražil, S. Kalytchuk, K. Holá, M. Petr, O. Zmeškal, Š. Kment, A. L. Rogach, R. Zbořil, *Nanoscale* **2020**, *12*, 6664.

[109] J. Wang, J. Wang, Y. Xu, J. Jin, W. Xiao, D. Tan, J. Li, T. Mei, L. Xue, X. Wang, *ACS Appl. Energy Mater.* **2020**, *3*, 12230.

[110] J. Li, H. Zhao, X. Zhao, X. Gong, *Nanoscale* **2021**, *13*, 9561.

[111] Y. Han, X. Zhao, A. Vomiero, X. Gong, H. Zhao, *J. Mater. Chem. C Mater.* **2021**, *9*, 12255.

[112] H. Zhao, D. Benetti, X. Tong, H. Zhang, Y. Zhou, G. Liu, D. Ma, S. Sun, Z. M. Wang, Y. Wang, F. Rosei, *Nano Energy* **2018**, *50*, 756.

[113] J. Chen, H. Zhao, Z. Li, X. Zhao, X. Gong, *Energy Environ. Sci.* **2022**, *15*, 799.

[114] J. Graffion, X. Cattoën, M. Wong Chi Man, V. R. Fernandes, P. S. André, R. A. S. Ferreira, L. D. Carlos, *Chemistry of Materials* **2011**, *23*, 4773.

[115] W. Ma, W. Li, R. Liu, M. Cao, X. Zhao, X. Gong, *Chemical Communications* **2019**, *55*, 7486.

[116] J. Song, C. Kim, S. Lee, H. Lee, J. Seo, H.-J. Song, *Korean Journal of Chemical Engineering* **2024**, *41*, 3573.

[117] B. S. Richards, I. A. Howard, *Energy Environ. Sci.* **2023**, *16*, 3214.

[118] G. Griffini, *Front. Mater.* **2019**, *6*, DOI: 10.3389/fmats.2019.00029.

[119] T. Warner, K. P. Ghiggino, G. Rosengarten, *Solar Energy* **2022**, *246*, 119.

[120] M. Cao, X. Zhao, X. Gong, *JACS Au* **2023**, *3*, 25.

[121] E. Tatsi, A. Nitti, D. Pasini, G. Griffini, *Nanoscale* **2024**, *16*, 15502.

[122] L. Jin, G. S. Selopal, X. Liu, D. Benetti, F. Rosei, *Adv. Funct. Mater.* **2024**, *34*, DOI: 10.1002/adfm.202405653.

[123] T. Wei, K. Lian, J. Tao, H. Zhang, D. Xu, J. Han, C. Fan, Z. Zhang, W. Bi, C. Sun, *ACS Appl. Mater. Interfaces* **2022**, *14*, 44572.

[124] G. Griffini, M. Levi, S. Turri, *Solar Energy Materials and Solar Cells* **2013**, *118*, 36.

[125] E. Bagherzadeh-Khajehmarjan, S. Ahmadi-Kandjani, N. AmirKooshesh, S. Rajabi-Ghaleh, *Int. J. Energy Res.* **2024**, *2024*, DOI: 10.1155/2024/1155917.

[126] J. Choi, S.-J. Kim, *J. Mater. Chem. C Mater.* **2024**, *12*, 12026.

[127] J. Tong, J. Luo, L. Shi, J. Wu, L. Xu, J. Song, P. Wang, H. Li, Z. Deng, *J. Mater. Chem. A Mater.* **2019**, *7*, 4872.

[128] M. Wei, F. P. G. de Arquer, G. Walters, Z. Yang, L. N. Quan, Y. Kim, R. Sabatini, R. Quintero-Bermudez, L. Gao, J. Z. Fan, F. Fan, A. Gold-Parker, M. F. Toney, E. H. Sargent, *Nat. Energy* **2019**, *4*, 197.

[129] Z. Li, A. Johnston, M. Wei, M. I. Saidaminov, J. Martins de Pina, X. Zheng, J. Liu, Y. Liu, O. M. Bakr, E. H. Sargent, *Joule* **2020**, *4*, 631.

[130] A. K. Singh, *Methods Appl. Fluoresc.* **2020**, *8*, 045008.

[131] Y. Gu, X. Yao, H. Geng, G. Guan, M. Hu, M. Han, *ACS Appl. Mater. Interfaces* **2021**, *13*, 40798.

[132] H. Oh, G. Kang, M. Park, *ACS Appl. Energy Mater.* **2022**, *5*, 15844.

[133] T. Wang, J. Zhang, W. Ma, Y. Luo, L. Wang, Z. Hu, W. Wu, X. Wang, G. Zou, Q. Zhang, *Solar Energy* **2011**, *85*, 2571.

[134] Y. Wang, G. Xie, J. Chen, X. Zhang, C. Chen, J. Yin, H. Li, *J. Mater. Chem. C Mater.* **2022**, *10*, 11924.

[135] X. Wang, J. Wu, D. Huang, J. Yan, C. Li, Z. Ren, J. Li, X. Wang, J. Wang, *Chemical Engineering Journal* **2024**, *480*, 148139.

[136] S. Li, Y. Zhang, Z. Song, Z. Zheng, X. Zhang, X. Liu, *J. Mater. Chem. C Mater.* **2024**, *12*, 10096.

[137] S. Oh, S. W. Bae, T. H. Kim, G. Kang, H. Jung, Y.-H. Kim, M. Park, *J. Mater. Chem. A Mater.* **2024**, *12*, 33193.

[138] X. Cao, Z. Zheng, Y. Zhang, Y. Tian, K. Ye, C. Luo, H. Zhang, X. Zhang, *J. Lumin.* **2023**, *260*, 119889.

[139] G. Gu, X. Zhang, Y. Guo, Z. Zheng, X. Cao, Y. Zhang, R. Huang, X. Zhang, *Appl. Phys. Lett.* **2021**, *119*, DOI: 10.1063/5.0059847.

[140] A. F. Bertozzi, A. Picchi, A. Pucci, *Macromol. Chem. Phys.* **2023**, *224*, DOI: 10.1002/macp.202200392.

[141] G. Gu, Z. Zheng, H. Zhang, Y. Zhang, Z. Gan, R. Huang, X. Zhang, *J. Lumin.* **2022**, *248*, 118963.

[142] J. Graffion, A. M. Cojocariu, X. Cattoën, R. A. S. Ferreira, V. R. Fernandes, P. S. André, L. D. Carlos, M. Wong Chi Man, J. R. Bartlett, *J. Mater. Chem.* **2012**, *22*, 13279.

[143] M. M. Nolasco, P. M. Vaz, V. T. Freitas, P. P. Lima, Paulo. S. André, R. A. S. Ferreira, P. D. Vaz, P. Ribeiro-Claro, L. D. Carlos, *J. Mater. Chem. A Mater.* **2013**, *1*, 7339.

[144] S. F. H. Correia, V. de Zea Bermudez, S. J. L. Ribeiro, P. S. André, R. A. S. Ferreira, L. D. Carlos, *J. Mater. Chem. A* **2014**, *2*, 5580.

[145] M. Tonezzer, G. Maggioni, A. Campagnaro, S. Carturan, A. Quaranta, M. della Pirriera, D. Gutierrez Tauste, *Progress in Photovoltaics: Research and Applications* **2015**, *23*, 1037.

[146] Y. Wang, Y. Liu, G. Xie, J. Chen, P. Li, Y. Zhang, H. Li, *ACS Appl. Mater. Interfaces* **2022**, *14*, 5951.

[147] J. Wu, J. Tong, Y. Gao, A. Wang, T. Zhang, H. Tan, S. Nie, Z. Deng, *Angewandte Chemie International Edition* **2020**, *59*, 7738.

[148] S. Ebrahimisadr, B. Olyaeefar, S. Ahmadi-kandjani, *Phys. Scr.* **2023**, *98*, 015833.

[149] C. Cai, M. Wang, J. Wang, B. Xu, J. Wang, L. Zhang, W. Xin, L. Xue, J. Li, X. Wang, *Appl. Surf. Sci.* **2023**, *609*, 155313.

[150] P. Xia, H. Sun, S. Xu, T. Zhou, S. Zong, C. Lu, C. Wang, *Adv. Energy Mater.* **2023**, *13*, DOI: 10.1002/aenm.202301332.

[151] X.-F. Liu, B. Sun, X.-Y. Li, Y. Huo, C. Zhang, H.-L. Zhang, *J. Mater. Chem. A Mater.* **2024**, *12*, 16627.

[152] R. Luo, T. Lin, M. Chen, X. Yang, Y. Song, M. Wei, S. Cao, J. Zheng, J. Zhao, *Mater. Res. Bull.* **2026**, *196*, 113938.

[153] S. Wang, Q. Zhao, A. Hazarika, S. Li, Y. Wu, Y. Zhai, X. Chen, J. M. Luther, G. Li, *Nat. Commun.* **2023**, *14*, 2216.

[154] E. Arrospide, M. A. Illarramendi, I. Ayesta, N. Guarrotxena, O. García, J. Zubia, G. Durana, *Polymers (Basel).* **2021**, *13*, 424.

[155] M. Riahinezhad, M. Hallman, J.-F. Masson, *Buildings* **2021**, *11*, 299.

[156] M. Xia, J. Luo, C. Chen, H. Liu, J. Tang, *Adv. Opt. Mater.* **2019**, *7*, DOI: 10.1002/adom.201900851.

[157] T. N. L. Tran, A. Chiasera, A. Lukowiak, M. Ferrari, *Materials* **2022**, *15*, 1847.

[158] E. Erol, O. Kıbrıslı, M. Çelikbilek Ersundu, A. E. Ersundu, *Chemical Engineering Journal* **2020**, *401*, 126053.

[159] Y. Niu, S. Sun, C. Yan, C. Wang, J. Qiu, *J. Mater. Chem. C Mater.* **2024**, *12*, 4399.

[160] Y. Hu, W. Zhang, Y. Ye, Z. Zhao, C. Liu, *ACS Appl. Nano Mater.* **2020**, *3*, 850.

[161] Y. Zhang, W. Zhang, Y. Ye, K. Li, X. Gong, C. Liu, *Solar Energy Materials and Solar Cells* **2022**, *238*, 111619.

[162] Z. Wang, S. Wei, F. Huang, G. Bai, X. Zhang, S. Xu, *Solar Energy* **2024**, *269*, 112334.

[163] U. Ekim, E. İlter, E. Özan, Y. Temürhan, M. Çelikbilek Ersundu, A. E. Ersundu, *Physical Chemistry Chemical Physics* **2023**, *25*, 23150.

[164] E. M. Purcell, D. J. Morin, *Electricity and Magnetism:*, Cambridge University Press, **2013**.

[165] B. Valeur, M. N. Berberan-Santos, *J. Chem. Educ.* **2011**, *88*, 731.

[166] Joseph R. Lakowicz, *Principles of Fluorescence Spectroscopy*, Springer US, Boston, MA, **2006**.

[167] B. Henderson, G. F. Imbusch, *Optical Spectroscopy of Inorganic Solids*, Oxford University PressOxford, **2006**.

[168] P. S. Peijzel, A. Meijerink, R. T. Wegh, M. F. Reid, G. W. Burdick, *J. Solid State Chem.* **2005**, *178*, 448.

[169] L. J. Charbonnière, A. M. Nonat, R. C. Knighton, L. Godec, *Chem. Sci.* **2024**, *15*, 3048.

[170] Mark. Fox, *Optical Properties of Solids*, Oxford University Press, **2007**.

[171] V. I. Klimov, T. A. Baker, J. Lim, K. A. Velizhanin, H. McDaniel, *ACS Photonics* **2016**, *3*, 1138.

[172] C. Yang, H. A. Atwater, M. A. Baldo, D. Baran, C. J. Barile, M. C. Barr, M. Bates, M. G. Bawendi, M. R. Bergren, B. Borhan, C. J. Brabec, S. Brovelli, V. Bulović, P. Ceroni, M. G. Debije, J.-M. Delgado-Sanchez, W.-J. Dong, P. M. Duxbury, R. C. Evans, S. R. Forrest, D. R. Gamelin, N. C. Giebink, X. Gong, G. Griffini, F. Guo, C. K. Herrera, A. W. Y. Ho-Baillie, R. J. Holmes, S.-K. Hong, T. Kirchartz, B. G. Levine, H. Li, Y. Li, D. Liu, M. A. Loi, C. K. Luscombe, N. S. Makarov, F. Mateen, R. Mazzaro, H. McDaniel, M. D. McGehee, F. Meinardi, A. Menéndez-Velázquez, J. Min, D. B. Mitzi, M. Moemeni, J. H. Moon, A. Nattestad, M. K. Nazeeruddin, A. F. Nogueira, U. W. Paetzold, D. L. Patrick, A. Pucci, B. P. Rand, E. Reichmanis, B. S. Richards, J. Roncali, F. Rosei, T. W. Schmidt, F. So, C.-C. Tu, A. Vahdani, W. G. J. H. M. van Sark, R. Verduzco, A. Vomiero, W. W. H. Wong, K. Wu, H.-L. Yip, X. Zhang, H. Zhao, R. R. Lunt, *Joule* **2022**, *6*, 8.

[173] C. K. Herrera, A. Vahdani, C. Yang, M. Bates, S. Y. Lunt, B. Borhan, R. R. Lunt, *ACS Photonics* **2023**, *10*, 3195.

[174] S. S. Bhosale, E. Jokar, Y.-T. Chiang, C.-H. Kuan, K. Khodakarami, Z. Hosseini, F.-C. Chen, E. W.-G. Diau, *ACS Appl. Energy Mater.* **2021**, *4*, 10565.

[175] B. S. Richards, I. A. Howard, *Energy Environ. Sci.* **2023**, *16*, 3214.

[176] M. A. . Green, *Solar Cells : Operating Principles, Technology and System Applications*, University Of New South Wales, **1998**.

[177] D. Souri, Z. E. Tahan, *Applied Physics B* **2015**, *119*, 273.

[178] J. Zhao, L. Huang, T. Liang, S. Zhao, S. Xu, *J. Lumin.* **2019**, *205*, 342.

[179] J. Zhang, G. Cai, W. Wang, L. Ma, X. Wang, Z. Jin, *Inorg. Chem.* **2020**, *59*, 2241.

[180] C. Yang, D. Liu, R. R. Lunt, *Joule* **2019**, *3*, 2871.

[181] Vânia. T. Freitas, L. Fu, A. M. Cojocariu, X. Cattoën, J. R. Bartlett, R. Le Parc, J.-L. Bantignies, M. Wong Chi Man, P. S. André, R. A. S. Ferreira, L. D. Carlos, *ACS Appl. Mater. Interfaces* **2015**, *7*, 8770.

[182] A. R. Frias, M. A. Cardoso, A. R. N. Bastos, S. F. H. Correia, P. S. André, L. D. Carlos, V. de Zea Bermudez, R. A. S. Ferreira, *Energies (Basel).* **2019**, *12*, 451.

[183] M. Kong, A. Osvet, K. Forberich, A. Barabash, C. Erban, M. Batentschuk, C. J. Brabec, *ACS Appl. Mater. Interfaces* **2025**, *17*, 1644.

[184] H. Zhao, R. Sun, Z. Wang, K. Fu, X. Hu, Y. Zhang, *Adv. Funct. Mater.* **2019**, *29*, DOI: 10.1002/adfm.201902262.

[185] M. Wei, F. P. G. de Arquer, G. Walters, Z. Yang, L. N. Quan, Y. Kim, R. Sabatini, R. Quintero-Bermudez, L. Gao, J. Z. Fan, F. Fan, A. Gold-Parker, M. F. Toney, E. H. Sargent, *Nat. Energy* **2019**, *4*, 197.

[186] Y. Liu, N. Li, R. Sun, W. Zheng, T. Liu, H. Li, Y. Chen, G. Liu, H. Zhao, H. Liu, Y. Zhang, *Nano Energy* **2021**, *85*, 105960.

[187] K. Nikolaidou, S. Sarang, C. Hoffman, B. Mendewala, H. Ishihara, J. Q. Lu, B. Ilan, V. Tung, S. Ghosh, *Adv. Opt. Mater.* **2016**, *4*, 2126.

[188] T. Wei, K. Lian, J. Tao, H. Zhang, D. Xu, J. Han, C. Fan, Z. Zhang, W. Bi, C. Sun, *ACS Appl. Mater. Interfaces* **2022**, *14*, 44572.

[189] M. Sun, Y. Chen, S. Tian, M. Zhang, H. Jiang, K. Liu, J. Xu, F. Dai, L. Wang, Z. Zhou, J. Xing, *Adv. Funct. Mater.* **2025**, *35*, DOI: 10.1002/adfm.202413553.

PUBLICATIONS FROM THE THESIS

Papers

1. *Scalable Perovskite Quantum Dot Glass Nanocomposites for High-Efficiency Luminescent Solar Concentrators,* E. İlter, U. Ekim, E. Asadi, K. Tsoi, S. Yerci, M. Çelikbilek Ersundu, A. E. Ersundu, *Adv. Funct. Mater.* **2025**, *35*, DOI: 10.1002/adfm.202506829

2. *Highly Transparent and Color-Neutral Eu^{3+}-Doped Glass Luminescent Solar Concentrators for Scalable BIPV Integration*, E. İlter, U. Ekim, H. S. Çelik, M. Çelikbilek Ersundu, A. E. Ersundu, J. Mater. Chem. C Mater. 2026, DOI: 10.1039/D5TC04310G

Conference

1. *PVCon2024 International Conference on Photovoltaic Science and Technologies*, Middle East Technical University, Oral Presentation, 2024, Ankara/Türkiye.

Projects

1. *Akıllı Binalara Entegre Fotovoltaik Sistemler için Cam Nanokompozit Esaslı Lüminesans Güneş Yoğunlaştırıcılarının Geliştirilmesi*, Yıldız Technical University Scientific Research Projects Coordination Unit, 2025-continue.